Investigation of the Charge Symmetry Breaking Reaction $dd \rightarrow {}^{4}\mathrm{He}\pi^{0}$ with the WASA-at-COSY Facility

INAUGURAL - DISSERTATION

zur

Erlangung des Doktorgrades

der Mathematisch-Naturwissenschaftlichen Fakultät

der Universität zu Köln

vorgelegt von

Maria Katarzyna ŻUREK

aus Chrzanów, Polen

Köln 2017

Abstract

Probing elementary symmetries and symmetry breaking tests our understanding of the theory of strong forces, Quantum Chromodynamics. The presented study concentrates on the charge symmetry forbidden reaction $dd \rightarrow {}^4\mathrm{He}\pi^0$. The aim is to provide experimental results for comparison with predictions from Chiral Perturbation Theory (χ_{PT}) to study effects induced by quark masses on the hadronic level, e.g., the proton-neutron mass difference.

First calculations showed that in addition to the existing high-precision data from TRIUMF and IUCF, more data are required for a precise determination of the parameters of χ_{PT}. These new data should comprise the measurement of the charge symmetry forbidden $dd \rightarrow {}^4\mathrm{He}\pi^0$ reaction at sufficiently high energy, where the p-wave contribution becomes important. A first measurement with the WASA-at-COSY experiment at an excess energy of $\varepsilon = 60\,\mathrm{MeV}$ was performed, but the results did not allow for a decisive interpretation because of limited statistics.

This thesis reports on a second measurement of the $dd \rightarrow {}^4\mathrm{He}\pi^0$ reaction at $\varepsilon = 60\,\mathrm{MeV}$ using an improved WASA detector setup aiming at higher statistics. A sample of 336 ± 43 event candidates have been extracted using a data set from an eight-week long beamtime, and total and differential cross sections have been determined. The angular distribution has been described with a function of the form $\mathrm{d}\sigma/\mathrm{d}\Omega = a + b\cos^2\theta^*$, where θ^* is the scattering angle of the pion in the c.m. coordinate system. The obtained parameters a and b and the total cross section are:

$$a = \left(1.75 \pm 0.46(\mathrm{stat.})^{+0.31}_{-0.8}(\mathrm{syst.})\right)\mathrm{pb/sr}\,,$$

$$b = \left(13.6 \pm 2.2(\mathrm{stat.})^{+0.9}_{-2.7}(\mathrm{syst.})\right)\mathrm{pb/sr}\,,$$

$$\sigma_{\mathrm{tot}} = \left(79.1 \pm 7.3(\mathrm{stat.})^{+1.2}_{-10.5}(\mathrm{syst.}) \pm 8.1(\mathrm{norm.}) \pm 2.0(\mathrm{lumi.\ syst.})\right)\mathrm{pb}\,.$$

For this experiment a modified detector setup optimized for a time-of-flight measurement of the forward going particles has been used. After detector calibration and track reconstruction, signal events have been selected using a chain of cuts and a kinematic fit. For absolute normalization the integrated luminosity has been obtained using the $dd \rightarrow {}^3\mathrm{He}n\pi^0$ reaction. The final acceptance correction has been performed using a Monte Carlo signal generator with the measured angular distribution.

The obtained differential cross section indicates the presence of higher partial waves in the final state. A combined interpretation of these results with the other measurements of the $dd \rightarrow {}^4\mathrm{He}\pi^0$ reaction allowed to determine the square of the magnitude of the p-wave amplitude $|C|^2 = \left(520 \pm 290(\mathrm{stat.})^{+50}_{-430}(\mathrm{syst.})\right)\mathrm{pb/}\left(\mathrm{sr}\cdot(\mathrm{GeV}/c)^2\right)$ and the real part of the $s-d$ interference term $\Re\{A_0^* A_2\} = \left(1670 \pm 320(\mathrm{stat.})^{+80}_{-430}(\mathrm{syst.})\right)\mathrm{pb/}\left(\mathrm{sr}\cdot(\mathrm{GeV}/c)^2\right)$ neglecting any further initial and final state interactions. The result shows that any theoretical attempt to describe the reaction has to include, in addition to p-waves, also d-wave contributions.

Zusammenfassung

Die Untersuchung elementarer Symmetrien und ihrer Brechung testet unser Verständnis der Theorie der starken Wechselwirkung, der Quantenchromodynamik. Die vorliegende Doktorarbeit konzentriert sich auf die Reaktion $dd \to {}^4\text{He}\pi^0$, welche die Ladungssymmetrie verletzt. Das Ziel ist es, die experimentellen Ergebnisse mit den Vorhersagen der chiraler Störungstheorie (χ_{PT}) zu vergleichen, um die Effekte von Quarkmassen auf hadronischer Ebene zu untersuchen. Ein Beispiel ist der Einfluß auf die Massendifferenz von Proton und Neutron.

Erste theoretische Rechnungen zeigten, dass zusätzlich zu den bestehenden Hochpräzisionsdaten von TRIUMF und IUCF weitere Daten für eine genaue Bestimmung der χ_{PT} Parameter erforderlich sind. Diese neuen Daten zur Ladungssymmetrie verletzenden $dd \to {}^4\text{He}\pi^0$ Reaktion müssen bei ausreichend hoher Energie gemessen werden, da dort die Beiträge von p-Wellen wichtig werden. Eine erste Messung wurde mit dem WASA-at-COSY Experiment bei einer Überschussenergie von $\varepsilon = 60\,\text{MeV}$ durchgeführt, allerdings ließen die Ergebnisse wegen der begrenzten Statistik keine endgültige Interpretation zu.

Diese Dissertation besckäftigt sich mit einer zweiten Messung der Reaktion $dd \to {}^4\text{He}\pi^0$ bei $\varepsilon = 60\,\text{MeV}$ mit einem verbesserten Aufbau des WASA-Detektors und dem Ziel einer höheren Statistik. Aus den Daten einer acht Wochen langen Messung wurden 336 ± 43 Eventkandidaten extrahiert. Dabei wurden der totale und differentielle Wirkungsquerschnitt bestimmt und die Winkelverteilung mit der Funktion $\mathrm{d}\sigma/\mathrm{d}\Omega = a + b\cos^2\theta^*$ gefittet. Die dadurch erhaltenen Parameter a und b und der totale Wirkungsquerschnitt ergeben sich zu:

$$a = \left(1.75 \pm 0.46(\text{stat.})^{+0.31}_{-0.8}(\text{syst.})\right)\,\text{pb}/\text{sr}\,,$$

$$b = \left(13.6 \pm 2.2(\text{stat.})^{+0.9}_{-2.7}(\text{syst.})\right)\,\text{pb}/\text{sr}\,,$$

$$\sigma_{\text{tot}} = \left(79.1 \pm 7.3(\text{stat.})^{+1.2}_{-10.5}(\text{syst.}) \pm 8.1(\text{norm.}) \pm 2.0(\text{lumi. syst.})\right)\,\text{pb}\,.$$

Der modifizierte Detektoraufbau, welcher für die Messung verwendet wurde, ist auf die Nutzung der Flugzeit für nach vorne emittierte Teilchen ausgelegt. Die Signalereignisse wurden nach erfolgter Detektorkalibrierung und Spurrekonstruktion mittels eines kinematischen Fits und verschiedenen Analyseschnitten ausgewählt. Für die absolute Normalisierung wurde die integrierte Luminosität mit der $dd \to {}^3\text{He}n\pi^0$ Reaktion bestimmt. Die endgültige Akzeptanzkorrektur wurde auf der Basis einer Monte-Carlo Simulation durchgeführt, welche die gemessene Winkelverteilung berücksichtigt.

Der erhaltene differentielle Wirkungsquerschnitt zeigt das Vorhandensein von höheren Partialwellen im Endzustand. Eine gemeinsame Analyse dieser Ergebnisse mit den anderen Messungen der $dd \to {}^4\text{He}\pi^0$ Reaktion erlaubt die Bestimmung des Quadrats der p-Wellenamplitude $|C|^2 = \left(520 \pm 290(\text{stat.})^{+50}_{-430}(\text{syst.})\right)\,\text{pb}/\left(\text{sr} \cdot (\text{GeV}/c)^2\right)$

und des Realteils des $s-d$ Interferenzterms $\Re\{A_0^* A_2\} = \left(1670 \pm 320(\text{stat.})^{+80}_{-430}(\text{syst.})\right)$ pb/ $\left(\text{sr} \cdot (\text{GeV}/c)^2\right)$, ohne die Berücksichtigung von weiteren Anfangs- und Endzustandswechselwirkungen. Das Ergebnis zeigt, dass jede theoretische Beschreibung der Reaktion zusätzlich zu p-Wellen auch d-Wellen-Beiträge berücksichtigen muss.

Acknowledgements

Undertaking this PhD project has been a truly life-changing experience for me and it would not have been possible to do without the support and guidance that I received from many people.

I would like to express my sincere gratitude to my thesis advisor Prof. Dr. Hans Ströher for making it possible for me to write this thesis at the Forschungszentrum Jülich. Thank you for the support of my research, for your patience, motivation, and immense knowledge in the field of hadron physics. Your guidance helped me constantly during research and writing of this thesis. Thank you also for giving me lots of precious advice about how to present my work and the opportunity to participate in workshops and conferences.

I am sincerely grateful to my scientific advisor Dr. Volker Hejny for his excellent guidance. Thank you for all the time you spent with me on countless discussions about the analysis, for helping me to understand deeply the experimental and theoretical side of this project, for motivating me to find creative solutions to non-obvious problems, and showing how important carefulness and precision are in experimental work. I am grateful for proofreading this thesis and for all comments on my work, especially these critical ones, because they helped me to improve. I could not imagine having a better mentor. Your experience is really astonishing, I wish every physics collaboration had its own "Volker"!

I would like to thank Prof. Dr. Jan Jolie for reviewing my thesis, as well as Prof. Dr. Alexander Altland and Prof. Dr. Detlev Gotta for being members of my examination committee.

I am grateful to Prof. Dr. Christoph Hanhart and Dr. Florian Hauenstein for proofreading this dissertation.

I also want to thank the "charge symmetry breaking team" from Jagiellonian University - Prof. Dr. Andrzej Magiera and Dr. Aleksadra Wrońska for their help during the experiment, all the discussions and lots of useful advice. Also warm thanks to Dr. Edward Stephenson for wise comments and deep interest in the project.

I would like to express my gratitude to Prof. Dr. Michael Albrow for sharing his passion and enthusiasm for scientific work during our "free-time" project in diffraction physics. I am grateful for your supervision during the internships in Fermilab, when my adventure with particle physics started 6 years ago, and for continuing it when I am at the beginning of my scientific career. I am really lucky I have the opportunity to work with you.

I am grateful to the whole WASA-at-COSY collaboration, especially all people who were helping me during the beamtime. In total we had 183 eight-hour long shifts to

To my family and true friends

Contents

List of Figures

List of Tables

List of Abbreviations

QCD	**Q**uantum **C**hromo**d**ynamics
QED	**Q**uantum **E**lectro**d**ynamics
SM	**S**tandard **M**odel
χ_{PT}	**Chi**ral **P**erturbation **T**heory
EFT	**E**ffective **F**ield **T**heory
CSB	**C**harge **S**ymmetry **B**reaking
TRIUMF	**Tri**-**U**niversity **M**eson **F**acility
WASA	**W**ide **A**ngle **S**hower **A**pparatus
COSY	**CO**oler **SY**nchrotron
ToF	**T**ime-**o**f-**F**light
FD	**F**orward **D**etector
CD	**C**entral **D**etector
FWC	**F**orward **W**indow **C**ounter
FPC	**F**orward **P**roportional **C**hamber
FVH	**F**orward **V**eto **H**odoscope
MDC	**M**ini **D**rift **C**hamber
PSB	**P**lastic **S**cintillator **B**arrel
SCS	**S**uper**c**onductive **S**olenoid
SEC	**S**cintillator **E**lectromagnetic **C**alorimeter
DAQ	**D**ata **Ac**quisition
FPGA	**F**ield-**P**rogrammable **G**ate **A**rray
QDC	**C**harge-to-**D**igital **C**onverter
TDC	**T**ime-to-**D**igital **C**onverter
FIFO	**F**irst **I**n **F**irst **O**ut

Chapter 1

Introduction

Why does the Universe exist as it is?

For decades a multitude of physicists have been trying to understand and describe the structure of matter and basic interactions in Nature. Many mysteries of the existence of our Universe have been solved by curiosity-driven studies, but a lot of fundamental questions are still open.

Nowadays, we know that protons and neutrons, collectively called nucleons, form nuclei. Together with electrons, they build all the stable elements in the visible Universe. Nucleons are not elementary particles, but they are built of quarks and gluons. The basic constituents of protons and neutrons are the up (u) and down (d) quarks. In the constituent quark model, the proton is made of two u and one d quark, while the neutron comprises of one d and two u quarks. In units of the elementary charge e, the charges of the u and d quarks are $+2/3$ and $-1/3$, respectively. Therefore, the proton has a positive charge $1e$, and the neutron is neutral. However, in addition to the difference in charge, there is also a small difference in the u and d quark masses. This tiny difference is vital for our very existence. In a world with equal masses of u and d quarks, the proton-neutron mass difference would be based exclusively on electromagnetic effects. This would result in the proton being heavier than the neutron. In such a world the proton, not the neutron, would have a finite lifetime, and stable hydrogen atoms would not exist. Our whole universe would not exist in the way it is now.

The importance of light quark mass effects has driven many theoretical and experimental studies. The goal is to describe the effects induced by quark masses in hadronic reactions. It is to show that our understanding of the theory of strong interaction — Quantum Chromodynamics (QCD), and especially the calculations based on it — is correct. The measurement of the $dd \rightarrow {}^4\text{He}\pi^0$ reaction provides an important experimental input to the calculations which trace the proton-neutron mass difference induced by the difference of u and d quark masses.

In this Chapter an introduction to the topic is given. Basic information about the structure of matter, the origin of mass and the idea of isospin is discussed. A short description and the formalism of low energy hadron physics is described. In Chapter 2 the theoretical and experimental status of the selected charge symmetry breaking observables is presented. The experimental setup used in this measurement and the run

conditions are described in Chapter 3. The basic data analysis procedure, including the calibration of the detector and the tracking procedure as well as the Monte Carlo simulations, is reported in Chapter 4. The selection of the $dd \rightarrow {}^4\text{He}\pi^0$ reaction is described in Chapter 5. The luminosity determination is reported in Chapter 6. The results are presented in Chapter 7. A discussion of these results and an outlook in Chapter 8 complete the thesis.

1.1 Standard Model

1.1.1 Elementary Particles and Interactions

All the matter in the Universe is built of basic building blocks called elementary particles, interacting with each other by four fundamental forces, namely the gravitational, electromagnetic, weak and strong force. Elementary particles and the interactions between them (with the exception of the gravitational force) are described within a quantum field theory called the Standard Model (SM). The schematic depiction of elementary particles included in the SM is presented in Fig. 1.1.
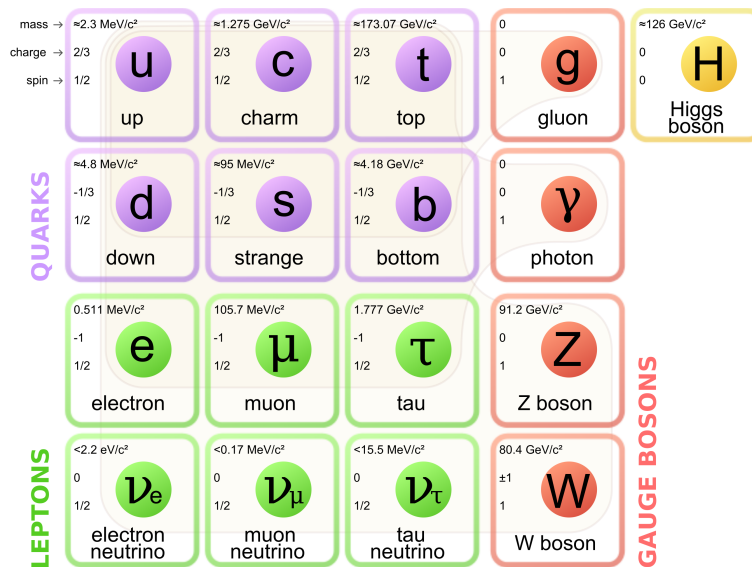
FIGURE 1.1: Elementary particles included in the Standard Model. The three generations of quarks and leptons are presented in the first three columns, gauge bosons are in the fourth column, and the Higgs boson in the fifth one. Source: [1].

The elementary particles building all matter are fermions, which means they have a spin equal to $\frac{1}{2}\hbar$. They are divided in two groups — leptons and quarks. Within each group there are three generations of pairs of particles. The first generation consists of the most stable and lightest particles, while the less stable and heavier ones belong to the higher generations.

Leptons are particles which do not interact via the strong force. For leptons, every generation consists of one negatively charged particle, and one neutral partner, called

neutrino. Therefore, we have: electron and electron neutrino (e, ν_e), muon and muon neutrino (μ, ν_μ), tauon and tauon neutrino (τ, ν_τ). Quarks interact strongly in addition to the other interactions. They are carriers of one of three colour charges. Quarks possess also an electric charge of $+2/3$ or $-1/3$ of the elementary charge e. The three families of quarks ordered by mass are: up and down quark (u, d), strange and charm quark (s, c), and bottom and top quark (b, t). In addition, every matter particle has an antiparticle with identical mass.

The Standard Model describes the interactions as the result of the exchange of force-carrier particles. These particles are the so-called gauge bosons and have a spin of $\hbar$. The weakest interaction described in the SM is the weak force. It is described as an exchange of W^+, W^-, and Z^0 bosons. They couple to quarks and leptons. Because of the large gauge bosons masses ($M_W = 80.4 \, \text{GeV}/c^2$, $M_Z = 91.2 \, \text{GeV}/c^2$), the weak interaction has only a short range of about 10^{-18} m [2].

The exchange particles for the electromagnetic force are photons, which couple to all particles with an electromagnetic charge. Photons are massless, therefore this interaction has an infinite range. The theory of electromagnetic interactions — quantum electrodynamics (QED) — is unified with the theory of weak forces in the so-called Glashow-Weinberg-Salam model [3] (electroweak interactions).

The strongest of all four fundamental interactions is the strong force. It is carried by eight massless gluons which couple to quarks and to themselves. The range of the strong force is about the radius of a nucleon. In the theory of strong forces, Quantum Chromodynamics (QCD), there are three types of strong charges, called colour charges. A quark can carry one of three primary colours (red, blue and green), and its antiquark carries the corresponding anticolour. Gluons carry one colour and one anti-colour. All composite particles made of quarks, called hadrons, have zero net colour, i.e., they are colour singlets. Particles built of quark and anti-quark are called mesons, while particles consisting of three quarks are called baryons [4].

1.1.2 Color Confinement

The Standard Model is a quantum field theory based on the gauge invariance of the group $SU(3)_C \times SU(2) \times U(1)$. Quantum Chromodynamics is the $SU(3)_C$ component of the Standard Model symmetry group. The remaining $SU(2) \times U(1)$ is the symmetry group of the electroweak theory. For an introduction to quantum field theory see, e.g., [5, 6].

Most calculations in Quantum Field Theory are performed in an approximated way using perturbative methods based on an expansion in powers of the coupling constant. This method is applicable only in the limit of a small coupling constant $\alpha \ll 1$. The coupling constant determines the strength of the force exerted in an interaction. The effective coupling constant varies with the energy scale. For QED it grows with energy. At large distances, i.e, low four-momentum transfer Q^2, it is about $\alpha \approx 1/137$, at the scale of the Z boson it is about $\alpha \approx 1/128$ [2]. At very high energies, where the Standard Model is no longer applicable, the coupling becomes large

and eventually diverges. In QCD the self-coupling of gluons affects significantly this so-called running of the coupling constant α_s. The strong coupling becomes weak for processes involving large four-momentum transfers. This phenomenon is called asymptotic freedom. At the scale of the Z boson α_s is about 0.12 [2]. At small four-momentum transfers α_s diverges.

One can introduce a QCD energy scale Λ_{QCD} — the energy scale at which the perturbatively-defined coupling constant α_s would diverge. The effective strong coupling constant can be presented then as:

$$\alpha_s(Q^2) = \frac{2\pi}{\beta_0 \log(Q^2/\Lambda_{QCD}^2)}, \tag{1.1}$$

where $\beta_0 = 11 - 2/3 n_f$, and n_f is the number of quark flavours. The value of Λ_{QCD} can be determined experimentally by measuring the dependence of α_s on the four-momentum transfer Q^2. The obtained value is about $\Lambda_{QCD} \approx 250 \, \text{MeV}$ [7].

For the perturbative region, $Q^2 \gg \Lambda_{QCD}^2$, the quark and gluon degrees of freedom dominate. At low four-momentum transfer, below Λ_{QCD}^2, quarks and gluons are strongly confined. They cannot be observed as a free particles, but they form colour neutral objects, called hadrons. The theoretical description of strong interaction in this region, referred to as "strong QCD", relies on lattice gauge theory, phenomenological models or effective field theories.

The strong coupling constant α_s is one of the parameters of QCD. Like α, it has to be extracted from measured observables by theoretical calculations [3]. The general properties of the QCD and QED coupling constant are presented in Fig. 1.2.
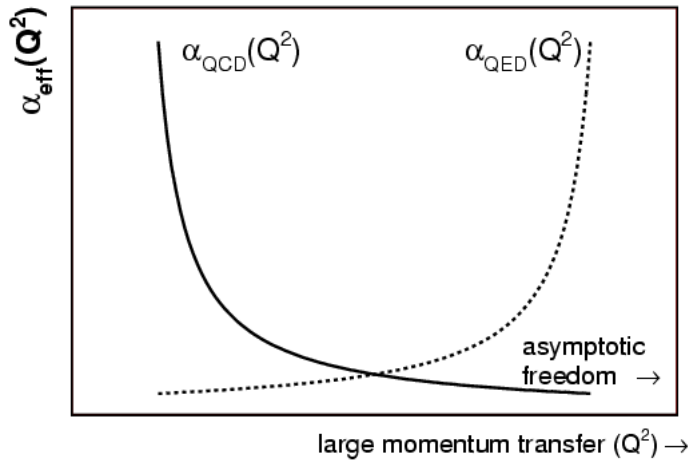
FIGURE 1.2: Schematic behaviour of the coupling constants of QCD and QED. In QED, for low four-momentum transfers Q^2 the coupling constant is small. It increases as a function of Q^2 and at very high energy it diverges. For QCD the coupling at small Q^2 diverges and for high Q^2 it asymptotically goes to zero. Note that this picture shows only the general behaviour for the coupling constant of QCD and QED and the scale on the x-axis is different for these two curves. Source: [8].

1.2 Origin of Mass

The Standard Model includes one additional particle - the recently discovered Higgs boson [9, 10]. The discovery confirmed the theory of the Brout-Englert-Higgs mechanism [11–15]. This mechanism explains the generation of the intrinsic mass of the gauge W and Z bosons. Elementary particles can couple to the quantum excitation of the Higgs field (Higgs boson) and this endows them with an effective mass. The particles coupled to this field are quarks, leptons, W and Z bosons, and the Higgs boson by itself.

The ordinary matter in the Universe is built of protons, neutrons and electrons, and protons and neutrons are made of quarks and gluons. However, only a few percent of the nucleon mass is coming from the intrinsic masses of the quarks themselves [16]. For example, for the proton ($M_p = 938 \, \text{MeV}/c^2$) the intrinsic masses of u and d quarks would contribute only about $10 \, \text{MeV}/c^2$ to its mass. All the rest has its origin in the dynamics of the strong processes inside the nucleon [17, 18].

In the limit of massless quarks, the global chiral symmetry ($SU(n)_R \times SU(n)_L = SU(n)_V \times SU(n)_A$, where n is the number of quark flavours) of the QCD Langrangian is not broken explicitly. It is broken spontaneously through the formation of a quark condensate in the ground state to the isospin symmetry group $SU(n)_V$. This quark condensate is a fermionic condensate formed by quark-antiquark pairs [19]. Quarks interact with this environment as though they had mass. One can imagine it as massless quarks traveling at the speed of light which are slowed down by the interaction with the quark condensate. Thus, they can be described as massive quarks in a free environment [17]. The nonperturbative scale of the dynamical chiral symmetry breaking Λ_χ is about 1 GeV [2, 20]. Because of the small non-zero quark masses, the chiral symmetry is also broken explicitly. For quarks with masses $M > \Lambda_\chi$ the explicit chiral symmetry breaking dominates (c, b and t, the so-called "heavy" quarks). For $M < \Lambda_\chi$ the spontaneous chiral symmetry breaking is dominating (u, d and s).

As a result of the spontaneous chiral symmetry breaking for vanishing quark masses, according to the Goldstone theorem [21], massless Nambu-Goldstone bosons should be observed. Their number is determined by the structure of the symmetry group. For the $SU(2)_R \times SU(2)_L \rightarrow SU(2)_V$ symmetry (u, d quarks considered) there are three Nambu-Goldstone bosons, one for each of the three generators of the spontaneously broken symmetry, corresponding to the three pions (π^+, π^0, π^-). The spontaneously broken $SU(3)_R \times SU(3)_L$ symmetry (u, d and s quarks considered) has eight generators, therefore there are eight Nambu-Goldstone bosons (π^+, π^0, π^-, η_8, K^0, $\bar{K}^0$, K^+, K^-). Because of the explicit chiral symmetry breaking caused by non-zero quark masses, the Nambu-Goldstone bosons have also small finite masses [22].

The main origin of the ordinary mass is thus not the Higgs mechanism, but rather is a consequence of the spontaneous breaking of chiral symmetry. For a popular introduction to the topic see [16, 23]. Detailed information about the origin of mass can be found in [17].

1.3   Chiral Perturbation Theory

An analytic derivation of hadronic interactions from the fundamental QCD Lagrangian is still not achieved. However, what is known are the symmetry features of the strong interaction. The chiral symmetry properties of QCD are the key components of Chiral Perturbation Theory (χ_{PT}) [24, 25], which is an effective field theory (EFT) for low energy QCD.

The concept of an EFT can be presented as a theorem [25, 26] which states that, if the calculations are based on the most general interaction consistent with the symmetries and symmetry-breaking patterns of the underlying fundamental theory (in our case QCD), the results will be consistent with those of the underlying theory up to a given order in perturbation theory. In χ_{PT} the dynamic degrees of freedom [27] are not the fundamental quarks and gluons but the lightest pseudoscalar mesons identified as the Nambu-Goldstone bosons of the spontaneously broken chiral symmetry, which are non-interacting in the chiral limit for vanishing momenta.

As χ_{PT} is built for low energy QCD, it takes explicitly into account the relevant degrees of freedom, which are the states with $M \ll \Lambda_\chi$, where Λ_χ is a hadronic scale already mentioned in Sec. 1.2. Heavier excitations are integrated out from the action. Only because the pseudoscalar octet is separated on the mass scale from the rest of the hadronic spectrum, it is possible to construct this EFT.

The fields of the Nambu-Goldstone bosons are represented in the chiral Lagrangian by the unitary matrix $U = \exp(i\sqrt{2}\Phi/f)$, where the most common form of Φ is:

$$\Phi = \begin{bmatrix} \frac{1}{\sqrt{2}}\pi^0 + \frac{1}{\sqrt{6}}\eta_8 & \pi^+ & K^+ \\ \pi^- & -\frac{1}{\sqrt{2}}\pi^0 + \frac{1}{\sqrt{6}}\eta_8 & K^0 \\ K^- & \bar{K}^0 & -\frac{2}{\sqrt{2}}\eta_8 \end{bmatrix}, \tag{1.2}$$

and f is the Nambu-Goldstone boson decay constant in the chiral limit.

At low energies, the interaction between Nambu-Goldstone bosons can be expanded in powers of their momenta p, which are small compared to Λ_χ. Powers of momenta correspond to powers of derivatives of the Nambu-Goldstone boson fields in the χ_{PT} Lagrangian. The explicit chiral symmetry breaking is introduced in the χ_{PT} Lagrangian via the quark mass matrix $\mathcal{M}$. Therefore, in addition to the derivative expansion, the effective Lagrangian is expanded simultaneously in powers of $\mathcal{M}$, which is possible since the quark masses are much smaller then Λ_χ. Below, the lowest order effective chiral Lagrangian $\mathcal{L}_{\chi_{PT}}$ is presented. It shares the same symmetry patterns with QCD: C, P, T, Lorentz invariance and, in particular, chiral symmetry. The first term in $\mathcal{L}_{\chi_{PT}}$ represents the effective χ_{PT} Lagrangian for the limit of massless quarks. The second term introduces the explicit chiral symmetry breaking [28].

$$\mathcal{L}_{\chi_{PT}} = \frac{f^2}{4}\langle \partial_\mu U^\dagger \partial^\mu U \rangle + \frac{f^2 B}{2}\langle U^\dagger \mathcal{M} + \mathcal{M}^\dagger U \rangle, \tag{1.3}$$

where $\mathcal{M}$ is the quark mass matrix for $p = 0$. The constants B and f are not fixed

by symmetry requirements alone. The physical meaning of the chiral coupling f at the considered order is, that — in the chiral limit — it is the pion decay constant ($f_\pi \approx 92.4$ MeV). Also in the chiral limit, B is directly related to the chiral condensate: $\langle 0|\bar{q}q|0\rangle = -Bf_\pi^2 + \mathcal{O}(M_q)$. Thus, B is the order parameter of spontaneous chiral symmetry breaking. The value of $B \approx 1800$ MeV has been extracted from the sum-rule value $\langle 0|\bar{q}q|0\rangle = -(250\,\text{MeV})^3$ [29].

An effective field theory can be also introduced for mesonic resonances and baryons [30, 31]. However, the fact that in the chiral limit baryon masses do not vanish and that they are not small compared to $\Lambda\chi$ complicates the chiral analysis of baryons [27]. χ_{PT} has been successfully extended to pion production where typical momenta are in the order of $\sqrt{m_\pi M}$, where M is the nucleon mass (for a review see [32]). A complete description of the interactions in the baryonic sector based on χ_{PT} requires to fix the strength of the hadronic operators either from experiment or from lattice QCD calculations. For the πN interaction, at leading order the only parameters are the pion mass and pion decay constant [33, 34], but for higher orders the number of unknown parameters increases. The theory, however, can provide non-trivial links between the different operators, which need to be fixed by experiment. Therefore, an investigation of the basic symmetries of the strong interaction requires an joint effort of experiment and theory.

1.4 Isospin

1.4.1 Isospin Multiplets

After the discovery of the neutron in 1932 by Chadwick [35], the similarity between the proton p and the neutron n led to the idea of the existence of an approximate symmetry. It was suggested that both may be treated as two states of the same particle, namely the nucleon N. This requires that neutron and proton have the same mass. In fact, their masses are only approximately equal ($m_n = 939.57$ MeV/c^2, $m_p = 938.28$ MeV/c^2 [2]). It was suggested that nucleons behave identically under the strong interaction and that the only difference between these two states has its origin in their charge content: isospin symmetry would be a good symmetry of the strong interaction. A strong isospin quantum number was introduced, with the projection coordinate T_3 equal to $+1/2$ for protons and $-1/2$ for neutrons.

The symmetry group of the rotation operators in isospin space is a $SU(2)_V$ group with operators represented as:

$$\hat{U}_T(\alpha) = \hat{U}_T(\alpha_1, \alpha_2, \alpha_3) = e^{-i\frac{1}{2}(\hat{\tau}_1\alpha_1 + \hat{\tau}_2\alpha_2 + \hat{\tau}_3\alpha_3)} = e^{-i\frac{1}{2}\alpha_i\hat{\tau}_i}. \tag{1.4}$$

The angles $\alpha = \{\alpha_1, \alpha_2, \alpha_3\}$ describe the rotations around three axes in the abstract isospin space, and τ_i are the Pauli matrices.

The isospin multiplets can be introduced in the same way as the angular momentum and spin multiplets. Each multiplet is $(2T + 1)$ times degenerate. The nucleon

isospin doublet $|T, T_3\rangle$ consists of proton and neutron states with $T = \frac{1}{2}$:

$$
\begin{aligned}
\left| \frac{1}{2}, \frac{1}{2} \right\rangle &\equiv |p\rangle, \\
\left| \frac{1}{2}, -\frac{1}{2} \right\rangle &\equiv |n\rangle.
\end{aligned}
\tag{1.5}
$$

The isospin triplet with $T = 1$ is realized in nature, e.g., for π mesons:

$$
\begin{aligned}
|1, 1\rangle &\equiv |\pi^+\rangle, \\
|1, 0\rangle &\equiv |\pi^0\rangle, \\
|1, -1\rangle &\equiv |\pi^-\rangle.
\end{aligned}
\tag{1.6}
$$

Let us now consider the isospin of the deuteron. Each deuteron consists of one proton and one neutron and its wave function can be described in terms of the constituent nucleons. Therefore, the third component of its isospin T_3 equals to 0. The first possibility is that the deuteron is an isospin singlet state $|0, 0\rangle$:

$$
|0, 0\rangle = \frac{1}{\sqrt{2}} \left(|p\rangle |n\rangle - |n\rangle |p\rangle \right).
\tag{1.7}
$$

Another option is that the deuteron is the isospin state $|1, 0\rangle$ from the triplet:

$$
\begin{aligned}
|1, 1\rangle &= |p\rangle |p\rangle, \\
|1, 0\rangle &= \frac{1}{\sqrt{2}} \left(|p\rangle |n\rangle + |n\rangle |p\rangle \right), \\
|1, -1\rangle &= |n\rangle |n\rangle.
\end{aligned}
\tag{1.8}
$$

Because of isospin symmetry, all triplet states should have comparable energy. Thus, if the deuteron was an isotriplet $|1, 0\rangle$, nn and pp bound states should have been observed in nature. This is not the case. Therefore, the deuteron has to be the isospin singlet state $|0, 0\rangle$. With similar arguments one can show that the nucleus of ^{4}He (which is build of two protons and two neutrons) is also an isosinglet state.

Within the Standard Model, the isospin symmetry of the proton and the neutron can be reinterpreted as the isospin symmetry of the u and d quarks. Then the fundamental isospin doublet of the up and down quark states is:

$$
\begin{aligned}
|u\rangle &\equiv \left| \frac{1}{2}, \frac{1}{2} \right\rangle, \\
|d\rangle &\equiv \left| \frac{1}{2}, -\frac{1}{2} \right\rangle.
\end{aligned}
\tag{1.9}
$$

In the framework of the constituent quark model the proton and the neutron can be represented as totally symmetric uud and udd states. The pion triplet can be presented

as:

$$|\pi^+\rangle \equiv |u\bar{d}\rangle,$$
$$|\pi^o\rangle \equiv \frac{1}{\sqrt{2}}\left(|u\bar{u}\rangle - |d\bar{d}\rangle\right), \tag{1.10}$$
$$|\pi^-\rangle \equiv |d\bar{u}\rangle.$$

1.4.2 Isospin Symmetry Violation

In the Standard Model there are two sources of isospin symmetry violation. The first natural source is the charge difference of the different quarks. The charges of the lightest quarks are $Q_u = 2/3e$ and $Q_d = -1/3e$ (convention: $e > 0$). In addition, isospin symmetry is broken by the strong interaction because the quarks also have slightly different masses [36, 37]. In order to study the effects caused by the quark mass difference, these two sources of isospin symmetry breaking need to be disentangled.

The isospin symmetry breaking on the hadronic level manifests itself in several static observables. One observable, which is important for our very existence, is the proton-neutron mass difference ΔM_{pn}. As the quark mass difference, it has two origins: an electromagnetic and a strong one. If isospin symmetry was broken only because of the different charges of the lightest quarks, ΔM_{pn} would be a purely electromagnetic effect, with the result that the proton would be heavier then the neutron, and that stable hydrogen atoms would not exist. However, nature shows that this is not the case and that the proton as a stable particle (with a mean lifetime $\tau_p > 10^{32}$ yr) is lighter then the neutron ($\tau_n \approx 880$ s). Thus, ΔM_{pn} has an additional contribution from the strong interaction:

$$\Delta M_{pn} = \Delta M_{pn}^{strong} + \Delta M_{pn}^{em}. \tag{1.11}$$

The electromagnetic part ΔM_{pn}^{em} can be calculated based on QED considerations and dispersion theory [38], where ΔM_{pn}^{strong} can be obtained indirectly ($\Delta M_{pn}^{strong} = \Delta M_{pn} - \Delta M_{pn}^{em}$) [37, 39], from lattice QCD [40], or from χ_{PT} calculations. Chiral perturbation theory provides an interesting link between the static isospin breaking observable ΔM_{pn}^{strong} and, at leading order, the dynamic isospin violating πN scattering length [36].

In general, experimentally it is difficult to get access to quark mass effects in low energy hadron physics, where the effect of the pion mass difference $\Delta \pi = M_{\pi^\pm} - M_{\pi^0}$, which is of electromagnetic origin, is by far dominant [41]. Therefore, any observables where $\Delta \pi$ does not contribute are of interest. Here, charge symmetry breaking (CSB) play a major role.

1.4.3 Charge Symmetry Violation

Charge symmetry is a special case of isospin symmetry. It is the invariance under the rotation of an angle of $180°$ in isospin space around the T_2 axis. The charge symmetry

operator is:

$$\hat{U}_{CS} = e^{-\frac{1}{2}i\pi\tau_2}. \tag{1.12}$$

The pion mass difference $\Delta\pi$ is invariant under this rotation and does not contribute to charge symmetry observables. $\hat{U}_{CS}$ transforms the π^+ state into a π^-, and $m_{\pi^+} = m_{\pi^-}$ because of CPT symmetry. Simply speaking, charge symmetry is the symmetry under interchange of the u and d quarks [42]:

$$\begin{aligned} \hat{U}_{CS}\,|u\rangle &= -\,|d\rangle\,, \\ \hat{U}_{CS}\,|d\rangle &= |u\rangle\,. \end{aligned} \tag{1.13}$$

Charge symmetry breaking (CSB) manifests itself in many phenomena like the different scattering lengths in nn and pp systems after correcting for electromagnetic effects [43], neutron–proton elastic scattering at intermediate energies [44], $\pi - \eta$ mixing [45, 46], or the Nolen–Schiffer anomaly in the binding energy difference of ^{3}H and ^{3}He [47, 48]. In 1977 Weinberg predicted an effect of CSB in πN scattering [36]: the difference in the scattering lengths for $n\pi^0$ and $p\pi^0$ should be huge (up to 30%) and directly proportional to M_{pn}^{strong}. However, the direct measurement of $f(\pi^0 p) - f(\pi^0 n)$ in πN scattering is practically impossible experimentally, because of the lack of π^0 beams. Thus, there was the suggestion [49, 50] to use NN induced pion production as an alternative access to CSB pion–nucleon scattering. There have been three successful experiments in which the corresponding CSB observables were measured:

- the forward-backward asymmetry A_{fb} in the $np \to d\pi^0$ reaction [51],

- the total cross section of the reaction $dd \to {}^4$Heπ^0 near the threshold [52],

- the total and differential cross section of the reaction $dd \to {}^4$Heπ^0 at an excess energy of $Q = 60$ MeV [53].

The study presented in the thesis concentrates on a new measurement of the $dd \to {}^4$Heπ^0 reaction. In the next chapter the theoretical and experimental status of the CSB reactions presented above is discussed.

Chapter 2

Experimental and Theoretical Status

In this chapter a description of the experimental and theoretical status of three CSB observables — the forward-backward asymmetry A_{fb} in the $np \to d\pi^0$ reaction and the total and differential cross section of the reaction $dd \to {}^4\mathrm{He}\pi^0$ near the threshold — is presented. These observables provide an alternative access to CSB effects of the pion–nucleon scattering.

2.1 Forward-Backward Asymmetry in $np \to d\pi^0$

The forward-backward asymmetry A_{fb} of the $np \to d\pi^0$ reaction was measured at Canada's National Laboratory for Particle and Nuclear Physics TRIUMF. A neutron beam with an energy of 279.5 MeV was impinged on a proton target, corresponding to an excess energy, ε, of about $2\,\mathrm{MeV}$ [51]. A_{fb} is defined as:

$$A_{fb} = \frac{\int_0^{\pi/2} \left[\frac{\mathrm{d}\sigma}{\mathrm{d}\Omega}(\theta) - \frac{\mathrm{d}\sigma}{\mathrm{d}\Omega}(\theta - \pi) \right] \sin\theta \mathrm{d}\theta}{\int_0^{\pi/2} \left[\frac{\mathrm{d}\sigma}{\mathrm{d}\Omega}(\theta) + \frac{\mathrm{d}\sigma}{\mathrm{d}\Omega}(\theta - \pi) \right] \sin\theta \mathrm{d}\theta}, \tag{2.1}$$

where θ is the emission angle of the deuteron in the center of mass frame. In Fig. 2.1 the scheme of the $np \to d\pi^0$ reaction in the c.m. system before and after an interchange of u and d quarks is presented. The angle between the proton and deuteron before the interchange is equal to θ, and afterwards it is equal to $\pi - \theta$. Therefore, if the charge symmetry is broken, the differential cross section is not symmetric and $A_{fb} \neq 0$. The experimentally obtained value is $A_{fb} = [17.2 \pm 8(\mathrm{stat.}) \pm 5.5(\mathrm{syst.})] \cdot 10^{-4}$ [51]. The result has a quite big uncertainty: within two standard deviations of the statistical uncertainty it is compatible with zero.

The first theoretical calculations of A_{fb} based on a meson-exchange coupled-channel formalism are presented in [54]. It was predicted that $\pi - \eta$ mixing should completely dominate this observable. The calculated asymmetry $A_{fb} = -28 \cdot 10^{-4}$ is negative, contrary to the experimental result. First calculations based on χ_{PT} [49], where the CSB effects were modeled by a charge symmetry violating $\pi^0 N$ interaction, lead to a value of $A_{fb} = 60 \cdot 10^{-4}$ which is much larger than the one observed experimentally. Both calculations were performed before the results appeared describing mechanisms of isospin conserving pion production in the $NN \longrightarrow NN\pi$ reactions in χ_{PT} [55, 56]. These developments provided a good base for studying isospin violation
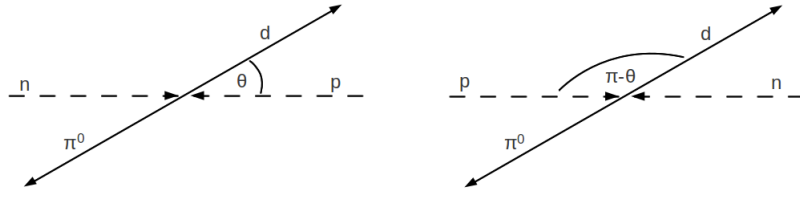
FIGURE 2.1: Scheme of $np \rightarrow d\pi^0$ reaction in the c.m. system, before (left) and after (right) an interchange of u and d quarks.

effects and brought the total cross section and the angular distribution into agreement with the experiment [50, 57]. It has been shown that at leading order (LO) A_{fb} is directly proportional to M_{pn}^{strong}, while the effect of $\pi - \eta$ mixing is subleading. The leading order diagram for the CSB s-wave amplitudes of the $np \rightarrow d\pi^0$ reaction is depicted in Fig. 2.2. From the experimental value of A_{fb}, M_{pn}^{strong} was obtained as

$$\Delta M_{np}^{strong} = 1.5 \pm 0.8(\text{exp.}) \pm 0.5(\text{th.}) \text{ MeV} . \tag{2.2}$$

This value is in agreement with lattice predictions [40] and the indirect extraction from $\Delta M_{pn}^{strong} = \Delta M_{pn} - \Delta M_{pn}^{em}$ [37, 39].
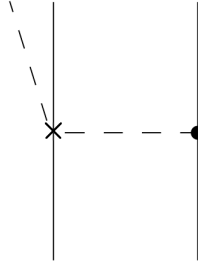
FIGURE 2.2: Leading order diagram for the CSB s-wave amplitudes of the $np \rightarrow d\pi^0$ reaction. The solid lines represent nucleons, the dashed lines denote pions, the cross indicates the CSB vertex and the dot represents a leading order charge invariant vertex. Source [50].

2.2 Total and Differential Cross Section of $dd \rightarrow {}^4\text{He}\pi^0$

2.2.1 $dd \rightarrow {}^4\text{He}\pi^0$ Cross Section Close to Threshold

The total cross section of the $dd \rightarrow {}^4\text{He}\pi^0$ reaction was first measured at the Indiana University Cyclotron Facility at two different beam energies. The results are $\sigma = 12.7 \pm 2.2$ pb and $\sigma = 15.1 \pm 3.1$ pb at 228.5 MeV and 231.8 MeV beam energy [52], respectively. In Fig. 2.3 the ${}^4\text{He}$ missing mass for $dd \rightarrow {}^4\text{He}X$ is presented. Each spectrum shows a prominent signal on top of a continuous background. The spectra

are described by a Gaussian peak and a continuum, presented as curves. The energy dependence of these results are comparable with s-wave pion production.
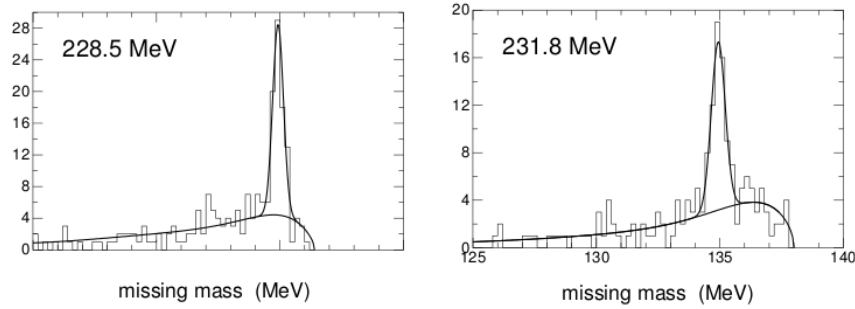
FIGURE 2.3: Candidate events at the two deuteron bombarding energies 228.5 MeV and 231.8 MeV as a function of the ^{4}He missing mass for $dd \rightarrow {}^4\text{He}X$. The smooth curves show the reproduction of these histograms with Gaussian peak and a continuum. Source [52].

2.2.2 Theory

When the charge symmetry operator acts on the particular hadronic states from the $dd \rightarrow {}^4\text{He}\pi^0$ reaction, one gets:

$$
\begin{aligned}
\hat{U}_{CS} \left| d \right\rangle &= \left| d \right\rangle, \\
\hat{U}_{CS} \left| {}^4\text{He} \right\rangle &= \left| {}^4\text{He} \right\rangle, \\
\hat{U}_{CS} \left| \pi^0 \right\rangle &= - \left| \pi^0 \right\rangle.
\end{aligned}
\tag{2.3}
$$

The $dd \rightarrow {}^4\text{He}\pi^0$ reaction violates charge symmetry because the system $^4\text{He}\pi^0$, odd under charge symmetry, should not be produced from the dd system, which is even under charge symmetry. Therefore, the total cross section is proportional to the CSB amplitude $|M_{CSB}|^2$.

First calculations for the $dd \rightarrow {}^4\text{He}\pi^0$ reaction can be found in [58, 59]. In [58] a simplified set of d and ^{4}He wave functions and a plane-wave approximation for the initial dd state were used. The ordering scheme of χ_{PT} was used to classify and identify different contributions. At leading order, there is only the contribution from πN re-scattering; no next-to-leading order contribution is identified. It occurred that the formally leading πN re-scattering term is suppressed due to selection rules in spin and isospin space. The contributions from next-to-next-to-leading order (NNLO) diagrams were too small to account for the observed cross section. It was shown that better agreement could only be obtained if short-range pion emission was taken into account.

More reliable calculations were performed in [59], where realistic two- and three-nucleon interactions in a χ_{PT} calculation were used. This allowed a proper treatment of the effects of the deuteron-deuteron interaction in the initial state and to use a realistic ^{4}He bound-state wave function. The contribution of the leading order term

for the s-wave channel is confirmed to be suppressed. The contributions at NNLO individually give results of the same order as the experimental cross section. This demonstrates the significant influence of the initial-state interaction. A complete calculation to NNLO — including pion loops and CSB in the initial state — is still under investigation.

The effects of initial-state Coulomb interactions were investigated in [60] using a simplified set of d and ^{4}He wave functions and a plane-wave approximation for the initial dd state. It was shown that the cross sections for $dd \rightarrow {}^4\text{He}\pi^0$ can be significantly enhanced by the soft photon exchange.

Furthermore, [61] shows that using parameters consistent with the CSB induced difference between the strong pp and nn scattering one can provide significant constraints on the calculated amplitude for the $dd \rightarrow {}^4\text{He}\pi^0$ reaction. However, the result is very sensitive to the choice of the nuclear potential model, which demonstrates that a simultaneous analysis of the NN scattering length and the $dd \rightarrow {}^4\text{He}\pi^0$ reaction is needed.

There is one more important test for the theoretical description of the CSB observables. At NNLO the first counter term enters the s-wave pion production with unknown strength $\bar{D}$. In addition, the isospin violating πNN coupling constant β_1 contributes. The reaction $dd \rightarrow {}^4\text{He}\pi^0$ near threshold can be used together with the forward-backward asymmetry in $np \rightarrow d\pi^0$ to NNLO to fix $\bar{D}$ and β_1 (the required evaluation of the transition operator to one loop is in progress). Once the parameters are fixed, the p-wave contribution can be predicted parameter-free to leading and next-to-leading order, which will provide an important cross-check for the χ_{PT} predictions [62].

In Fig. 2.4 some formally leading operators for p-wave pion production are presented. The coupling strengths are given by the leading CSB πN amplitude (Fig. 2.4 a) and the leading CSB πNN vertex (Fig. 2.4 b and 2.4 c). However, as for the s-wave pion production, the contribution of diagram (a) is suppressed as a consequence of selection rules. Therefore, p-wave pion production provides direct access to the CSB πNN coupling constant β_1. A measurement of the p-wave contribution in $dd \rightarrow {}^4\text{He}\pi^0$ is therefore complementary to the $np \rightarrow d\pi^0$ measurement from [51] which is mostly sensitive to the leading isospin violating πN amplitude [62].

In addition, higher partial waves are predicted to be sensitive to the CSB $NN \longrightarrow N\Delta$ transition potential which is difficult to access in other reactions. This potential is known in chiral perturbation theory in LO. Therefore, the measurement of higher partial waves provides an additional non-trivial test of the understanding of isospin violation in hadronic reactions [53].

2.2.3   Charge Symmetry Breaking with WASA-at-COSY

The investigation of higher partial waves of the pion production in the $dd \rightarrow {}^4\text{He}\pi^0$ reaction at $\varepsilon = 60$ MeV is one of the main goals of the WASA-at-COSY experiment. The program started with the measurement of the isospin conserving $dd \rightarrow {}^3\text{He}n\pi^0$
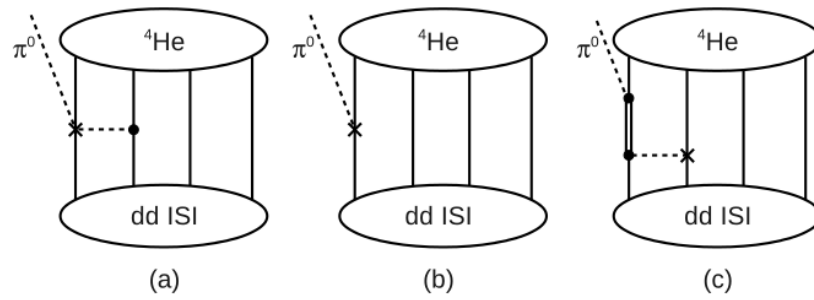
FIGURE 2.4: Formally leading operators for p-wave pion production in $dd \to {}^4He\pi^0$. The crosses indicate the occurrence of CSB, the dots represent a leading order charge invariant vertex. The dashed lines denote pions, the single solid lines denote nucleons and the double solid lines denote a Δ. Source [63].

reaction, which provides important experimental input for calculations of the initial-state interactions. As a next step, a first measurement of $dd \to {}^4He\pi^0$ was performed.

Measurement of the $dd \to {}^3Hen\pi^0$ Reaction

The theoretical control over the initial-state interactions is one of the biggest challenges in the calculation describing the $dd \to {}^4He\pi^0$ reaction. Therefore, as an experimental input, high accuracy wave functions for $dd \to 4N$ in low partial waves at relatively high energy are needed. Therefore, the first part of the CSB program was the measurement of the isospin symmetry conserving reaction $dd \to {}^3Hen\pi^0$ [64], as this reaction partially shares the same partial waves in the initial state with $dd \to {}^4He\pi^0$.

The analysis was performed using data collected during a one-week run in November 2007, at a beam momentum of $p_d = 1.2\,\text{GeV}/c$ ($E_d = 350\,\text{MeV}$), which is the same energy as the $dd \to {}^4He\pi^0$ run. The goal was to measure the total and differential cross section of the $dd \to {}^3Hen\pi^0$ reaction in order to provide first experimental data on the dd initial state for s and p partial waves.

As a result the total cross section of the $dd \to {}^3Hen\pi^0$ reaction was obtained:

$$\sigma_{\text{tot}} = (2.89 \pm 0.01(\text{stat.}) \pm 0.06(\text{syst.}) \pm 0.29(\text{norm.}))\ \mu\text{b}. \qquad (2.4)$$

The differential distributions have been compared to a *quasi*-free reaction model and a partial-wave expansion for the three-body reaction limited to at most one p-wave in the final state, both added incoherently. The contribution of the *quasi*-free processes is about 1.11 μb of the σ_{tot}, which is in agreement with model predictions. The conclusion from the partial wave decomposition was that p-wave contributions in the final state are significant, but that there are no significant contributions from higher partial waves [64].

First $dd \rightarrow {}^4\text{He}\pi^0$ Measurement with WASA-at-COSY

In June 2008 a first two-week long high-luminosity run dedicated to the measurement of the $dd \rightarrow {}^4\text{He}\pi^0$ reaction took place. The main goal of this experiment was to obtain the total cross section at $p_d = 1.2\,\text{GeV}/c$ ($E_d = 350\,\text{MeV}$) [53]. In Fig. 2.5 the final missing mass plot is presented. On a flat, broad background coming from double radiative capture $dd \rightarrow {}^4\text{He}\gamma\gamma$, two significant peaks are visible. The first, coming from the signal reaction $dd \rightarrow {}^4\text{He}\pi^0$, is located at $m_\pi = 135$ MeV. The second one corresponds to misidentified events from the background reaction $dd \rightarrow {}^3\text{He}n\pi^0$, which is shifted because of the ${}^3\text{He} - n$ binding energy. The data have been fitted with Monte Carlo filtered distributions for all three contributions. For the $dd \rightarrow {}^4\text{He}\gamma\gamma$ channel a homogeneous 3-body phase-space distribution has been assumed, for the $dd \rightarrow {}^3\text{He}n\pi^0$ contribution the obtained model from [64] has been used, and the contribution of the $dd \rightarrow {}^4\text{He}\pi^0$ reaction is based on the 2-body phase-space. The obtained total cross section is equal to [53]:

$$\sigma_{\text{tot}}^{{}^4\text{He}\pi^0} = (118 \pm 18(\text{stat.}) \pm 13(\text{syst.}) \pm 8(\text{ext.}))\ \text{pb}. \tag{2.5}$$

Dividing out the phase space in initial and final state, the result can be compared with the values measured close to threshold (see Fig. 2.6). A constant value could indicate dominating s-wave, but one has to keep in mind that the energy dependence of the ${}^4\text{He}$ formation in the final state is not included here. In addition, a first result for the angular distribution was obtained. Fig. 2.7 shows the extracted differential cross section as a function of $\cos\theta^*$ (θ^* is the polar angle of the π^0 in the c.m. system). Due to identical particles in the initial state the angular distribution must be symmetric with respect to 0. Taking into account the statistical uncertainty, the result is not decisive in identifying contributions from higher partial waves [53].

The measurement described in this thesis is the next stage of the WASA-at-COSY program. The goal is to obtain the differential cross section with better statistics and improved accuracy. An eight-week long run with a modified detector setup was carried out in spring 2014. The aim of the detector modification and description of the experimental conditions are presented in Sec. 3.2.
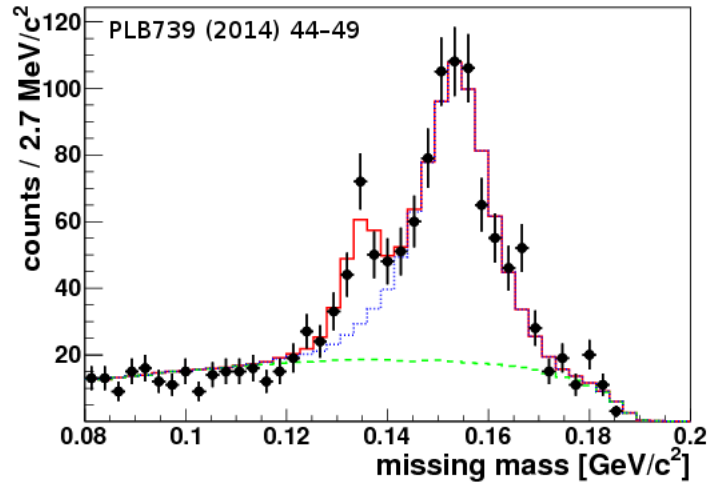
FIGURE 2.5: Missing mass plot for the reaction $dd \rightarrow {}^4\text{He}X$ at $p_d = 1.2\,\text{GeV}/c$. The different contributions fitted to the spectrum are double radiative capture $dd \rightarrow {}^4\text{He}\gamma\gamma$ (green dashed), the reaction $dd \rightarrow {}^3\text{He}n\pi^0$ (blue dotted, added) and the sum of all contributions including the signal (red solid). Source [53].
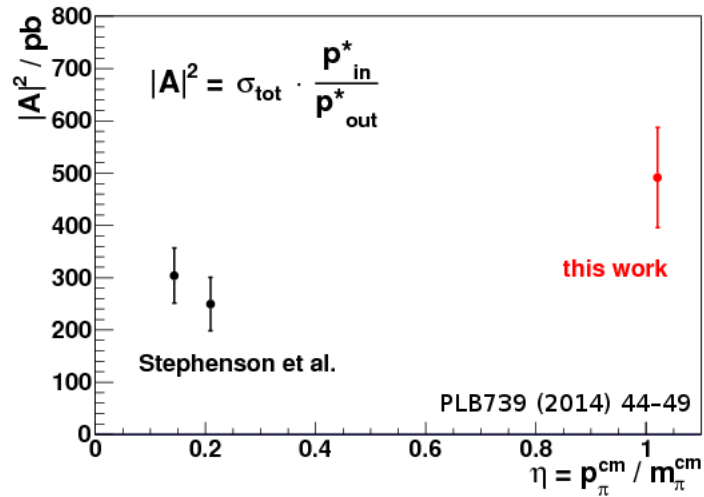
FIGURE 2.6: Energy dependence of the $dd \rightarrow {}^4\text{He}\pi^0$ reaction amplitude squared $|A|^2$. In the absence of initial- and final-state interactions a constant amplitude would indicate that only s-wave is contributing. The red full circle corresponds to the total cross section given in 2.5. Source [53].
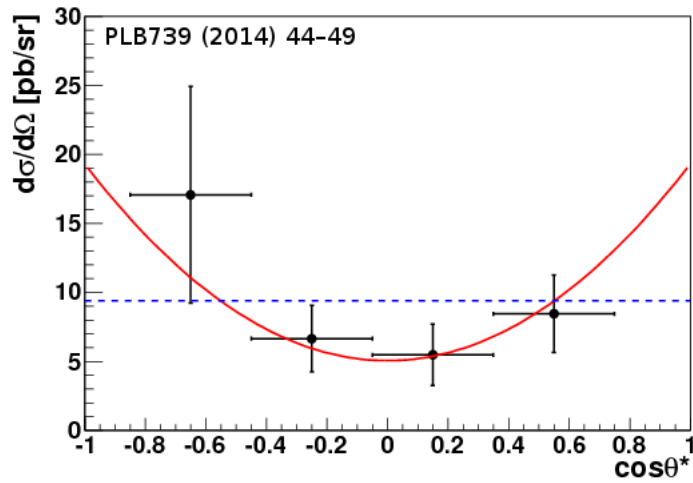
FIGURE 2.7: Differential cross section of $dd \to {}^4\mathrm{He}\pi^0$ at $p_d = 1.2\,\mathrm{GeV}/c$. The error bars show the statistical uncertainties. In the first bin an additional systematic uncertainty has been added. The blue dashed line represents the total cross section assuming an isotropic distribution, the solid red curve shows the fit with the Legendre polynomials P_0 and P_2. Source [53].

Chapter 3

Experiment

The experiment described in this thesis was performed at the Institute for Nuclear Physics at the Forschungszentrum Jülich located in Germany. The following setup was used:

- **Detector**: modified version of the Wide Angle Shower Apparatus (WASA).

- **Target**: deuteron pellets, provided by the WASA pellet target system.

- **Beam**: high intensity deuteron beam with a momentum of $p_d = 1.2\,\text{GeV}/c$ ($E_d = 350\,\text{MeV}$), provided by the Cooler Synchrotron COSY.

COSY is described in Sec. 3.1, the WASA detector system together with the pellet target and the trigger system is presented in Sec. 3.2, and the run conditions are summarized in Sec. 3.3.

3.1 Cooler Synchrotron COSY

The COSY facility is presented schematically in Fig. 3.1. It consists of ion sources for polarized and unpolarized beam, the injector cyclotron JULIC (Jülich Isochronous Cyclotron), injection and extraction lines, and the COSY ring. Experiments can be performed using either the internal beam of COSY or an extracted beam at external target stations. The circumference of the COSY ring is 184 m. The straight sections are 40 m long and the arcs are 52 m long [65, 66].

The accelerator facility can provide polarized and unpolarized beams of protons and deuterons. First H^- (D^-) ions provided by an ion source are pre-accelerated to a momentum of 0.29 GeV/c (0.54 GeV/c) in the injector cyclotron JULIC. Then, the electrons are stripped off using a carbon foil. Finally, the protons or deuterons are injected into the COSY ring, stored, and accelerated further to the desired momentum (0.295 GeV/c - 3.7 GeV/c). The part of the cycle when the particles are stored for a certain time is called "flat top". To start a new cycle, at the end of the flat top, the dipole magnets are ramped down and the beam is dumped [66].

In order to reduce the phase space volume of the beam, two cooling mechanisms can be used. Electron cooling [67] is used for the low momentum range, up to 600 MeV/c. For momenta above 1.5 GeV/c stochastic cooling [68] is available. In

addition to cooling, a barrier bucket cavity [69] can be used to compensate the mean energy loss in the beam caused by beam-target interactions. This is especially important for target densities of about 10^{15} atoms/cm^2 as with the WASA target (see Sec. 3.2.1). For unpolarized protons or deuterons the maximum number of particles in the beam is about $10^{10} - 10^{11}$, while for polarized beams it is about one order of magnitude smaller. This corresponds to typical luminosities of 10^{31} to 10^{32} cm^{-2}s^{-1} achieved with the WASA target system [70].

3.2   WASA Detector System

The Wide Angle Shower Apparatus (WASA) was originally installed at the CELSIUS storage ring in Uppsala, Sweden [72]. In 2005, WASA was moved to Jülich, Germany, and assembled at the COSY ring in the form which is described in [71]. It was operating in Jüich from 2006 to 2014.

The WASA facility was designed to study the production and decays of light mesons. It allows to identify and fully reconstruct both charged and neutral particles. It has a geometrical acceptance close to 4π and can handle high luminosities, up to 10^{32} cm^{-2}s^{-1} [71]. The detector setup consists of three major parts, namely, the pellet target system, the Forward Detector (FD), and the Central Detector (CD). The beampipe goes through the whole detector setup and crosses perpendicularly the pellet target tube in the middle of the Central Detector.

At the end of 2013 the detector setup was modified. A sketch of WASA is presented in Fig. 3.2 (modified version) and Fig. 3.3 (original version).

The reason for the modification was the experiences gained during the first measurement of the $dd \rightarrow {}^4\text{He}\pi^0$ reaction, (see Sec. 2.2.3), which was performed with the original setup (for details see [73]). The main goal was to add a time-of-flight measurement of forward going particles to the so-far energy-loss based particle reconstruction. Thus, all the detectors between the Forward Proportional Chamber and the Forward Veto Hodoscope were removed (see the comparison between Fig. 3.2 and Fig. 3.3). This allows the slow ^4He from the $dd \rightarrow {}^4\text{He}\pi^0$ reaction to reach the last layer of the Forward Veto Hodoscope, instead of being stopped in the first scintillator layer after the Forward Proportional Chamber. The analysis of the time-of-flight information allows for

- a better separation of the $dd \rightarrow {}^4\text{He}\pi^0$ and $dd \rightarrow {}^3\text{He}n\pi^0$ reactions,

- an independent method for detector calibration (so far, the calibration of the energy deposit in the thin plastic scintillators was based only on the correlation of the energy loss in the different layers),

- and a more accurate kinetic energy reconstruction of ^4He and ^3He.

In the following section the modified WASA facility is described in more details.
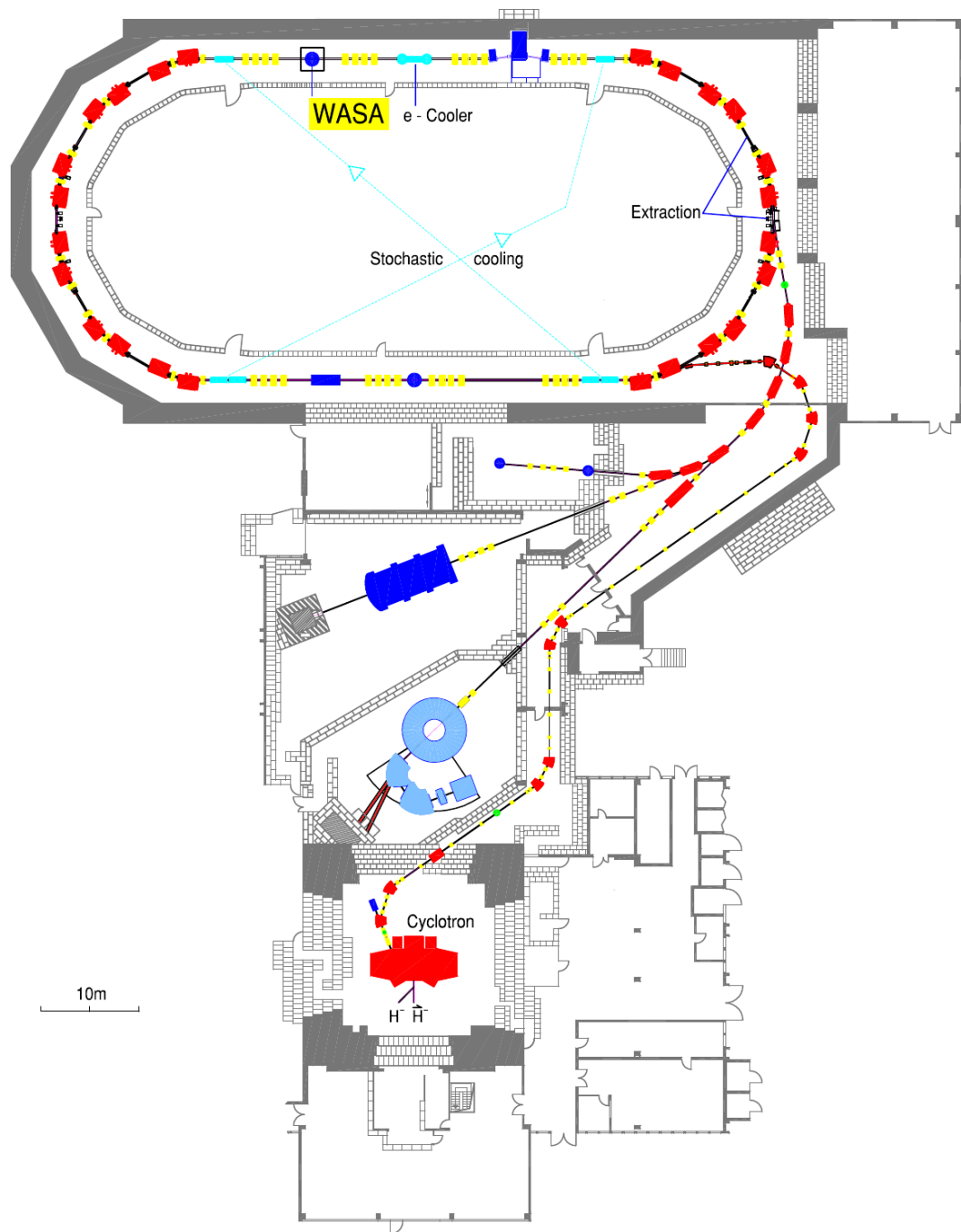
FIGURE 3.1: Schematic view of the COSY facility. The ion sources, the injector cyclotron, the injection and extraction lines, and the COSY ring are visible. The position of the WASA detector setup is marked. Adapted from [71].
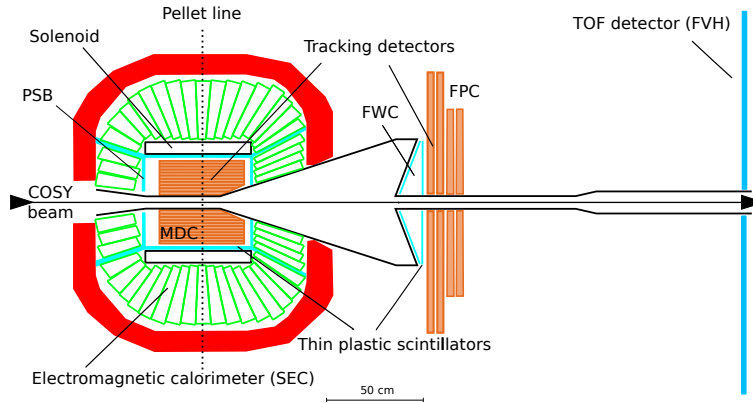
FIGURE 3.2: Schematic side view of the WASA detector setup. The Forward Detector consists of two layers of the Forward Window Counter (FWC), four planes of the Forward Proportional Chamber (FPC) and one layer of the Forward Veto Hodoscope (FVH). In the Central Detector a tracking detector, called Mini Drift Chamber (MDC), is surrounded by the Plastic Scintillator Barrel (PSB), the solenoid, and the Scintillator Electromagnetic Calorimeter (SEC). The most outer part of the Central Detector is the iron yoke (marked in red). The COSY beam enters the detector setup from the left side. Adapted from [71].
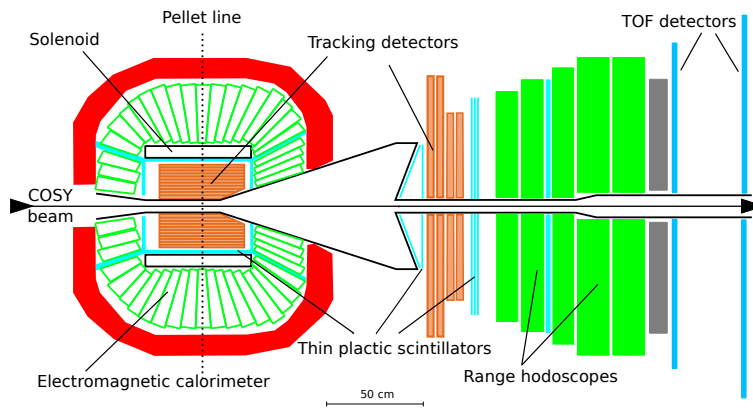
FIGURE 3.3: Previous WASA detector setup as described in [71]. All the detectors between the Forward Proportional Chamber and the Forward Veto Hodoscope were removed during the modification in 2013.

3.2.1 Pellet Target

The pellet target system can provide frozen pellets of hydrogen and deuterium with a diameter between $25 - 35$ μm, a frequency about $5 - 12$ kHz, and a velocity about 60 m/s at the interaction point. The achievable effective target thickness is about 10^{15} atoms/cm^2, which is necessary to obtain luminosities as high as 10^{32} cm^{-2}s^{-1}. The spread of the pellet stream at the interaction point is about $2 - 4$ mm [71, 74]. Detailed information about the system can be found in [74–79].

The layout of the pellet target system is shown in Fig. 3.4. In the pellet generator, hydrogen or deuterium gas is liquefied in a heat exchanger. Then, it is pressed through

a glass nozzle. The temperature of hydrogen is about 15 K and of deuterium is about 20 K, while the pressure of both is kept at a level of 600 mbar [79]. The jet of liquid hydrogen or deuterium is then broken up in droplets using a vibrating nozzle. The droplets pass through the droplet chamber, where the pressure is slightly below the triple point value (20 mbar for hydrogen and 60 mbar for deuterium), to reach a 7 cm long vacuum-injection capillary where their surfaces freeze by evaporation. Then, they cool down further and freeze to solid spheres in the skimmer chamber, because of a pressure reduction up to 10^{-3} [77, 80]. The stream of pellets is collimated passing through a skimmer. Then, it reaches a 2 m long pipe which leads to the scattering chamber. At the interaction region the beampipe crosses the pellet target tube. After that, the pellets are directed to a beam dump where pumps remove the gas from the evaporating pellets.
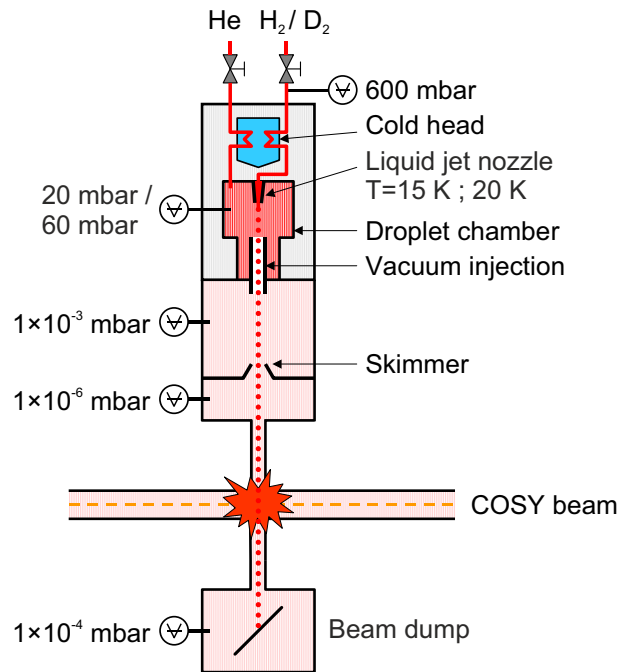
FIGURE 3.4: Scheme of the pellet target system. The main components and information about the pressure and the temperature values in the particular parts of the system are marked. Source: [79].

3.2.2 Forward Detector

The purpose of the Forward Detector (FD) is the detection and identification of charged recoil particles like protons, deutrons, and helium nuclei with polar angles between $3°$ and $18°$. It consists of two layers of thin plastic scintillators (the Forward Window Counter (FWC)), four layers of a straw tube detector (the Forward Proportional Chamber (FPC)), and one layer of the time-of-flight (ToF) detector — the Forward Veto Hodoscope (FVH). In the following these FD components are discussed.

Forward Window Counter

The two layers of the FWC are located just after the exit window of the scattering chamber. While the second layer is perpendicular to the beam direction, the first one is titled by $20°$ to fit to the shape of the exit window. Each layer is built of 3 mm thick plastic scintillators made of BC408. Both layers consist of 24 elements. One layer is rotated with respect to the other one by half of an element, resulting in an effective granularity of 48 elements. A sketch of the detector is presented in Fig. 3.5. More details on the FWC can be found in [81].

Plastic scintillators consist of scintillating molecules or atoms suspended in an organic material to form a polymerizing structure. Charged particles passing through a scintillator cause an excitation of the atoms or molecules, which produces a flash of light when going back into the ground state. The light is usually detected by photomultipliers. Plastic scintillators can be produced in almost any geometry. Characterized by a fast rise time they can provide excellent timing information used for time-of-flight [82].

The FWC plays an important role in the trigger logic, reducing the background caused by secondary interactions in the beam-pipe or in the flange at the exit of the scattering chamber. Events with time-coincident hits in geometrically overlapping elements in both layers will trigger the data acquisition. In addition, in the presented experiment, the FWC is also used to separate ^{3}He and ^{4}He isotopes from protons and deuterons, by introducing a high threshold for the energy deposit in the trigger. For the off-line analysis the detector provides timing information of charged particles used to measure time-of-flight. It can also be used for particle identification by means of methods based on a correlation between energy losses in different detector layers (dE-dE) or a correlation between time-of-flight and energy losses (ToF-dE).
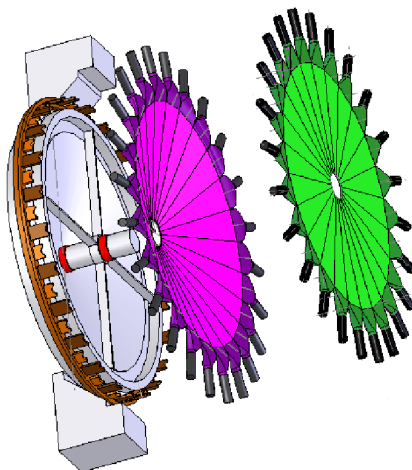
FIGURE 3.5: Sketch of the two layers of the Forward Window Counter. The scintillator layers and the scattering window are separated in an explosion view. Source: [81].

Forward Proportional Chamber

Behind the FWC the Forward Proportional Chamber is located, which is composed of 4 planes. Each plane consists of 4 staggered layers of 122 straws of 8 mm diameter. All planes are oriented perpendicularly to the beam direction. They are rotated by -45, $+45$, 0 and 90 degree, respectively (see Fig. 3.6). The drift tubes are made of aluminized Mylar foil with a central sense wire made of stainless steel [83]. A mixture of 80% Ar, as a proportional gas, and 20% C_2H_6, as a quenching gas, is used [84].

The principle of the particle detection in a straw tube tracker is the following: every straw tube is a proportional drift tube, with the central steel wire as anode and the Mylar foil as cathode. When a charged particle crosses the straw it ionizes the gas. The primary electrons from the gas ionization are accelerated in the strong electrical field in the vicinity of the wire and they move towards the anode. The intensity of the field is $E \propto r^{-1}$, where r is a distance from the wire. If the primary electrons gain a sufficient amount of energy they ionize further gas atoms by colliding with them. This releases additional electrons which accelerate and collide with further atoms, releasing more electrons. It leads to an electron avalanche. The resulting cascade of electrons eventually reaches the anode and induces a current. While the ion cloud slowly drifts to the cathode, the signal induced by electrons is very fast and can be used for precise reconstruction of the trajectory of a traversing particle [82].

The purpose of the FPC is to provide the azimuthal and polar direction of particles coming from the interaction region. The precision of the scattering angles measured with the FPC is below $0.2°$ [83–85].

(A) (B)
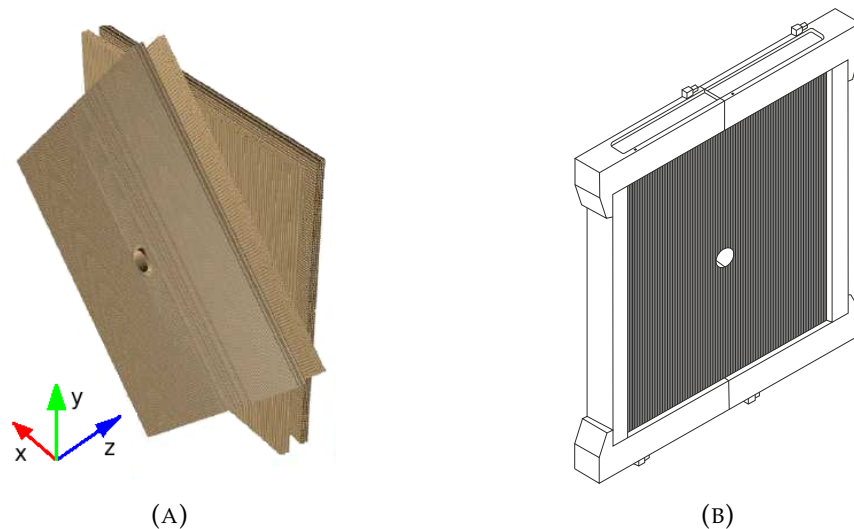
FIGURE 3.6: Schematic view of the Forward Proportional Chamber. Adapted from [86]. A: Three dimensional view of four modules of FPC. The system of coordinates is marked. B: The single FPC module in a frame. Source: [79].

Forward Veto Hodoscope

The Forward Veto Hodoscope is the most forward layer of the FD. It consists of 24 bars of the plastic scintillator EJ200. The elements are 12 cm wide and 20 mm thick. 22 of them are mounted vertically, 2 additional ones are located horizontally at the back side of the detector for calibration purposes. Each bar has photomultipliers at both ends. The three outer bars on each side are 190 cm long, the others are 260 cm long. Because of the beam pipe the central element is divided in two parts, above and below the pipe. A schematic view of the FVH is presented in Fig. 3.7. More information about the FVH can be found in [81, 87].

Due to the two-sided readout the location of the hit along a detector element can be also reconstructed by measuring the time difference of both signals. Together with the FWC detector, it is used to measure the time-of-flight of outgoing particles from the interaction region. The energy loss information from the FVH can be used for particle identification.
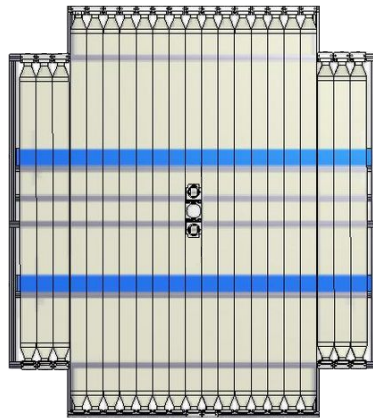
FIGURE 3.7: Schematic view of the Forward Veto Hodoscope. Adapted from [87].

3.2.3 Central Detector

The Central Detector surrounding the interaction point is designed for the detection and identification of meson decay products, namely, photons, electrons, muons and charged pions in the polar angular range between $20°$ and $169°$ and with full coverage of the azimuthal angle. It consists of the Mini Drift Chamber (MDC), the Plastic Scintillator Barrel (PSB) (thin plastic scintillators arranged as a cylinder surface), the Superconducting Solenoid (SCS) providing the magnetic field surrounded by the iron yoke, and the Scintillator Electromagnetic Calorimeter (SEC).

The Central Detector is crossed by the beampipe and the pellet target tube. In the interaction region, the beampipe is made of beryllium and has a radius of 30 mm and a wall thickness of 1.2 mm [71].

Since the measurement presented in the thesis does not require any charged particle detection in the Central Detector, the Superconducting Solenoid had been switched off. In the solenoidal field the transverse component of the particle momentum due to betatron oscillations causes a phase space mixing between x and y components of the COSY beam (rotation of the beam). As the acceptance of the COSY ring is not symmetric in x-axis, it is easier to reach higher beam currents with a switched-off solenoid. In the current measurement also the Mini Drift Chamber was not used as no charged particles were to be detected and the magnetic field was off. However, for completeness the description of these two components of the Central Detector is included in this section.

Mini Drift Chamber

The Mini Drift Chamber is the innermost part of the CD. This tracking detector consists of 1738 straw tubes arranged in 17 cylindrical layers. In order to get three-dimensional information about the trajectory of the particles, nine layers consist of straws parallel to the beam axis, and the other eight consist of tubes tilted by an angle in the range between $6° - 9°$ with respect to the beam axis. Each straw tube is made of $25\,\mu$m thin aluminized mylar foil and a sensing wire made of $20\,\mu$m gold-plated tungsten. The tubes are filled with a mixture of argon and ethane in the proportion 8:2. A schematic view of the MDC surrounded by the Plastic Scintillator Barrel is presented in Fig. 3.8. A detailed description of the MDC can be found in [88].

The purpose of the MDC is the three-dimensional track reconstruction of charged particles in the polar angular range of $24° - 159°$. The momentum vector of charged particles is determined from the curvature of the track in the magnetic field.
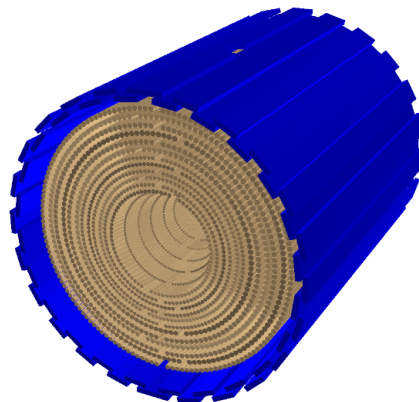
FIGURE 3.8: Schematic view of the Mini Drift Chamber (brown) surrounded by the Plastic Scintillator Barrel (blue). Source [79].

Plastic Scintillator Barrel

The Plastic Scintillator Barrel surrounds the MDC. It consists of three parts, the cylindrical central one and the two end caps which are shown in Fig. 3.9. Such a structure allows a nearly 4π coverage. The PSB is build of 146 plastic scintillator elements (BC408) with a thickness of 8 mm. The central part consists of 50 strips with a length of 55 cm and width of 3.8 cm. Two of them are split in half to provide space for the pellet tube. Each element overlaps with the neighboring ones to increase the geometrical acceptance. Every end cap is build of 48 trapezoidal elements. The front end cap is flat and has a hole for the beampipe with diameter of 19 cm, while the rear cap forms a conical surface with the beampipe hole with a diameter of 12 cm. All scintillators are connected via light guides with photomultipliers located outside the iron yoke to shield them from the magnetic field. More information on the PSB can be found in [88, 89].

The information from the PSB is used to discriminate between neutral and charged particles on the trigger level as well as in the off-line analysis. The energy loss measured in the PSB is used to identify charged particles, together with the momentum measured in the MDC or the energy deposit in the electromagnetic calorimeter.
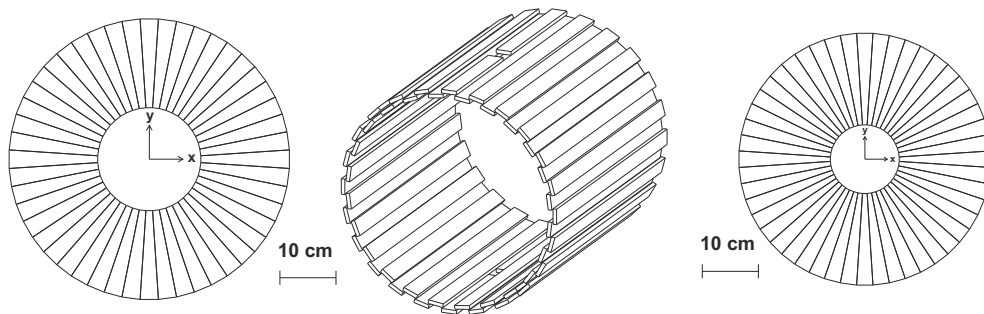
FIGURE 3.9: Sketch of the forward, central and backward part of the Plastic Scintillator Barrel. In the end caps the beampipe holes are visible. Source [71].

Superconducting Solenoid

In order to measure the momenta of charged particles using the information from the MDC, an axial magnetic field is needed. It is provided by the Superconducting Solenoid, which is able to produce magnetic fields up to 1.5 T. A map of such a magnetic field is presented in Fig. 3.10 The coil is operated at a temperature of 4.5 K provided by a liquid helium cooling system. The magnetic flux is closed by a five ton iron yoke. It shields the readout electronics and photomultipliers from the inner magnetic field and provides the support for the calorimeter. A detailed description of the SCS can be found in [90].
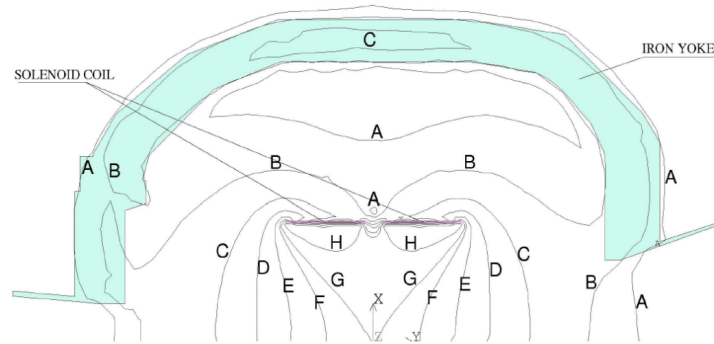
FIGURE 3.10: Map of the magnetic field produced by the Superconducting Solenoid. Border contours are indicated by lines with the labels A – H to describe field density: A = 0.10 T, B = 0.25 T, C = 0.50 T, D = 0.75 T, E = 1.00 T, F = 1.20 T, G = 1.30 T, H = 1.50 T. Source [90].

Scintillating Electromagnetic Calorimeter

The Scintillating Electromagnetic Calorimeter is the most outer layer of the Central Detector. It consists of 1012 sodium-doped CsI crystals supported by the iron yoke, organized in 24 rings. The crystal length varies from 20 cm in the backward region to 30 cm in the central part and 25 cm in the front one. Each crystal is connected to a photomultiplier outside the iron yoke via a light guide. The SEC covers a polar angular range of $20° - 169°$. A schematic view of the SEC is presented in Fig. 3.11.

The calorimeter is used to measure the energy of outgoing photons, electrons and pions. For the purpose of this thesis, the SEC was only used for photons from the π^0 decay. More details about this detector can be found in [71, 91, 92].

If a photon enters a scintillating crystal it starts an electromagnetic shower. The shower is dominated by pair production and bremsstrahlung. The created light is collected by photomultipliers and converted into an electric signal.

The scintillation mechanism in inorganic materials can be described by the band structure in the crystals. A particle crossing through a crystal can excite an electron from the valence band into the conduction band. In the conduction band electrons move freely. They can recombine with a hole or create a bound state with a hole called exciton. The excitation energy level is slightly below the conduction band. The exciton migrates in the crystal for some time. Then, it deexcites in a collision with a phonon or recombines emitting a photon with the excitation energy, which can be detected. Additionally, a dopant can be introduced in the lattice of the scintillating crystal. It creates an additional energy level between the valence and the conduction band and increases the probability of exciton recombination at room temperature [82].

3.2.4 Data Acquisition System

The Data Acquisition System (DAQ) processes signals from the detectors and makes them available for data analysis. The hierarchical structure of the WASA DAQ system
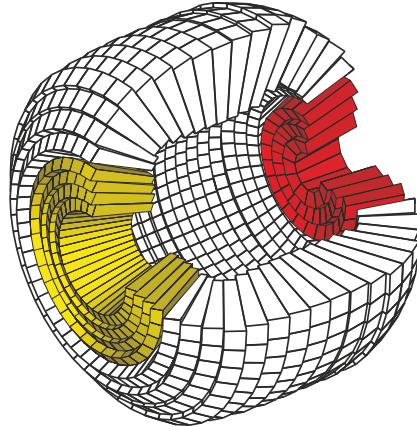
FIGURE 3.11: Schematic picture of the Scintillating Electromagnetic Calorimeter. The forward part is marked in yellow, the central part in white, and the backward part in red. Source [71].

is presented in Fig. 3.12. It is designed to handle high event rates (of about 10 kHz) when running at high luminosity [93, 94].

The signals from the straw tubes and photomultipliers are sent to front-end electronics (preamplifiers, splitters, discriminators). The signal from the front-end electronics is then sent to the digitalization modules. The evaluation of the digitized signals is done by a Field-Programmable Gate Array (FPGA). In these modules the whole digitalization system consists of 14 crates equipped with QDCs (Charge-to-Digital Converter) and TDCs (Time-to-Digital Converter). They continuously sample the data stream, and store the detected signals in a FIFO (First In First Out) buffer. Signal selection and evaluation in the FPGAs start when the trigger arrives, using a pre-defined time window. The memory of the digitalization modules is large enough to store the history of data and avoid a separate delay of the signals. A synchronization system synchronizes the time signal of the trigger and the modules and assigns event numbers. When a trigger is sent by the synchronization system to the individual crates, the leading edge of the signal is used as a reference time in the crates to assign a time stamp relative to the trigger to all stored signals. The final data are transfered to a readout computer farm. There, an event builder collects the data streams and writes it to disk [93].

3.2.5   Trigger

In general, the WASA trigger is based on the information from the scintillating detectors in the Forward as well as in the Central Detector. This includes hit multiplicities, time coincidences, and geometrical overlap between the detector elements. From the calorimeter the cluster multiplicity, the energy of the cluster and the total energy sum in the calorimeter can be used. The cluster type (charged or neutral) can be determined by including the information from the PSB. Several trigger conditions can be logically combined to optimize the selection of the data sample [95, 96].
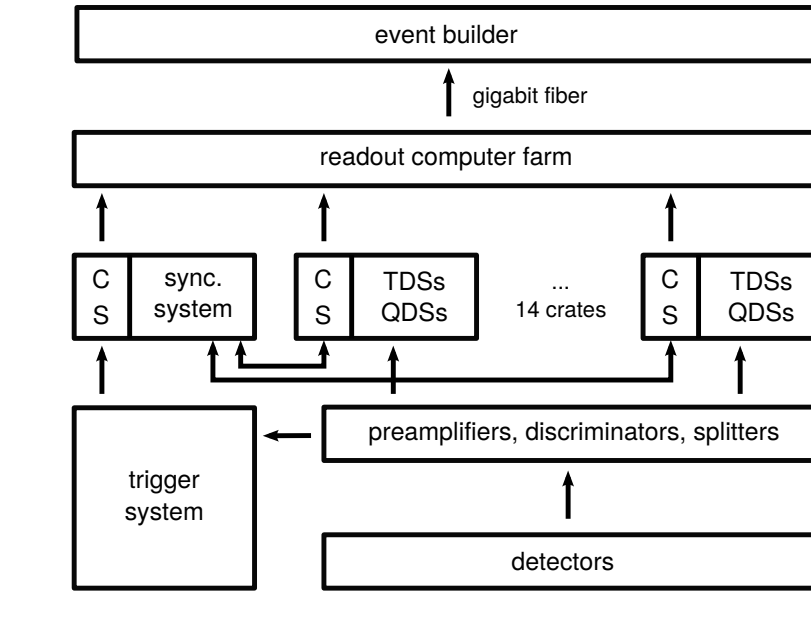
FIGURE 3.12: Structure of the DAQ system of the WASA detector. Figure adapted from [93].

For the $dd \rightarrow {}^4\text{He}\pi^0$ reaction the main trigger was:

```
fwHea1 & fwHeb1 & seln1
```

meaning the following:

1. `fwHea1 & fwHeb1` - a high threshold (corresponding to a high energy deposit) was required for signals from at least one element of the first and the second layer of Forward Window Counter AND

2. `seln1` - at least one cluster originating from a neutral particles (i.e., no geometrical overlap with a PSB hit) in the Central Detector.

For the first trigger requirement, the high thresholds in FWC1 and FWC2 (first and second layer of FWC, respectively) were adjusted at the beginning of the beamtime such that the $dd \rightarrow {}^3\text{He}n$ reaction used for the calibration purposes (see Sec. 4.3), the signal reaction $dd \rightarrow {}^4\text{He}\pi^0$, and the $dd \rightarrow {}^3\text{He}n\pi^0$ reaction used for luminosity determination (see Chapter 6) were included in the trigger. In Fig. 3.13 an example spectrum of the energy loss in QDC channels is presented for element 13 of FWC1. In the plot, the high trigger threshold is marked with a green line. The prominent peak around channel 5000 originates from ${}^3\text{He}$ from $dd \rightarrow {}^3\text{He}n$. The energy losses of ${}^3\text{He}$ and ${}^4\text{He}$ from $dd \rightarrow {}^3\text{He}n\pi^0$ and $dd \rightarrow {}^4\text{He}\pi^0$ are above that peak.

3.3 Run Summary

The data were collected in an eight-week long run between 17.02.2014 and 21.04.2014. A deuteron beam at a kinetic energy of $E_{kin} = 0.350\,\text{GeV}$ ($p_d = 1.2\,\text{GeV}/c$) was scattered on deuterium pellets.
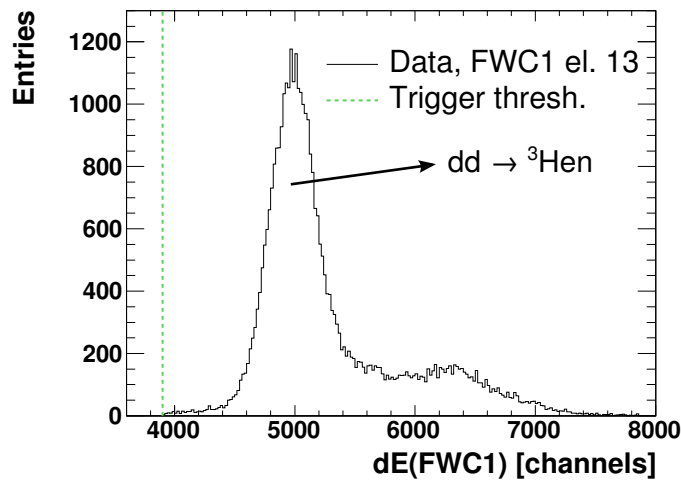
FIGURE 3.13: Energy loss for element 13 of FWC1. The high trigger threshold is marked with a green dashed line. The prominent peak around channel 5000 originates from ^{3}He from the $dd \to {}^3\mathrm{He}n$ reaction. the energy losses of ^{3}He and ^{4}He from $dd \to {}^3\mathrm{He}n\pi^0$ and $dd \to {}^4\mathrm{He}\pi^0$ are above that peak.

The typical accelerator cycle was 50 s long, while the effective time of data taking was 41 s. The time structure of the cycle is presented in Tab 3.1.

TABLE 3.1: Beam cycle structure.

Time in cycle [s]	Action
0	Start of cycle
2.5	High voltage of MDC and FPC switched on
5	Barrier bucket switched on
5.5	Pellet target and DAQ switched on
46.5	Pellet target and HV switched off
48	WASA DAQ switched off
49	Barrier bucket switched off
50	End of cycle

The pellet rate and the beam current as a function of time in one example cycle is presented in the left panel of Fig. 3.14. On a longer time scale the pellet rate was varying between $1500 - 11000$ Hz, but was not changing significantly within a cycle. The number of deuterons in the flat top (right after injection and acceleration) was between $1.9 - 2.5 \cdot 10^{10}$. While interacting with the target, the beam current dropped by $50 - 80\%$. In the right panel of Fig. 3.14 the ratio of incoming to accepted triggers during the cycle is shown, representing the efficiency of the data acquisition system. The ratio grows from about 85% at the beginning of the cycle, to about 100% at the end. It is caused by the fact that due to the dropping beam current the luminosity was

highest at the beginning of cycle. With very high luminosities the data acquisition system cannot process all trigger events because of the dead time linked to the conversion time of the analog-to-digital converters and the readout and storage times.
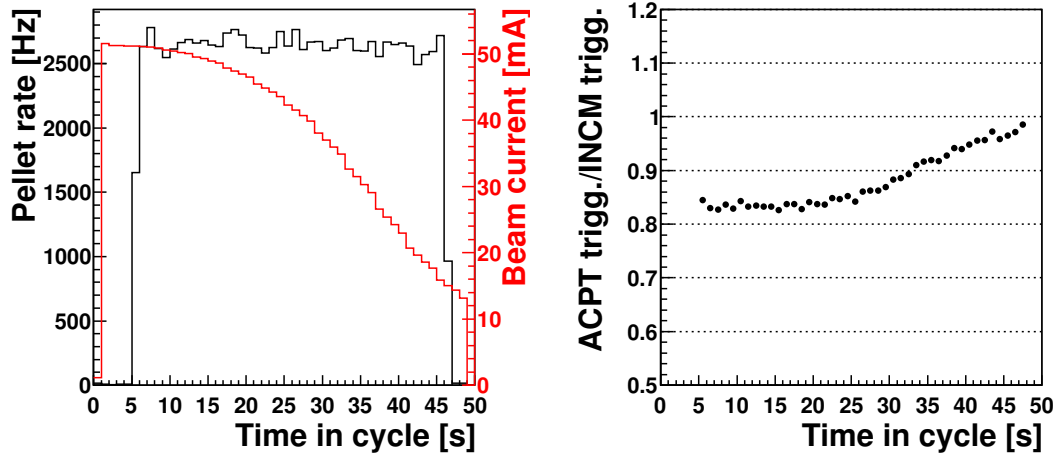
FIGURE 3.14: **Left**: Pellet rate (black) and the beam intensity (red) during one beam cycle. **Right**: The ratio of incoming to accepted triggers as a function of the time during one beam cycle.

The beamtime was planned for 65 days (9 weeks) with one week reserved for maintenance purposes. However, only 41 days (989 hours) of measurement could be used for the analysis purposes, which gives 71% of time originally dedicated to data collection. The given times were calculated without subtracting the time at the beginning and the end of the cycle when the DAQ system was switched off (see Tab. 3.1).

One reason for the significantly reduced effective beam time was an initial problem with the deuteron pellet target. The gas purifier for cleaning the deuterium gas from other residual gases had a leak, and, thus, impurities could enter the target system causing nozzle blocking by frozen gas. Several target regenerations, nozzle changes and a careful examination of the purifier took almost the first two weeks of the beamtime. First stable run conditions were achieved on 28.02.2014.

Another problem that occurred during the beamtime was caused by a dropping gain of the photomultipliers connected to FWC and FVH. It was most probably caused by a degeneration of the photomultipliers which were working for a long time with high particle rates. With dropping gain, the effective trigger thresholds were rising. Therefore, the thresholds had to be adjusted several times during the beamtime. However, as the online monitoring spectra did not show the position dependence of the detector response, for some elements and ranges of scattering angles, events from the calibration reaction $dd \rightarrow {}^3\text{He}n$ dropped below the trigger threshold (see next chapter).

In addition to the adjustment of the trigger thresholds, in the middle of the run, the high voltages of FWC and FVH were increased to achieve a higher and a more uniform gain. This divided the beamtime in two major parts. The overall gain drop was

between 5-25% for different FWC and FVH elements for every part of the beamtime. For a detailed description of these effects on the detector calibration see Sec. 4.3.1 and Sec. 4.3.2.

The rest of detector components were operating smoothly. In Tab. 3.2 a summary of the whole beamtime is given.

TABLE 3.2: Main properties of the beamtime.

Beam momentum	$1.2\,\text{GeV}/c$
Beam kinetic energy	$0.350\,\text{GeV}$
Deuterons in flat top	$1.9 - 2.5 \cdot 10^{10}$
Cycle length	$50\,\text{s}$
Pellet rate	$1500 - 11000\,\text{Hz}$
Run numbers	$41715 - 44960$
Run numbers for part 1	$41785 - 42949$ (1164 runs)
Run numbers for part 2	$42973 - 44958$ (1985 runs)
Effective time of measurement	41 days (989 hours)
Integrated luminosity	$(35.4 \pm 3.6(\text{norm.}) \pm 0.9(\text{syst.}))\,\text{pb}^{-1}$

Chapter 4

Data Analysis and Simulations

The goal of the first step of the data analysis is to reconstruct straight tracks of particles in the Forward Detector together with their kinetic energy and to obtain neutral pion candidates in the Central Detector. This information is essential for the next step of the analysis, namely to extract the signal reaction candidates (Chapter 5), and to determine the integrated luminosity (Chapter 6).

First, a calibration of the detector has to be performed. This step is largely based on Monte Carlo simulations. It is also crucial that the simulated detector response matches precisely the data.

In this chapter, the analysis software is described in Sec. 4.1. The track reconstruction procedure for particles in the Forward and Central Detector is presented in Sec. 4.2. The detector calibration is discussed in Sec. 4.3 together with the obtained resolutions of the kinematic observables. The efficiency of the Forward Proportional Chamber is described in Sec. 4.4. The chapter is closed with Sec. 4.5, where the matching of the simulated detector response to the data is discussed.

4.1   Analysis Software

4.1.1   RootSorter

The analysis, both for data and simulations, is performed using the RootSorter framework [97]. It is based on ROOT [98] and uses object-oriented programming techniques to allow modular software development and easy adaptation to individual needs.

In the first step of the event reconstruction, the data are stored in so-called banks, which holds the time and energy information from each single detector element. Every sub-detector is stored in a dedicated bank. The hit information for the experimental data is stored in a structure called `HitBankRaw`, from which it is copied to the `HitBank` after calibration. The simulation output is stored in `HitBankMC`. In order to match the Monte Carlo sample with the real experimental data, the simulated data are smeared to reproduce the experimental resolution and also copied to the `HitBank`. Therefore, after this step, simulated and experimental data are processed identically during the next steps of the analysis.

4.1.2   WASA Monte Carlo

The detector simulation is done using the WASA Monte Carlo (WMC) software which is based on GEANT3 (Geometry And Tracking) [99]. The geometry and the material types of the WASA detector setup are implemented, and the propagation of particles going through the detector is simulated. Any interactions with active and passive detector components — like energy losses, multiple scattering, secondary particle decays, and photon conversion — are included. Light propagation in the scintillators, electronic noise, the response of the photomultipliers, and the drift of the electrons in the straw tube detectors are not simulated. The match between the simulations and the detector response is obtained by an additional smearing of the simulated observables. The parameters used for smearing are defined and applied during analysis. The smearing procedure is described in Sec. 4.5.

The WMC software can process particle four-vectors from external or internal event generators. For simulating the signal reaction $dd \rightarrow {}^4\mathrm{He}\pi^0$ and the main sources of background, external generators have been used. The internal generator, which generates a chosen type of single particles in a defined kinetic energy, azimuthal and polar angular range, has been used for the purpose of error parametrization and kinetic energy reconstruction. The WMC output is similar to the experimental data format, and is also processed by the same analysis software used for experimental data.

4.1.3   Event Generator

The PLUTO software package is used as an external event generator. This software, originally designed for the HADES experiment [100] at GSI, was developed for simulations of hadronic and heavy ion interactions [101]. Later it was adapted to other reaction channels. The PLUTO generator uses the ROOT [98] environment and it generates energy-momentum four vectors for all intermediate and final particles for a defined reaction. In general, a phase-space distribution is generated using the `TGenPhaseSpace` class [102], but in addition several different basic reactions with inhomogeneous and anisotropic angular distributions can be provided. More complicated models may be implemented by the user, too.

For analysis and detector calibration, Monte Carlo samples of various hadronic reactions were needed. The $dd \rightarrow {}^3\mathrm{He}n\pi^0$ generator is based on a model obtained in the previous WASA experiment [64]. This model contains two different contributions added incoherently, namely the quasi-free reaction $d(pn_{\mathrm{spec}}) \rightarrow {}^3\mathrm{He}\pi^0 n_{\mathrm{spec}}$ and a partial wave expansion for the three-body reaction limited to at most one p-wave in the final state. In the quasi-free contribution, only the proton from one of the deuterons participates in the reaction. The neutron is a spectator, and does not take part in the momentum transfer. It leaves the reaction region with the sum of its initial momentum and the Fermi momentum at the moment of interaction. A sketch of the quasi-free reaction mechanism is presented in Fig. 4.1.

The second contribution is the partial wave expansion of the three-body reaction. The different contributions from all partial waves and interference terms up to at most one p-wave in the final state had been obtained by a fit to data [63]. Both contributions are added such that the generated $dd \rightarrow {}^3\text{He}n\pi^0$ sample contains 40% of the quasi-free production mechanism (20% with n_sp from the target and 20% with n_sp from the beam) and 60% of the partial wave decomposition model [64].
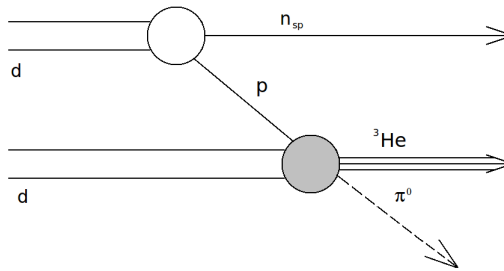
FIGURE 4.1: Sketch of the quasi-free $dd \rightarrow {}^3\text{He}n\pi^0$ reaction mechanism. Source [63].

The $dd \rightarrow {}^4\text{He}\gamma\gamma$ reaction at $p_d = 1.2\,\text{GeV}/c$ needed to describe another background contribution to the signal reaction has been simulated with an uniform 3-body phase space distribution. The $dd \rightarrow {}^4\text{He}\pi^0$ reaction has been simulated differently at different steps of the analysis: first, using a 2-body phase-space distribution, and then with the angular distribution obtained from the experiment (see Sec. 7.2).

In addition, the $dd \rightarrow {}^3\text{He}n$ reaction has been generated for calibration purposes. This generator is based on the measured total and differential cross sections presented in [103] for $dd \rightarrow {}^3\text{He}n$ for the momentum range of $1.1\,\text{GeV}/c - 2.5\,\text{GeV}/c$ and $dd \longrightarrow tp$ for the beam momenta range of $1.09\,\text{GeV}/c - 1.78\,\text{GeV}/c$. The differential cross section has been interpolated to a beam momentum of $p_d = 1.2\,\text{GeV}/c$ and included in the generator. For a detailed description see [63].

4.2 Track Reconstruction

In this section it is described how the individual detector hits have been combined to a particle track and how the direction of the particles has been extracted. The hits are tested against every detector threshold and time coincidences before they are processed. For the FVH hits also the readout from both sides of the bar is required.

In order to describe the direction and the kinematics of a particle in the detector, a right-handed coordinate system with the origin in the interaction point is introduced. The z-axis is defined as the beam axis, the y-axis is introduced upwards along the pellet beam tube, and the x-axis points outwards of the COSY ring in the horizontal plane. Both Cartesian (x, y, z) and spherical (r, θ, ϕ) systems of coordinates can be used, where θ is the polar (scattering) angle and ϕ is the azimuthal angle.

For charged particles registered in the Forward Detector the tracking algorithm is described in Sec. 4.2.1. For particles detected in the Central Detector the reconstruction procedure is presented in Sec. 4.2.2.

4.2.1 Forward Detector

Since the forward part of the detector setup was modified for the purpose of this experiment, a new track reconstruction procedure has been developed.

The track reconstruction is based on hits from FWC, FPC and FVH. The tracks of the outgoing particles are straight as there was no magnetic field in the Forward Detector. The algorithm has the following steps:

1. The geometrical overlap between hits in the first (FWC1) and second layer (FWC2) of the Forward Window Counter is checked. The granularity of the FWC layers is 24 elements each, but because one layer is rotated by a half of an element, the effective granularity is 48 elements covering $7.5°$ of the azimuthal angle ϕ. If overlapping elements are identified the algorithm moves the next step.

2. The geometrical overlap between the ϕ range from the FWC elements and the hits in the FVH is checked. If this requirement is fulfilled the algorithm proceeds to the next step.

3. The information from the Forward Proportional Chamber is used. It is checked if the ϕ angle extracted from FPC is consistent with the ϕ range of the saved track candidate from the FWC geometry within 2σ of the FPC ϕ resolution obtained from the Monte Carlo simulations.

4. Finally, the geometrical overlap between the FPC and the FVH is tested for track candidates that fulfilled all previous requirements. For each FVH bar the possible range of polar θ and azimuthal angle ϕ is calculated. If the θ and ϕ ranges match the values from FPC within 2σ, the track is saved as final.

The illustration of the track reconstruction procedure is presented in Fig. 4.2.

All of the reconstructed tracks are saved for further analysis. In Fig. 4.3 the distributions of the track multiplicities after each step of the algorithm are presented. The histograms are for a Monte Carlo sample of ^{4}He particles from the $dd \rightarrow {}^4\text{He}\pi^0$ reaction at $p_d = 1.2\,\text{GeV}/c$. In pink, the contribution of candidates that pass the first condition but do not hit any of the FVH elements is presented. It means that these particles are stopped in the air or other insensitive material between FWC and FVH.

The angular information is obtained from the FPC as follows. Let us name the four FPC planes as U, V, X, Y. Every one of these planes consists of 4 layers of tubes. Hits from different layers with geometrical overlap create so-called clusters. Every charged particle going through the FPC should produce, in the ideal case, four overlapping clusters: one from every plane. However, no detector is perfect. Sometimes less than
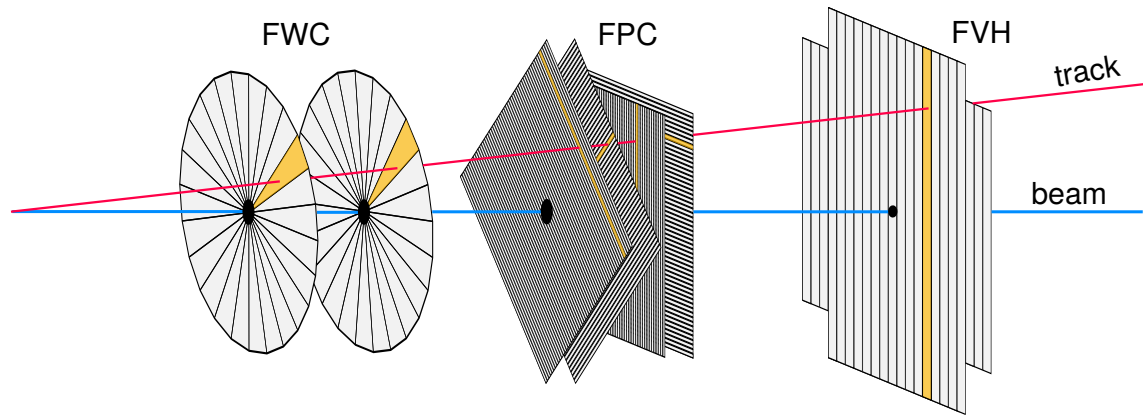
FIGURE 4.2: Ilustration of the track reconstruction procedure. The elements which define the track (red line) are marked in yellow. The detector components are not in scale. Source [104].

four matching clusters originate from one track, and sometimes there are more clusters because of electronic noise or artifacts in the cluster reconstruction. The algorithm accepts tracks with at least three matching clusters. The crossing point of all matching wires defines the azimuthal and polar angle of the track, assuming that it comes from the interaction point.

4.2.2 Central Detector

The track reconstruction in the Central Detector has been performed with the standard WASA procedure [105]. This method uses the information from the Mini Drift Chamber, the Plastic Scintillator Barrel and the Scintillating Electromagnetic Calorimeter. The aim is to identify those clusters from each of these detectors which belong to the same particle and connect them to a track.

For this analysis only the information from PSB and SEC has been used as no charged particles had to be identified. A neutral particle is defined as a cluster in SEC with no matching cluster in PSB.

In the final state of the reaction $dd \rightarrow {}^4\text{He}\pi^0$, a neutral pion decays into two photons. Therefore, one of the main trigger conditions required one or more neutral particle clusters in the Central Detector. The main background channels, described in Sec. 5, contain a π^0 or an n. However, as the efficiency of the neutron detection in the Central Detector is quite small, we did not aim at a neutron trigger. In the analysis the neutron is handled as an unmeasured particle.

When a photon enters the SEC it produces an electromagnetic shower which spreads over a group of neighboring crystals. To obtain the energy deposited by the particle, the energy from the whole cluster has to be summed up. The cluster finding routine starts from the first crystal which has an energy deposit of at least $5\,\text{MeV}$. Then, the deposited energy of each neighboring element is checked. If it is equal or larger than $2\,\text{MeV}$ and the time difference between the hit in this crystal and the hit in
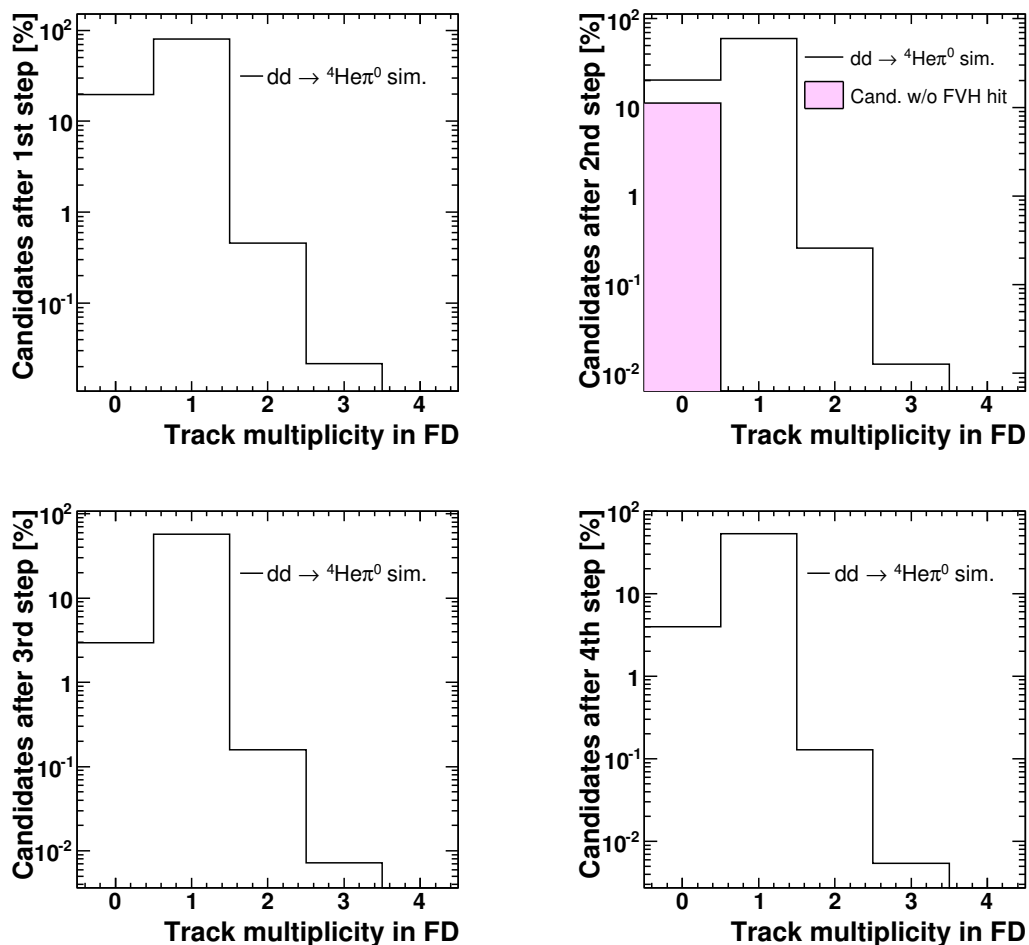
FIGURE 4.3: Distributions of the track multiplicities after every of step of the tracking algorithm described in Sec. 4.2 for the Monte Carlo sample of ^{4}He from the $dd \to {}^4$Heπ^0 reaction at $p_d = 1.2\,$GeV/c. The multiplicities are given in percentage of the number of events used to test the algorithm. In pink the contribution of the candidates that pass the first condition but do not hit any of the FVH elements is indicated.

the reference one is smaller than 20 ns, the element is added to the cluster. It is a recursive procedure: For each newly added crystal the requirements for its neighbors are checked. The sum of the deposited energy in one cluster is required to be larger than 20 MeV. This condition filters out a large amount of low-energy noise while allowing nearly every photon from a π^0 decay to be reconstructed. The time information of the whole cluster is taken from the element with the highest energy deposit. The position of the cluster $\vec{R}$ is taken as the weighted average of the positions of the front surfaces of the crystals in the cluster $\vec{r}$:

$$\vec{R} = \frac{\sum_i w_i \vec{r}_i}{\sum_i w_i} \, , \tag{4.1}$$

where the vector $\vec{r}_i$ begins in the interaction point and ends in the middle of the surface of the SEC element. The weights are defined as:

$$w_i = \max\left(0, W_0 + \ln \frac{\mathrm{d}E_i}{\sum_i \mathrm{d}E_i}\right) , \tag{4.2}$$

where $\mathrm{d}E_i$ is the deposited energy in the element i from the cluster and W_0 is a constant. For the WASA calorimeter a value of $W_0 = 5$ gives the best results for the position resolution.

The requirement for a neutral particle candidate in CD is the absence of a matching PSB cluster. If there are any hits in overlapping PSB bars, the energy deposit $\mathrm{d}E$ and the time difference $\mathrm{d}t$ is checked. If $\mathrm{d}E > 0.5\,\mathrm{MeV}$ and $\mathrm{d}t < 10\,\mathrm{ns}$, the hits are clustered. A cluster may only be formed by a single hit or by two hits. The cluster time is defined as the average of the hits. The energy of the cluster is taken from the element with the largest energy deposit.

4.3 Detector Calibration

In this part of the thesis the calibration of the Forward and Central Detectors is presented.

In the Forward Detector the energy loss of a particle in the FWC layers and the time-of-flight between FWC and FVH have to be calibrated. This means that the measured energy deposits have to be converted from QDC units to MeV and the measured times from TDC units to ns. First, the ToF calibration is performed. It is described in Sec. 4.3.1. In the next step, the energy losses are calibrated, making use of the obtained time-of-flight calibration (see Sec. 4.3.2). The parameters of both calibrations are not stable in time, mainly because of the dropping gain of the photomultipliers discussed in Sec. 3.3. This effect has to be corrected by applying run-by-run and rate-dependent corrections. This is shown at the end of the next two sections. The calibrated $\mathrm{d}E$ and ToF information is used to reconstruct the kinetic energy of outgoing ^{3}He and ^{4}He particles, which is presented in Sec. 4.3.3.

For the Central Detector, calibration is needed to obtain the energies and the direction of the photons from the π^0 decay. This procedure is presented in Sec. 4.3.4.

4.3.1 Time-of-flight in the Forward Detector

From every element of FWC and FVH the time relative to the trigger is saved in TDC units. In order to determine the time-of-flight, which is a difference between these time readouts, in physical units, the gain and the offset have to be calibrated for every detector element. The gain is defined by the binning of the TDCs — one channel corresponds to a time of $0.094\,97\,\mathrm{ns}$. The offset has to be adjusted for each channel separately. These time offsets are due to different propagation delays of the signals in

the detector, in the cables and in the electronic modules. In addition, due to different light propagation times, a correction based on the scattering angle has to be applied.

For the time-of-flight calibration, the reference reaction $dd \to {}^3\mathrm{He}n$ is used. This reaction is a two-body reaction, so for a fixed polar angle θ, the outgoing ${}^3\mathrm{He}$ has a fixed kinetic energy, and as a consequence, ToF and energy losses are well defined. The $dd \to {}^3\mathrm{He}n$ events have been selected with the main trigger conditions and the additional requirement of exactly one forward track. In Fig. 4.4 the time-of-flight versus the energy losses in the FWC1 are presented for the selected events. The prominent peak around QDC channel 4600 and time-of-flight of about 20 ns originates from ${}^3\mathrm{He}$ from $dd \to {}^3\mathrm{He}n$. From Monte Carlo simulations we know the ToF of ${}^3\mathrm{He}$ from this reaction between FWC and FVH.
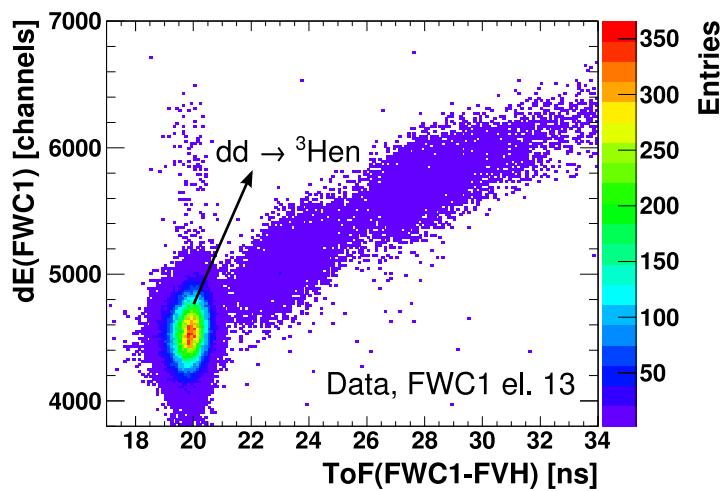
FIGURE 4.4: Time-of-flight versus energy losses in the FWC1 for the selected $dd \to {}^3\mathrm{He}n$ events. The prominent peak around QDC channel 4600 and time-of-flight of about 20 ns originates from ${}^3\mathrm{He}$ from $dd \to {}^3\mathrm{He}n$. The plot is made for element 13 of FWC1 and the angular range of $3° - 6°$.

The calibration is a multi-step procedure. In the first step, the relative offsets between FWC1 and FWC2 elements are adjusted. Then, an absolute ToF calibration is determined as a function of a Forward Veto Hodoscope element. In the following step, the θ dependence of the calibration is corrected. Finally, the stability of the calibration is checked with respect to running time, rate and run number. All steps are described below.

One of the difficulties of the time-of-flight calibration is caused by the different geometry of the FWC and the FVH. The first detector consists of wedge shaped elements, while the second one is build of vertical bars. Therefore, for different ranges of the polar angle the configuration of the overlapping FWC and FVH elements changes. In addition, not all of the FVH elements are covered by every angular bin. In the

calibration, all possible combinations of overlapping elements are used to obtain the offset corrections.

Adjustment of the FWC Offsets

In order to fix the relative offsets between the FWC1 and FWC2 elements, the ^{3}He from the $dd \rightarrow {}^3\mathrm{He}n$ reaction in a very small θ interval between $5°$ and $6°$ has been used. This was done to have a precisely defined ToF, since the first FWC layer is tilted with respect to the second one and the distance between the layers changes with θ. The relative offsets from cables and electronics do not depend on the scattering angle. In a later step, a precise θ-dependent correction includes, e.g., also effects from light propagation.

The ToF between FWC1 and FWC2 is measured for each pair of overlapping elements. In the left panel of Fig. 4.5 one can see that the measured time difference varies for every element combination. The correction for every FWC1 and FWC2 element can be calculated using the following set of 48 equations:

$$
\begin{cases}
\mathrm{ToF}^{1,1} + \delta^1_{\mathrm{FWC1}} + \delta^1_{\mathrm{FWC2}} = 0 \\
\mathrm{ToF}^{1,2} + \delta^1_{\mathrm{FWC1}} + \delta^2_{\mathrm{FWC2}} = 0 \\
\mathrm{ToF}^{2,2} + \delta^2_{\mathrm{FWC1}} + \delta^2_{\mathrm{FWC2}} = 0 \\
\ldots \\
\mathrm{ToF}^{24,24} + \delta^{24}_{\mathrm{FWC1}} + \delta^{24}_{\mathrm{FWC2}} = 0 \\
\mathrm{ToF}^{24,1} + \delta^{24}_{\mathrm{FWC1}} + \delta^1_{\mathrm{FWC2}} = 0
\end{cases}
, \tag{4.3}
$$

where $\mathrm{ToF}^{i,j}$ is the time-of-flight between element i from FWC1 layer and element j from FWC2 layer, δ^i_{FWC1} is the correction one has to apply to element i of FWC1 and δ^j_{FWC2} is the correction one has to apply to element j of FWC2. The values for $\mathrm{ToF}^{i,j}$ are obtained from a Gaussian fit of the ToF peaks. Since in this step, only the relative adjustment is done, the sum of time-of-flight and the correction terms is equal to an arbitrary value taken as zero: $\mathrm{ToF}^{i,j} + \delta^i_{\mathrm{FWC1}} + \delta^j_{\mathrm{FWC2}} = 0$. This equation is solved using an overall χ^2 fit. The result is applied to the measured time information and presented in Fig. 4.5.

Adjustment of the FVH Offsets

In this step the relative offsets of the FVH elements are adjusted as well as a first iteration of the absolute ToF calibration is performed. The ^{3}He time-of-flight between FWC1 and FVH as well as FWC2 and FVH is obtained from simulations for six polar angular bins. The same is done for data for every element of the FVH. Since the time-of-flight changes with θ — for larger polar angles it is longer — $3°$ wide bins have been used to have well defined ToF.

First, the time-of-flight between FWC1 and FVH for ^{3}He from $dd \rightarrow {}^3\mathrm{He}n$ has been fitted with a Gaussian function. For every angular bin the difference between the ToF
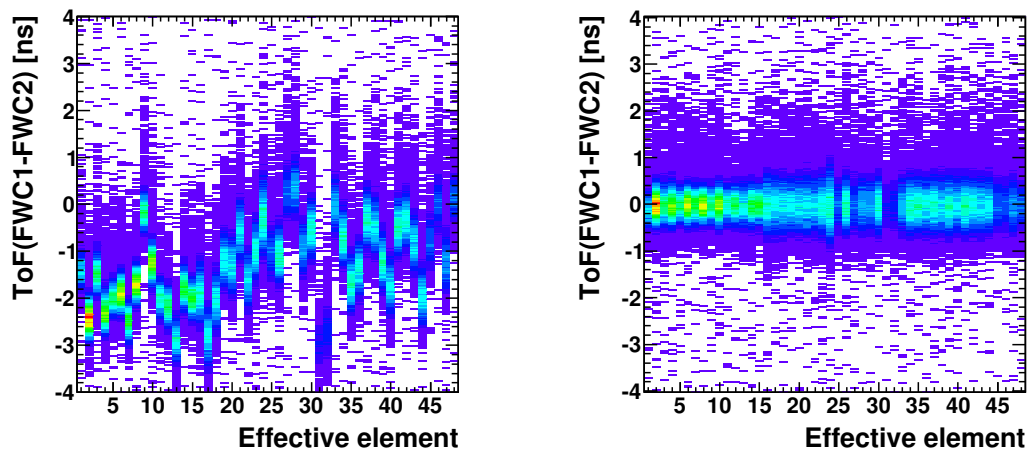
FIGURE 4.5: Time-of-flight between every pair of the overlapping elements of FWC1 and FWC2 (48 effective elements) for ^{3}He from $dd \rightarrow$ ^{3}Hen in the angular range of $5° - 6°$. The right plot shows the status after and the left one before the adjustment.

peak positions from the fit for data and Monte Carlo simulation have been obtained. Since the offsets calculated for one FVH element should be the same independently on the angular bin, finally the average of the obtained values has been used. Therefore, for each FVH element one offset has been calculated. In this way also the absolute calibration of the time-of-flight between FWC1 and FVH has been performed.

Having the relative offsets for the FVH and FWC elements adjusted, only one general correction has to be applied for the absolute calibration of the time-of-flight between FWC2 and FVH. It has been determined as an average from the differences between the ToF peak position from data and simulation for all FVH elements and θ angles. In Fig. 4.6 the ^{3}He time-of-flight between FWC1 and FVH is presented before (left panel) and after (right panel) the adjustment procedure. The plot refers to the angular range of $6° - 9°$, which is covered by the FHV elements 6 through 17.

Correction for the Polar Angle

After the relative offsets of the FVH and FWC elements have been adjusted, the next step of the absolute calibration is performed. The difference between the time of impact and the detector response depends of the distance of the hit from the photomultiplier. Therefore, the difference between the calibrated ToF and the one obtained from the simulation is checked for every FWC1 and FWC2 element for eighteen θ bins, $1°$ wide (see Fig. 4.7). For every element of the FWC a bin-wise θ-dependent correction is calculated. A parabolic interpolation between the bins is applied to avoid discontinuities at the bin edges.

The impact of the calibration steps is illustrated in Fig. 4.8, where the ToF of ^{3}He from $dd \rightarrow$ ^{3}Hen is presented for three stages: after adjusting the relative FWC offsets,
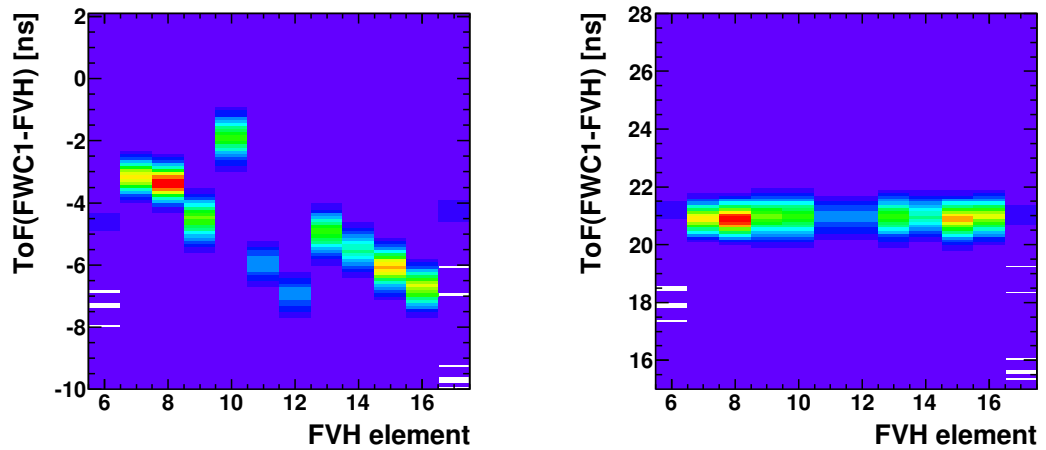
FIGURE 4.6: Time-of-flight between FWC1 and FVH before (left panel) and after (right panel) the adjustment of the FVH offsets. The plot is made for ^{3}He from $dd \to {}^3$Hen in the angular range of $6° - 9°$.
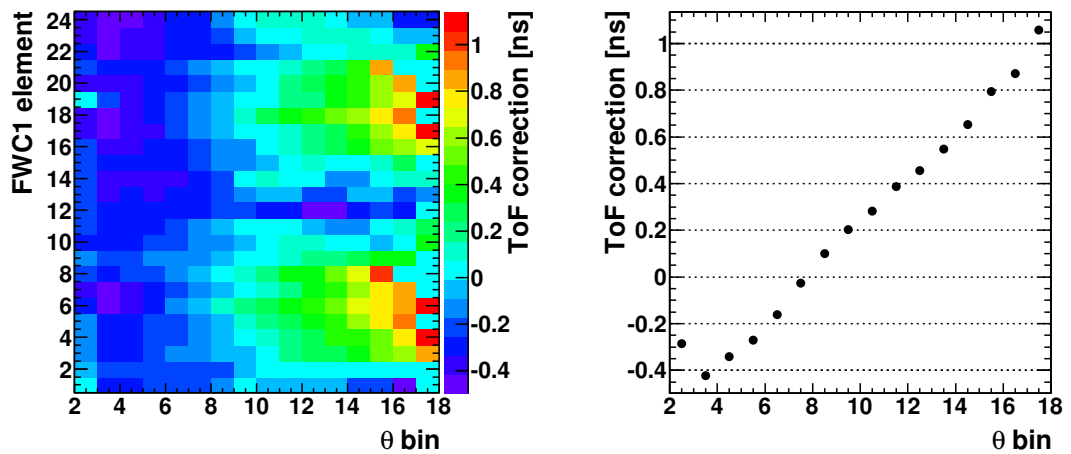
FIGURE 4.7: Correction to the ToF calibration depending on the polar angle. **Left**: The value of the ToF(FWC1-FVH) correction for every $1°$ polar angle bin and element of FWC1. **Right**: The projection for the 6th FWC element. The actual correction for the particular polar angle is calculated with parabolic interpolation between the points.

after adjusting the relative FVH offsets and the first iteration of the absolute calibration, and after the angular-dependent correction as a function of the FWC element. The plot shows one example combination: the 1st element of FWC1 and the 9th element of FVH in the angular range of $6° - 9°$. The value obtained from simulation is presented as a green line.
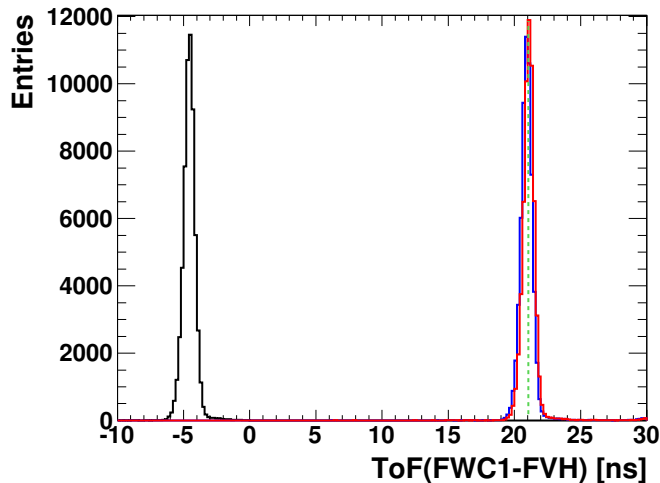
FIGURE 4.8: Time-of-flight of ^{3}He from the $dd \rightarrow {}^3$Hen reaction between FWC1 and FVH for three stages of the calibration: after adjusting the relative FWC offsets (black), after adjusting the relative FVH offsets and the first iteration of the absolute calibration (blue), and after the angular-dependent correction as a function of the FWC element (red). The plot shows one example combination: the 1st element of FWC1 and the 9th element of FVH in the angular range of $6° - 9°$. The value obtained from simulation is presented as a green line.

Rate and Run-Dependent Corrections

When checking the stability of the calibration as a function of time, a significant rate dependence has been observed. High rates have an impact on the scintillators, the photomultiplier responses and the readout electronics. Therefore, for every element of FWC and FVH a count-rate-dependent correction has been introduced. Fig. 4.9 shows the ToF(FWC1-FVH) versus count-rate of particles for element 7 of FVH, element 23 of FWC and the angular bin $6° - 9°$. The count-rate is taken for the minimum bias trigger (No. 17), which was set for elastic and quasi-elastic scattering events requiring one hit in the forward end cap of the PSB and one hit in the central barrel of the PSB. The fitted dependence is marked with a red line. The ToF peak position of ^{3}He from the $dd \rightarrow {}^3$Hen reaction is also presented as a function of the run number before and after the rate-dependent correction for the same combination of elements. As one can see, the rate correction makes the calibration more stable. Nevertheless, a remaining run-wise dependence is still visible, thus, an additional time shift depending on the run number, had to be applied.

For some combinations of the FWC and FVH elements for particular angular bins the run-wise correction is not possible because of a lost $dd \rightarrow {}^3$Hen peak caused by the dropping gain in the 1st part of the beamtime. For the 2nd part of the beamtime a linear run-wise dependence is observed, while for the 1st one it is more random. Therefore, the correction is determined only for the 2nd part of the dataset in the following way.
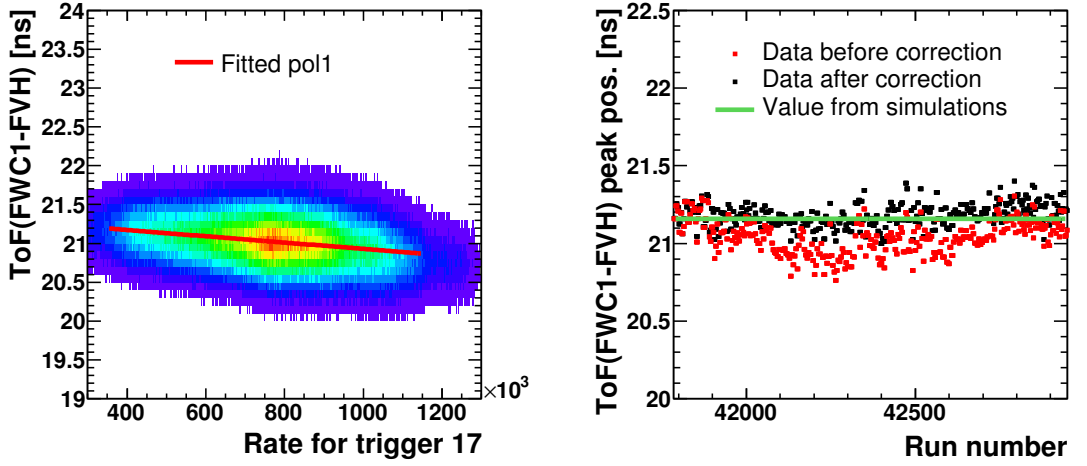
FIGURE 4.9: Rate-dependence of the ToF calibration. **Left**: Time-of-flight of ^{3}He from the $dd \to {}^3$Hen reaction between FWC1 and FVH as a function of the count-rate of the minimum bias trigger for the element 7 of FVH, the element 23 of FWC and the angular range of $6° - 9°$. The line shows the fitted correction function. **Right**: Position of the time-of-flight peak as a function of the run number before (red) and after (black) rate-dependent correction for the same combination of elements. The green line indicates the value obtained from Monte Carlo simulation.

The time-of-flight peak position of ^{3}He from $dd \to {}^3$Hen is plotted for every combination of the FWC element, the FVH element and the polar angle bin as a function of the run number. The dependence is fitted with a linear function. In order to determine one correction for every element of FWC and FVH, but using the full angular information, for every possible combination of elements and angular bin the following equation is used:

$$\delta_{\text{FWC}}^i(r) + \delta_{\text{FVH}}^j(r) = \delta_{\text{ToF(FWC-FVH)}}^{i,j}(\text{bin}_\theta, r), \qquad (4.4)$$

where $\delta_{\text{FWC}}^i(r)$ is the correction one has to apply to element i of FWC depending on the run number r, $\delta_{\text{FVH}}^j(r)$ is the correction one has to apply to element j of FVHa also depending on the run number r, and $\delta_{\text{ToF(FWC-FVH)}}^{i,j}(\text{bin}_\theta, r)$ is the difference between the time-of-flight from data and simulations for element i from FWC, for the element j from FVH, for the polar angle bin bin_θ, and the run number r. In total a set of 375 equations with 66 variables has been solved using an overall χ^2 fit. The result has been applied to the measured time information and presented in the right panel of Fig. 4.10.

The ToF variation can be caused by the observed gain drop, as this increases the effective height of the trigger thresholds. It is more significant for the 1st part of the beamtime, when some of the gains of photomultipliers were set quite low in comparison to the others. With low gains, walk effects get more significant. For the 2nd part of the beamtime, the photomultipliers were set to work in a higher gain range by increasing the high voltage. As a result, the overall ToF resolution is different for the
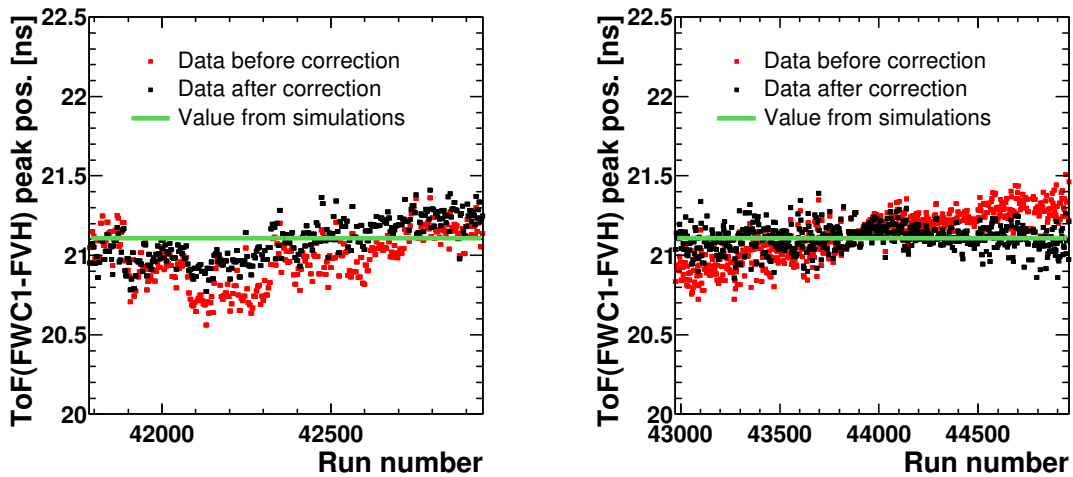
FIGURE 4.10: Run-dependence of the ToF calibration for the 1st and the 2nd part of the beamtime. **Left**: Position of the time-of-flight peak of ^{3}He from the $dd \rightarrow {}^3$Hen reaction between FWC1 and FVH as a function of the run number before (red) and after (black) the rate-dependent correction for the 1st part of the beamtime. **Right**: Dependence between the ToF peak position and the run number before (red) and after (black) the rate- and run-dependent correction for the 2nd part of the beamtime. Both pictures are done for the same combination of the detector elements: element 10 of FVH, element 19 of FWC1 and the angular range of $6° - 9°$. The green line indicates the value obtained from Monte Carlo simulation.
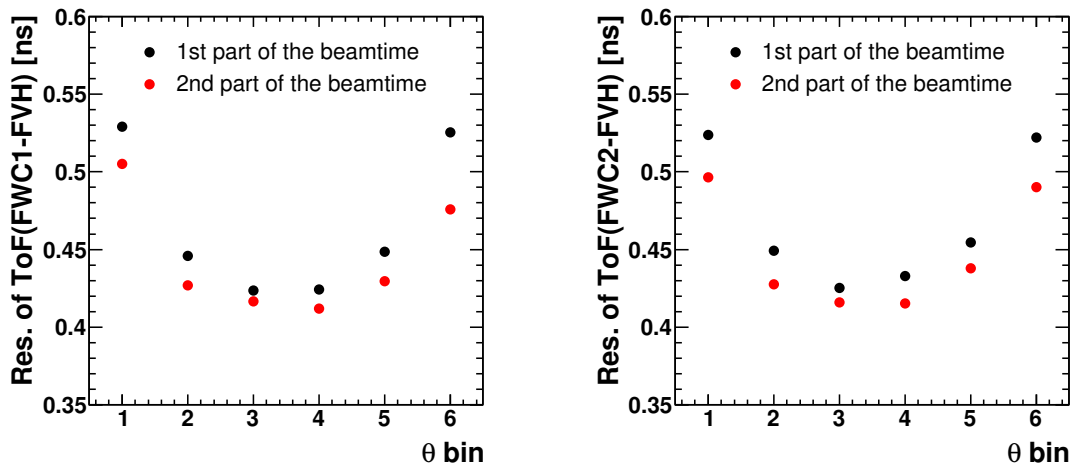
FIGURE 4.11: **Left**: Resolution of the time-of-flight between FWC1 and FVH as a function of the polar angle bin. **Right**: Resolution of the time-of-flight between FWC2 and FVH as a function of the polar angle bin. The resolutions for 1st part of the beamtime are presented in black, for the 2nd one, in red. One angular bin is $3°$ wide.

different parts of the beamtime. Therefore, the whole data analysis was performed for both parts separately.

The ToF resolution for the 1st and the 2nd part of the beamtime, as a function of the polar angle is presented in Fig. 4.11. The resolution is defined as one standard deviation of the fitted Gaussian function to the ToF peak from the $dd \rightarrow {}^3\text{He}n$ reaction for all runs from the corresponding part of the beamtime. One can see that the resolutions are similar, but slightly smaller for the 2nd part of the beamtime.

4.3.2 Energy Loss in the Forward Window Counters

For the energy loss calibration, only the gain has to be adjusted. The offset correction is done by an automatic pedestal subtraction, performed by the FPGA units in the QDCs. Because of the dropping gains, a run-dependent correction has to be applied also for the energy loss calibration. As for the time-of-flight, this is done separately for the 1st and the 2nd part of the beamtime.

Determination of the Calibration Function

The energy loss calibration is based on the ToF calibration. For every FWC element, the dependence between time-of-flight and energy loss, $dE[\text{GeV}] = f(\text{ToF[ns]})$, is obtained for a simulated sample of ${}^3\text{He}$ with kinetic energies of $0 < E_{kin} < 0.5$ GeV and polar angles of $0° < \theta < 18°$. It is fitted with a 3rd order polynomial for six θ bins. As an example, one angular bin, $6° - 9°$, is presented in Fig. 4.12. For data the ToF can now be recalculated to the expected energy losses in physical units (GeV) using the function $dE[\text{GeV}] = f(\text{ToF[ns]})$ obtained before. As a result, the energy loss in QCD channels versus the energy loss in GeV can be plotted for data. From this, a dE calibration function $dE[\text{GeV}] = f(dE[\text{channel}])$ is deduced.

This has to be done as a function of the scattering angle, since the larger the angle is, the longer is the path length of a particle in the detector layer. For every FWC element and θ bin, the correlations between dE in QDC channels and dE in physical units are fitted with a linear function, using a two-dimensional χ^2 fit procedure based on the `TMinuit` [106] ROOT class. An example fit is presented in the right panel of Fig. 4.12. A linear interpolation between the θ bins has been applied to avoid discontinuities at the bin edges. In the first step, the calibration function for every FWC element is determined using the first runs from every part of the beamtime. This is the basis for the following run-dependent correction.

Run-dependent Correction

The energy loss calibration is also affected by the observed drop in gain. The effect is shown in the left panel of Fig. 4.13. A plot of ToF between FWC1 and FVH versus the energy loss in the FWC1 is presented for a run from the end of the 2nd part of the beamtime (run 44900) for the angular bin $3° - 6°$. Furthermore, the function describing the ToF(dE) dependence for the initial calibration runs is shown. One can see a
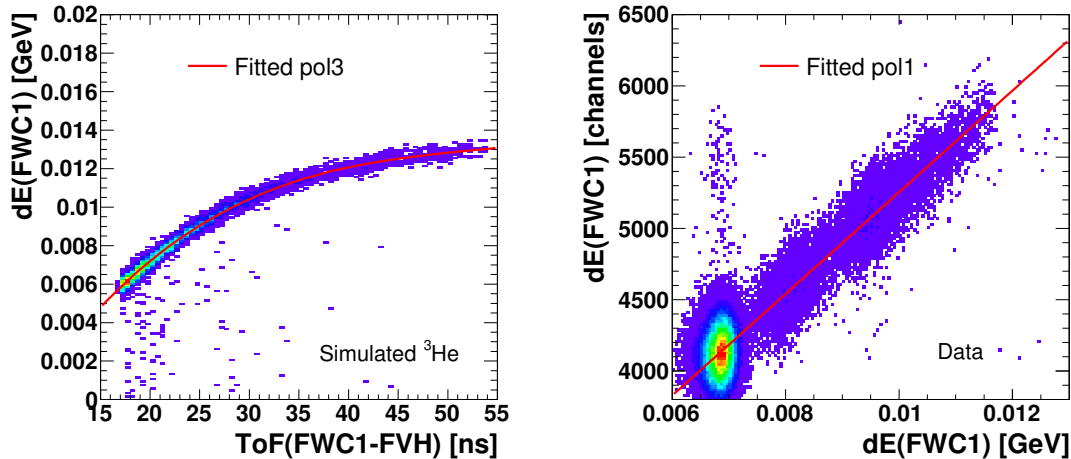
FIGURE 4.12: **Left**: Dependence between the time-of-flight and the energy loss obtained from simulated ^{3}He in the Forward Detector for the angular bin $6° - 9°$. The curve shows the fitted 3rd order polynomial. **Right**: Dependence between energy loss in QCD channels and GeV for the 2nd element of the FWC1 and the angular bin $6° - 9°$ for data. The linear calibration function fitted to this spectrum is marked in red.

significant displacement in the data from the last runs with respect to the data from the first runs.

In order to correct this effect, for every run the ratio between the obtained energy loss, and the reference energy loss that a particle should have based on its ToF (calculated from dE[GeV] = f(ToF[ns])) is checked. For a stable calibration, this ratio should have a Gaussian distribution and should be centered at one. While this is true for the first 15 runs from each part of the beamtime, used to determine the calibration functions, for subsequent runs, the Gaussian distribution is shifted towards numbers smaller than one. In the right panel of Fig. 4.13 this ratio is presented for a run from the beginning and end of the 2nd part of the beamtime. A change of about 10% is visible. The plot is done for the angular bin $3° - 6°$ for element 20 of FWC1. Tracking the position of the ratio for every run allows to determine a correction factor. In Fig. 4.14 this correction factor is shown for element 20 of FWC1 and element 15 of FWC1, for which the gain drop is the most significant. The correction factors studied for all FWC elements are between $1/0.9 - 1/0.75$ for the last runs of the beamtime part. For applying this correction, a 3rd order polynomial has been fitted to the histograms.

Using the final calibration, the relative resolution of the energy loss is determined as a function of the polar angle. It is presented in Fig. 4.15 for both parts of the beamtime. The resolution defined as one standard deviation of the Gaussian fit is about $7\% - 9\%$.
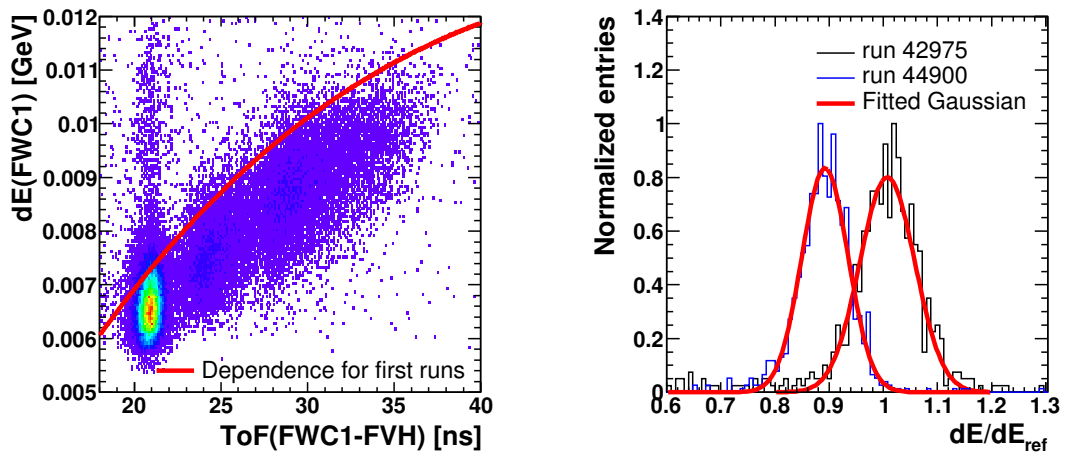
FIGURE 4.13: **Left**: ToF between FWC1 and FVH versus the energy loss in the FWC1 for a run from the end of the 2nd part of the beamtime (run 44900) for the angular renage of $3° − 6°$. The function describing the ToF(dE) dependence for the initial calibration runs is shown in red. **Right**: Ratio between the obtained energy losses, and the reference energy losses that a particle should have based on its ToF (calculated from $dE[\text{GeV}] = f(\text{ToF[ns]})$) for run 44900 (blue) and for run 42975 (black). From the Gaussian fit the mean value is equal to 1.007 ± 0.014 for the run 42975 and 0.892 ± 0.013 for the run 44900. The plot is made for element 20 of the FWC1 and the polar angular bin $6° − 9°$. Both plots are made for detected ^{3}He.
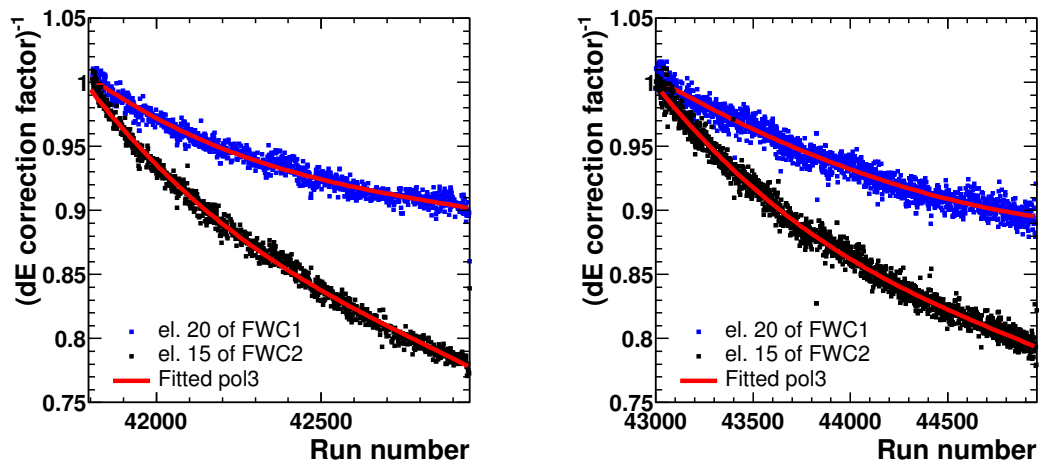
FIGURE 4.14: Run-dependent correction factor of the energy loss in the FWC for element 20 of FWC1 (blue) and element 15 of FWC1 (black), for which the gain drop is the most significant. **Left**: The correction factor for the 1st part of the beamtime. **Right**: The same for the 2nd part of the beamtime. In red the fitted 3rd order polynomial is drawn. Both plots are done for the polar angle bin $6° − 9°$.
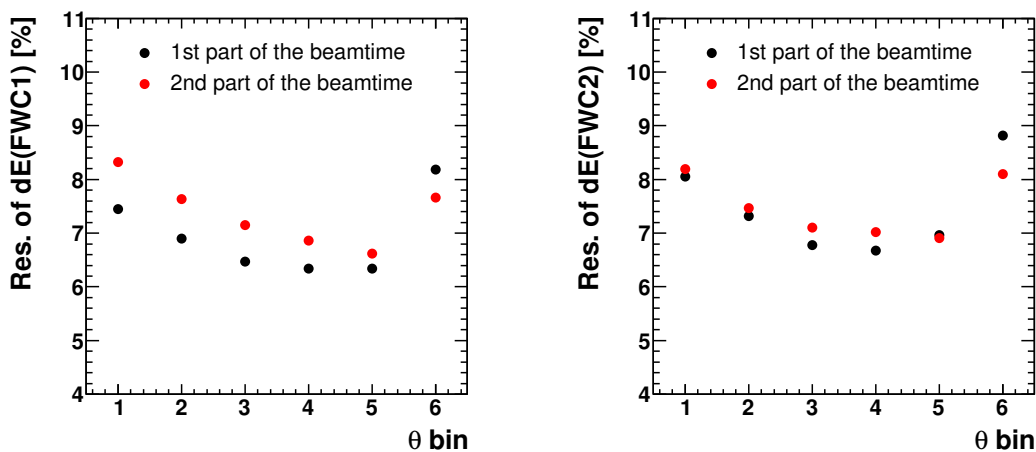
FIGURE 4.15: **Left**: Resolution of the energy loss in the FWC1 as a function of the polar angle bin. **Right**: Resolution for the FWC2 as a function of the polar angle bin. The resolutions for the 1st part of the beamtime are presented in black, for the 2nd one, in red. One angular bin is $3°$ wide.

4.3.3   Kinetic Energy Reconstruction

In this section the procedure of the kinetic energy reconstruction of the outgoing ^{3}He and ^{4}He in the Forward Detector is described. A particle passing through the detector looses its energy in every active detector layer (i.e., FWC and FVH) but also in several layers of insensitive material (i.e., exit window, detector wrapping foil, layers of FPC and air). Therefore, the kinetic energy cannot be simply calculated as the sum of the energy losses from FWC and FVH. Instead, it has to be reconstructed from the energy loss pattern using a method based on Monte Carlo simulations.

The procedure uses the correlations of energy loss in the FWC and time-of-flight versus kinetic energy, respectively, obtained from a Monte Carlo simulation. In a first step, these dependencies are parametrized with analytical functions: a 4th order polynomial for $dE(E_{kin})$, and the sum of an exponential function and a 3rd order polynomial for $ToF(E_{kin})$. This has to be done separately for ^{4}He and ^{3}He, because for the same initial kinetic energy the energy loss patterns for these particles are different. There is also an angular dependence which has to be taken into account: the larger the polar angle is, the longer the path is the particle travels through the detector, and the larger the energy losses in the FWC and time-of-flight are. Therefore, the $dE(E_{kin})$ and $ToF(E_{kin})$ parametrizations are done for different θ bins, each $3°$ wide. The simulated sample of ^{4}He and ^{3}He used for this procedure covers the kinetic energy range of the helium ejectiles from $dd \rightarrow {}^4\text{He}\pi^0$ and $dd \rightarrow {}^3\text{He}n\pi^0$ at $p_d = 1.2\,\text{GeV}/c$. In Fig. 4.16 the parametrization of the deposited energy in the FWC layers and the time-of-flight as a function of the initial kinetic energy is presented for ^{4}He. The plots show the angular range of $6° - 9°$.
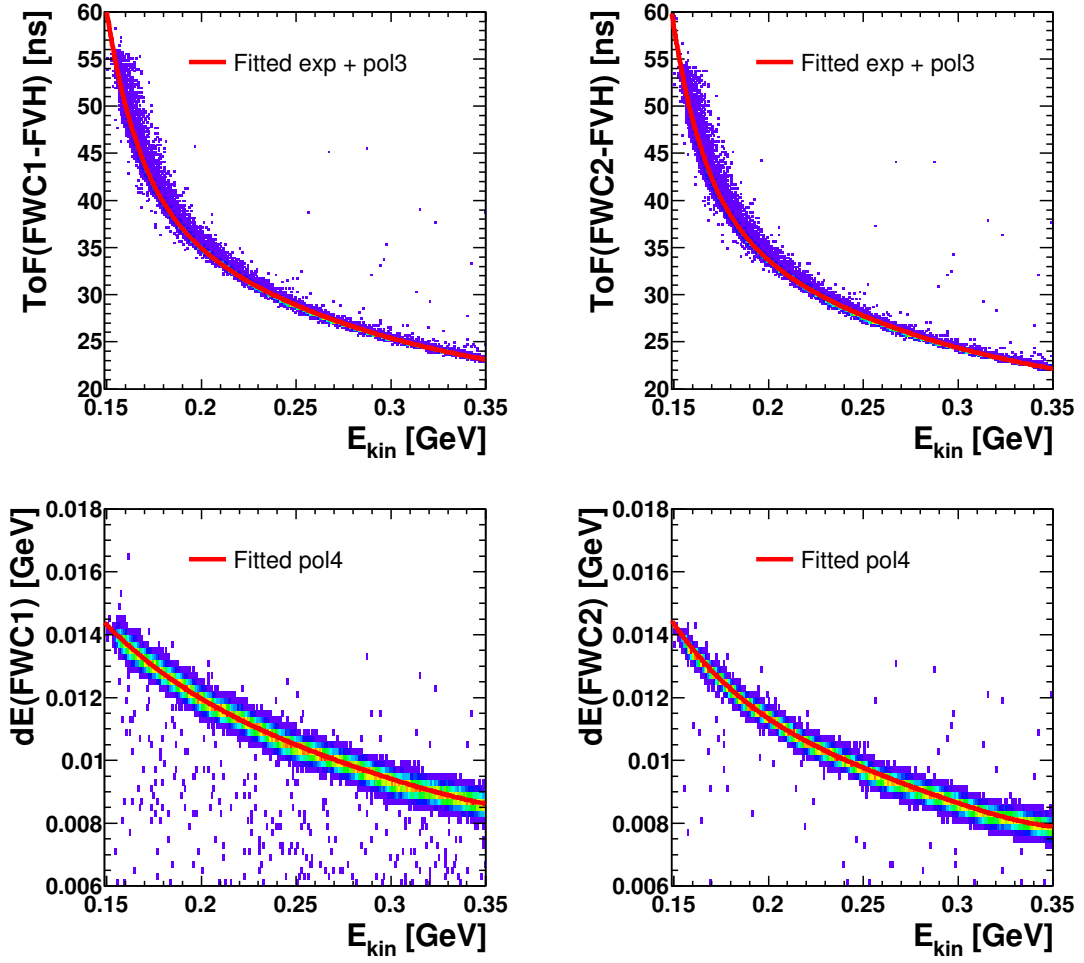
FIGURE 4.16: Parametrization of the deposited energy in the FWC layers (bottom row) and the time-of-flight (upper row) for ^{4}He as a function of the initial kinetic energy. The fitted functions are shown in red. In case of the energy loss a 4th order polynomial is fitted, in case of the time-of-flight the sum of a 3rd order polynomial and an exponential function. Plots are made for particles in the angular range of $6° - 9°$.

In order to calculate the kinetic energy, for every event a χ^2 function is defined:

$$\chi^2 = \sum_{i=1}^{n} \frac{(\mathrm{d}E_i^{meas} - \mathrm{d}E(E_{kin})_i)^2}{\sigma_i^2} + \sum_{j=1}^{m} \frac{\left(\mathrm{ToF}_j^{meas} - \mathrm{ToF}(E_{kin})_j\right)^2}{\sigma_j^2}, \qquad (4.5)$$

where n is the number of FD layers ($= 2$) and m refers to the number of time-of-flight combinations ($= 2$). The numerator in Eq. 4.5 is the square of the difference between the measured energy loss $\mathrm{d}E^{meas}$ or time-of-flight ToF^{meas}, and the expected values of $\mathrm{d}E(E_{kin})$ or $\mathrm{ToF}(E_{kin})$ from the parametrization. In the denominator the squared uncertainty of the energy deposit or time-of-flight is taken as a function of scattering angle from Fig. 4.11 and 4.15. The value of E_{kin} for which the χ^2 function has a global minimum is taken as the most probable value of the initial kinetic energy. A linear

interpolation between the angular bins is applied to avoid discontinuities between the bins. Fig. 4.17 shows the χ^2 distribution using the $dd \to {}^4\text{He}\pi^0$ and $dd \to {}^3\text{He}n\pi^0$ simulations, and a data sample which contains mostly ${}^3\text{He}$. The plots are normalized to the same height. To choose only events with a well reconstructed kinetic energy, a loose cut on a minimal χ^2 of 30 is applied later in the analysis.

In Fig. 4.18 the difference between the reconstructed E_{kin} and the true value from the Monte Carlo simulation is presented for ${}^3\text{He}$ from $dd \to {}^3\text{He}n\pi^0$ and ${}^4\text{He}$ from $dd \to {}^4\text{He}\pi^0$. The simulated d$E$ and ToF resolutions were tuned to match the experimental ones (see Sec. 4.5). From the plots, one can see that the distribution is centered at zero, with a root mean square of about 0.003 GeV, what can be taken as a error of the kinetic energy reconstruction.
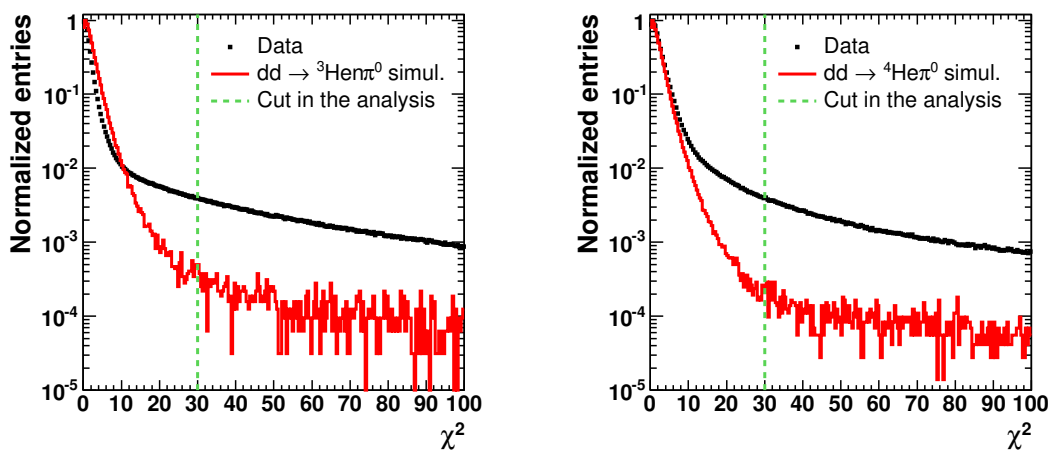
FIGURE 4.17: χ^2 distribution obtained from the E_{kin} reconstruction procedure for data (black points) and simulations (red histogram) for ${}^3\text{He}$ (**left**) and ${}^4\text{He}$ (**right**). The data set consists mostly of ${}^3\text{He}$. In green, the cut applied in the further analysis is shown.

4.3.4 Scintillator Electromagnetic Calorimeter

The Scintillator Electromagnetic Calorimeter is used to obtain the four-vectors of the photons from the π^0 decay. The SEC crystals are pre-calibrated using cosmic muons and radiative sources [91]. A calibration is done by adjusting the invariant mass of two photons to the π^0 mass, for all two-photon combinations.

To get an enhanced sample of photons from the π^0 decay, events with exactly two neutral particles in the Central Detector are selected (see Sec. 4.2.2). For every pair of photons the invariant mass $M_{\gamma\gamma}$ can be calculated having their energies E_1, E_2 and the open angle θ_{12} between their momenta vectors:

$$M_{\gamma\gamma} = \sqrt{2E_1 E_2 \left(1 - \cos\theta_{12}\right)}. \tag{4.6}$$
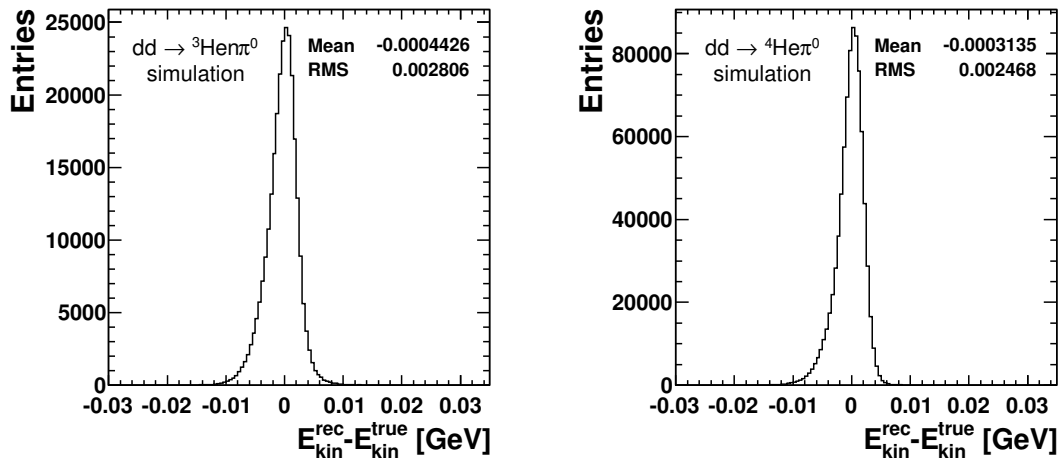
FIGURE 4.18: Difference between the reconstructed E_{kin} and the true value from the Monte Carlo simulation for ^{3}He from $dd \to {}^3\mathrm{He}n\pi^0$ (**left**) and ^{4}He from $dd \to {}^4\mathrm{He}\pi^0$ (**right**).

In the calibration procedure, this invariant mass $M_{\gamma\gamma}$ is assigned to the crystals with the largest energy deposit in each cluster. The gain for these elements is then adjusted based on the ratio between the invariant mass and the π^0 mass $m_{\pi^0} = 0.1349\,\mathrm{GeV}/c^2$. As one crystal can be combined with all other crystals, the calibration of each crystal is not independent from the others. Therefore, this procedure is repeated iteratively until the invariant mass distributions for all SEC modules are centered at the mass of π^0, and the result is stable. The parameters for the SEC calibration are taken from [107].

In the left panel of Fig. 4.19 the invariant mass of two photons is shown for about 1/3 of all runs. The green line represents the value of the π^0 mass m_{π^0}. The invariant mass as a function of the SEC element is presented in the right panel of Fig. 4.19. The red line indicates m_{π^0}. One can see that $M_{\gamma\gamma}$ is well centered at the mass of neutral pion. The SEC elements with high numbers correspond to the forward part of the Central Detector, where the background is large and — due to kinematics — the number of pions is lower.

4.4 Efficiency of the Forward Proportional Chamber

Besides the kinetic energy also the direction of a particle has to be determined. For this the Forward Proportional Chamber is used. As mentioned earlier, the individual planes are not 100% efficient. For reconstruction, only 3 out of four planes are required. However, the overall detection efficiency has to be determined and corrected for.

This has been done in the following way. The efficiency of, for example, the plane U (see Sec. 4.2.1), is a ratio of the number of reconstructed tracks with a cluster in all four planes to the number of all reconstructed tracks without requiring plane U.
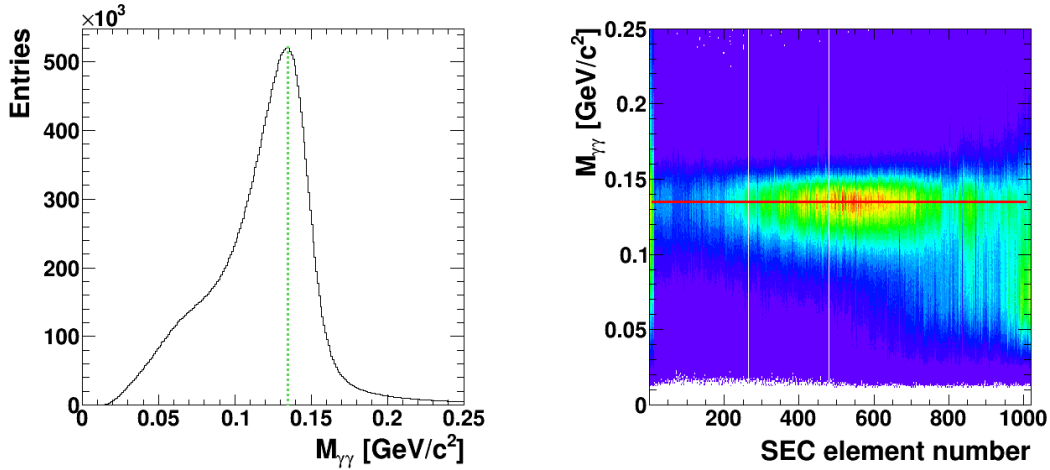
FIGURE 4.19: **Left**: Invariant mass of two photons for about 1/3 of all runs. The sample is dominated by π^0 from the $dd \to {}^3\mathrm{He}n\pi^0$ reaction. The green dashed line indicates the mass of neutral pion. **Right**: The same but as a function of the element of the Scintillator Electromagnetic Calorimeter. The SEC elements with high numbers correspond to the forward part of the Central Detector, where the background is large and — due to kinematics — the number of pions is lower. The red line indicates the mass of π^0.

The efficiencies for the other FPC planes are calculated similarly. The efficiency plots are shown in Fig. 4.20. On the x-axis the position of the cluster along the axis perpendicular to the tubes in the considered module is presented. Zero corresponds to the position at the beam pipe. One can see that for the first two planes the efficiency is about 96%, and it drops to about 90% in the last two. The dip around zero corresponds to the beam pipe.

The overall efficiency for three out of four planes is shown in Fig. 4.24 belonging to the next section as a function of the x and y coordinates of the track. The black circle corresponds to the maximum angle of the FPC acceptance. The overall efficiency within this acceptance region is about 97%.

4.5   Matching Simulations and Data

While the Monte Carlo package is able to simulate energy losses and other interactions of particles with matter, any threshold effects by the scintillator processes, the light propagation, or the readout electronics are not included. This has to be added in the analysis of the Monte Carlo output. Matching the resolutions in simulation and data is achieved by an additional smearing of the simulated observables. For the time readout and the energy loss resolutions this is discussed in Sec. 4.5.1, 4.5.2, 4.5.3. The efficiency of the FPC has also to be matched between the simulations and data. This is shown in Sec. 4.5.4. In addition, as a last adjustment, a cut on the kinetic energy distribution of ${}^3\mathrm{He}$ and ${}^4\mathrm{He}$ is introduced for data (see Sec. 4.5.5).
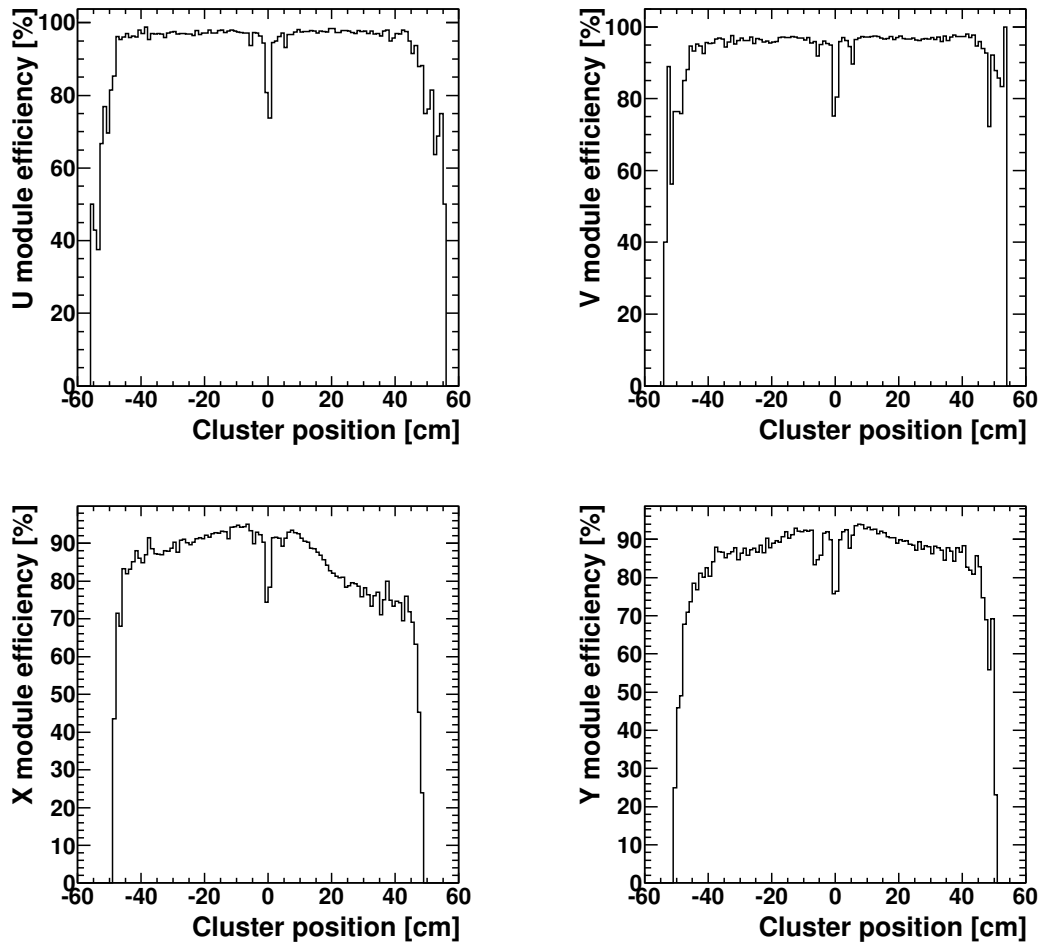
FIGURE 4.20: Efficiency of the FPC planes used for the tracking in the Forward Detector as a function of the position of the cluster along the axis perpendicular to the straw tubes. Plots are made using detected ^{3}He particles.

A mismatch between the simulated and experimental energy resolution of dE and ToF can affect the selection of ^{3}He and ^{4}He candidates and, as a result, the acceptance of the simulated reactions. In addition, for the kinematic fit described in Sec. 5.2, a precise parameterization of the resolutions is essential, which can be obtained only from simulations.

4.5.1 Resolution of the Time Readout

The resolution of the simulated time readout from FWC and FVH is adjusted on the hit level. The time readout from every hit in the layer is smeared by adding a value randomly taken from a Gaussian distribution with the mean equal to 0 and the standard deviation which has to be tuned. To obtain the width of the Gaussian distributions, a

sample of ^{3}He from the $dd \to {}^3\text{He}n$ reaction has been used. From data, one can obtain the width of three different time-of-flight distributions: between FWC1 and FVH, between FWC2 and FVH, and between FWC1 and FWC2. These resolutions are determined as one standard deviation of the Gaussian function fitted to the ^{3}He ToF peak from data. The ToF resolution σ^2_{ToF} is linked to the resolution of the individual time readout σ^2_t from every separate layer:

$$\begin{cases} \sigma^2_{\text{ToF(FWC1-FWC2)}} = \sigma^2_{t(\text{FWC1})} + \sigma^2_{t(\text{FWC2})} \\ \sigma^2_{\text{ToF(FWC1-FVH)}} = \sigma^2_{t(\text{FWC1})} + \sigma^2_{t(\text{FVH})} \\ \sigma^2_{\text{ToF(FWC2-FVH)}} = \sigma^2_{t(\text{FWC2})} + \sigma^2_{t(\text{FVH})} \end{cases} . \tag{4.7}$$

From this set of equations the individual resolution for every layer can be obtained. As the time readout depends on the polar angle — due to the different time a particle travels through the detector, different light collection efficiencies, and different electronics' response — the smearing procedure has to be angular dependent using a linear interpolation between certain angular bins. In the left panel of Fig. 4.21 the values obtained from Eq. 4.7 are presented. The width of the Gaussian smearing function is obtained as the square root of the difference of the squared time resolution from data and simulations. The comparison between the ToF(FWC1-FVH) resolution for data and for simulation after applying the smearing is shown in the right panel of Fig. 4.21. The agreement for the ToF(FWC2-FVH) resolution is similar.

4.5.2   Energy Losses in the FWC

The adjustment of the resolution of the simulated energy losses is done similarly to the ToF. The correction factor is randomly taken from a Gaussian distribution with a mean value equal to 1 and a standard deviation which has to be tuned. The relative resolution of the energy losses is determined in data and simulations using ^{3}He from the $dd \to {}^3\text{He}n$ reaction. The square root of the difference between the squared resolution of the data and the squared resolution of the simulation is taken as the width of the smearing distribution. The comparison of the resolutions in data and simulation is presented in Fig. 4.22 for FWC1 and FWC2 for the 1st part of the beamtime. For the 2nd part of the beamtime the agreement is similar. An angular dependence is also included in the smearing process.

4.5.3   Energy Losses in SEC

The simulated energy deposit of the photons in the SEC have to be smeared to describe correctly the width of the invariant mass distribution of the two photons from the π^0 decay. For this, a sample with one FD track and two CD neutral clusters matching the $dd \to {}^3\text{He}n\pi^0$ reaction hypothesis was chosen according to the selection criteria described in Sec. 5.2.
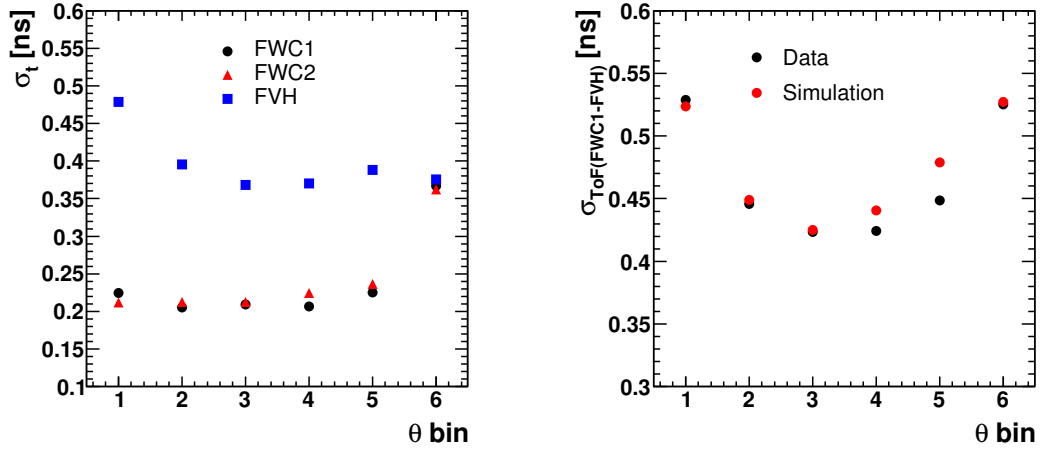
FIGURE 4.21: **Left**: Time readout resolutions for FVH (blue), FWC1 (black), and FWC2 (red) as a function of the polar angle bin for data. **Right**: Comparison of the resolution of ToF(FWC1-FVH) for data (black) and for simulation (red) after applying the smearing correction as a function of the angular bin. Plots are done for all runs from the 1st part of the beamtime using ^{3}He from the $dd \to {}^3$Hen reaction.
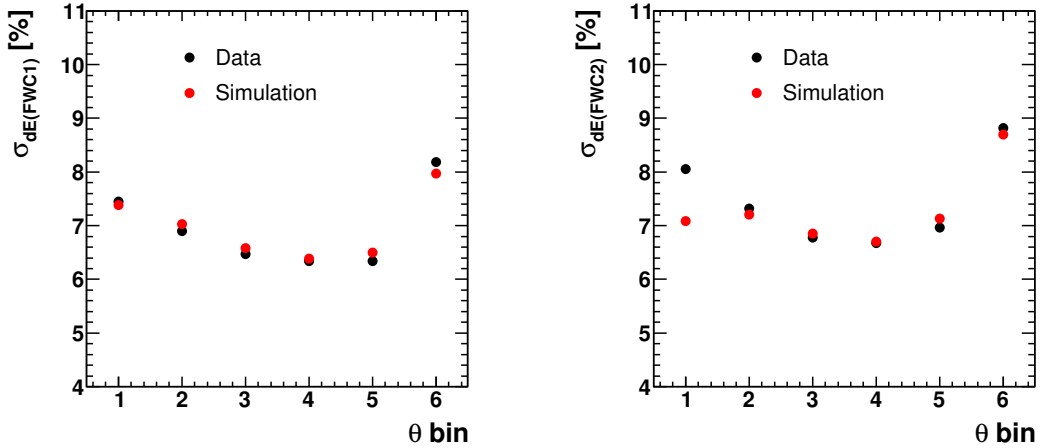
FIGURE 4.22: Comparison of the resolution of the energy losses from data (black) and simulations (red) as a function of polar angle bins. **Left**: Comparison for FWC1. **Right**: Comparison for FWC2. One angular bin is $3°$ wide. Plots are done for all runs from the 1st part of the beamtime.

In the case of the SEC, two individual Gaussian smearings are used: a constant relative smearing and an energy-dependent smearing which refers to the statistical fluctuations of the conversion of scintillation light to photoelectrons in the photomultiplier. Tunning these two contributions allows to change the response of the SEC and, thus, the width of the invariant mass spectra. In addition, a correction factor for shower losses is applied to match the position of the invariant mass peak. The result of the tuning is given in Fig. 4.23 where the invariant mass of two photons is presented for data and simulation of the $dd \to {}^3$He$n\pi^0$ reaction.
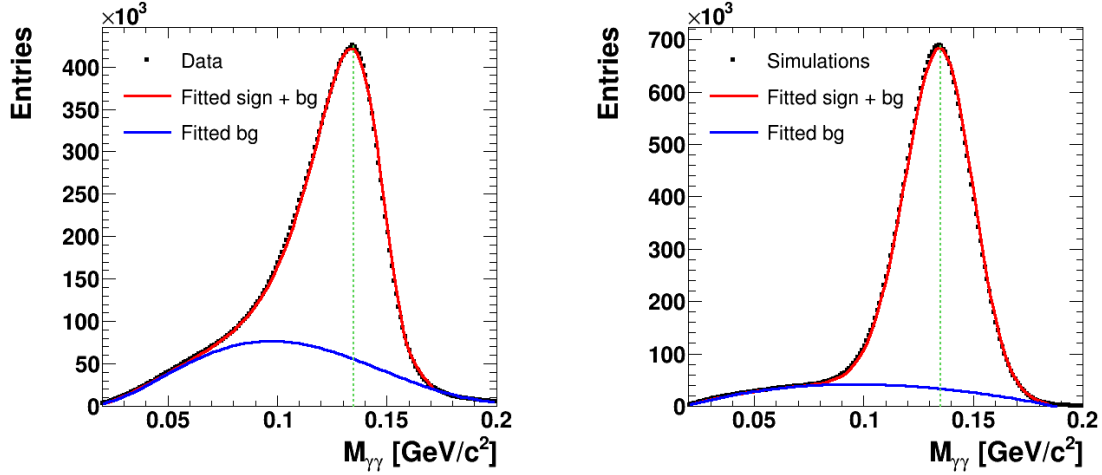
FIGURE 4.23: **Left**: Invariant mass of two photons for a sample with one FD track and two CD neutral clusters matching the $dd \to {}^3\text{He}n\pi^0$ reaction hypothesis from the kinematic fit in the best way. **Right**: Invariant mass of two photons for the $dd \to {}^3\text{He}n\pi^0$ reaction simulation. Both spectra are fitted with the sum of a Novosybirsk function and a 4th order polynomial shown in red. The background estimation is shown with a blue line. The green line indicates the mass of π^0. Plots are made for the 1st part of the beamtime.

The peak is fitted with a Novosybirsk function and a 4th order polynomial to describe the background. The Novosybirsk function has the following form:

$$f(x) = A \cdot \exp\left[-\frac{1}{2}\left(\frac{\ln q_x}{d}\right)^2 + d^2\right] , \tag{4.8}$$

where

$$q_x = 1 + \frac{x - x_0}{\sigma} \cdot \frac{\sinh(d\sqrt{\ln 4})}{\sqrt{\ln 4}} . \tag{4.9}$$

Here A is the amplitude of the signal, x_0 is the peak position, σ is FWHM/2.35 and d is the asymmetry parameter. This function takes into account the tail towards lower invariant masses resulting from the energy response of the calorimeter [108]. The obtained parameters for data and simulation are presented in Tab. 4.1. There is a good agreement for the peak position and width. However, there is a difference in the asymmetry parameters. The matching of the shape of the spectra is significantly improved after the four-vectors obtained in the kinematic fit are used and the cut on the cumulative probability distribution is applied. Using the obtained adjustment parameters, the final missing mass spectra for the $dd \to {}^4\text{He}X$ reaction (see Sec. 5.4) in the region of the π^0 peak are well described.

TABLE 4.1: Comparison of the fit parameters of $M_{\gamma\gamma}$ for data and simulation.

Parameter	Data	Simulation
1st part of the beamtime		
Peak position x_0	134.64(6) MeV	134.71(9) MeV
FWHM	35.77(2) MeV	36.18(1) MeV
Assym. param. d	$-0.249(6)$	$-0.061(2)$
2nd part of the beamtime		
Peak position x_0	134.51(6) MeV	134.45(8) MeV
FWHM	36.77(2) MeV	36.25(1) MeV
Assym. param. d	$-0.247(6)$	$-0.061(2)$

4.5.4 FPC Efficiency

In Sec. 4.2.1 the track reconstruction in the Forward Detector has been described. The algorithm requires the matching of clusters from at least three FPC planes out of four (U, V, X, Y). The efficiency of every module has been determined for data (see Fig. 4.20). However, what matters in the tracking procedure, is the overall probability for three out of four planes. In the upper row of Fig. 4.24 this probability is shown for data and simulation for the $dd \rightarrow {}^3\text{He}n\pi^0$ reaction as a function of the x and y coordinates of the track. As they differ slightly, a correction map has been introduced, dividing the probability for data by the probability for simulation. This is shown in the lower row of Fig. 4.24. The black circle corresponds to the maximum angle of the FD acceptance $\theta = 18°$. A zoomed correction map is shown in the right bottom panel to visualize better the asymmetry. The correction factor has been applied to all simulated forward going particles in the analysis.

4.5.5 Comparison of Kinetic Energy

When comparing the ToF information for the data and simulation, the data sample consists of more events with higher ToF than the simulation. Fig. 4.25 shows the ToF(FWC1-FVH) for ${}^3\text{He}$ from $dd \rightarrow {}^3\text{He}n\pi^0$ for the scattering angle between $3° - 6°$. The selection (described in Sec. 5.2) is based on a cut on the complementary cumulative probability distribution for the kinematic fit. One can see that the tail for data (black markers) extends beyond the simulation (red line). The difference may originate, for example, in a slightly too thick detector wrapping in the simulations or a mismatch in the air temperature. The effect is not big (note the logarithmic scale), however, a further cut on the kinetic energy is applied to match data and simulation. It is defined as presented in the right panel of Fig. 4.26. For comparison, the same spectrum is shown for the selected data in the right left. The time-of-flight of ${}^3\text{He}$ after applying the cut is presented in Fig. 4.25 with the blue points. The cut on the ${}^3\text{He}$ kinetic energy is applied only for the analysis of the $dd \rightarrow {}^3\text{He}n\pi^0$ reaction, i.e., the
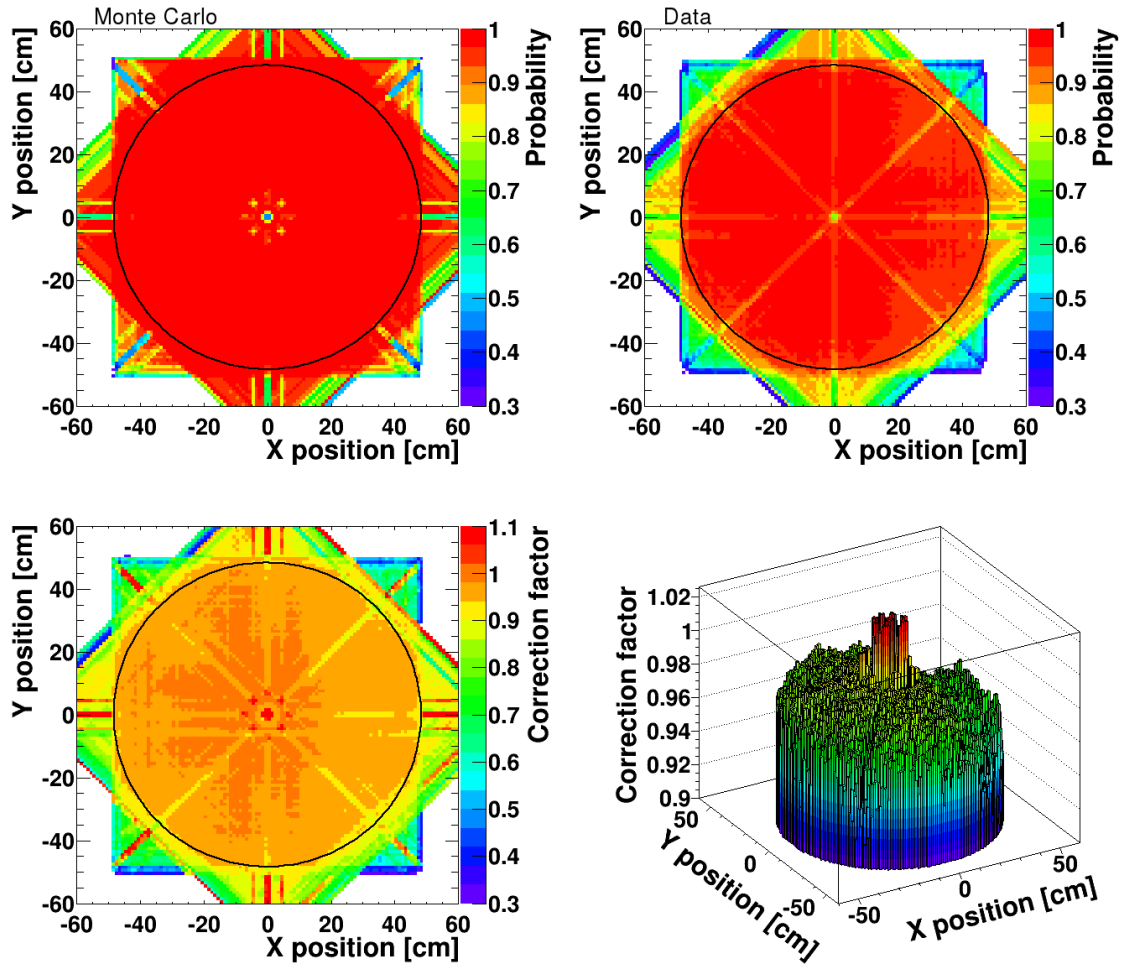
FIGURE 4.24: FPC efficiency for data and simulation. In the upper row the probability that three out of four FPC planes fired is presented for simulations and data as a function of the x and y coordinates of the track. The obtained correction factors for simulations are presented in the lower row. The black circle corresponds to the maximum angle of the FPC acceptance $\theta = 18°$. The right bottom plot is zoomed to see the asymmetry of the correction.

luminosity calculation. It is not used in the analysis optimized for the signal reaction selection and its cross section determination in order not to remove good candidates for the $dd \rightarrow {}^4\text{He}\pi^0$ events.

The cut on the ${}^4\text{He}$ kinetic energy is applied separately. This cut is defined using a simulation of the $dd \rightarrow {}^4\text{He}\pi^0$ reaction. In Fig. 4.27 one can see the distribution of E_{kin} vs θ for the simulated ${}^4\text{He}$ from the $dd \rightarrow {}^4\text{He}\pi^0$ reaction and for data after applying the two-dimensional cut on the cumulative probability distribution for the kinematic fit (see Sec. 5.3).
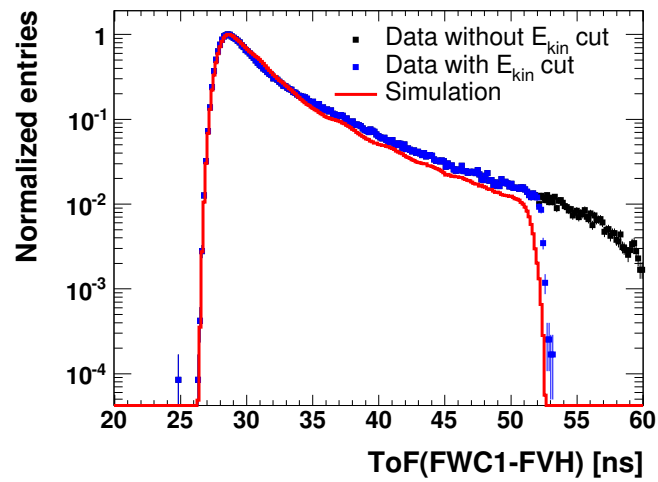
FIGURE 4.25: Time-of-flight for ^{3}He from the $dd \to {}^3\mathrm{He}n\pi^0$ reaction for data before the E_{kin} cut defined in Fig. 4.26 (black) and after this cut (blue). The simulated response is drawn with a red line. The plot is made for a polar angle between $3°$ and $6°$.
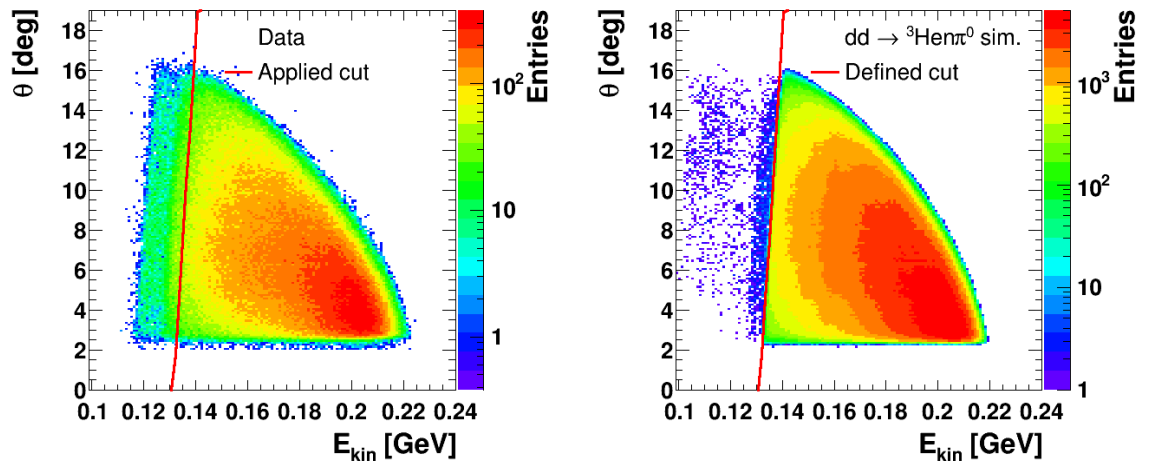
FIGURE 4.26: Kinetic energy versus polar angle of ^{3}He. **Left**: Data with the applied E_{kin} cut indicated with a red line. The selection of the data sample was optimized for the $dd \to {}^3\mathrm{He}n\pi^0$ reaction. **Right**: The same for the simulation of the $dd \to {}^3\mathrm{He}n\pi^0$ reaction. The cut for E_{kin} is defined with a red line.
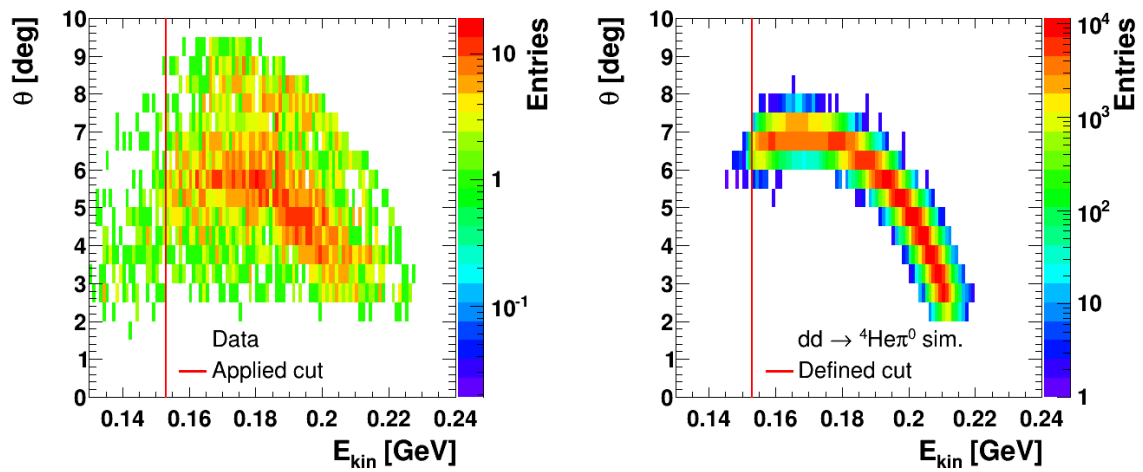
FIGURE 4.27: Kinetic energy versus polar angle of ^{4}He. **Left**: Data with the applied E_{kin} cut indicated with a red line. The selection of the data sample was optimized for the $dd \rightarrow {}^4$Heπ^0 reaction. **Right**: The same for the simulation of the $dd \rightarrow {}^4$Heπ^0 reaction. The cut for E_{kin} is defined with a red line.

Chapter 5

Selection of Signal Events

The general strategy for the analysis of the $dd \rightarrow {}^4\text{He}\pi^0$ reaction is the following. First, the $dd \rightarrow {}^4\text{He}\pi^0$ event candidates are selected using a chain of cuts and a kinematic fit. This is described in this chapter. Afterwards, the number of signal events as a function of the scattering angle θ^* of the outgoing π^0 in the c.m. coordinate system is obtained by a missing mass analysis. The whole analysis is performed separately for the 1st and the 2nd part of the beamtime. Finally, the results are combined.

For absolute normalization the integrated luminosity is determined using the $dd \rightarrow {}^3\text{He}n\pi^0$ reaction, which is described in Chapter 6. In the next step of the analysis, presented in Chapter 7, the acceptance correction is performed. Since the angular distribution of the $dd \rightarrow {}^4\text{He}\pi^0$ reaction is not known a priori, first a 2-body phase space generator is used. The extracted differential cross section is then used as input in a new event generator, and the analysis is repeated.

In this chapter, it is described how to extract events from the signal reaction, based on the reconstructed four-vectors of the π^0 candidates in the Central Detector and the ${}^4\text{He}$ and ${}^3\text{He}$ particles in the Forward Detector. Besides the signal reaction $dd \rightarrow {}^4\text{He}\pi^0$, the other main channels are: $dd \rightarrow pnd\pi^0$, $dd \rightarrow pnpn\pi^0$, $dd \rightarrow tp\pi^0$, $dd \rightarrow {}^4\text{He}\gamma\gamma$, and $dd \rightarrow {}^3\text{He}n\pi^0$. The first three reactions have a neutral pion in the final state, but no ${}^3\text{He}$ or ${}^4\text{He}$. Therefore, they can be separated easily from the other three reactions either in the analysis, or already on the trigger level by requiring a high energy deposit in the FWC which cuts events with protons or deuterons in the final state (see Sec. 3.2.5). More challenging is the suppression of the $dd \rightarrow {}^3\text{He}n\pi^0$ reaction, since ${}^3\text{He}$ and ${}^4\text{He}$ have similar energy losses in the FWC and time-of-flights. Furthermore, the cross section of the $dd \rightarrow {}^3\text{He}n\pi^0$ reaction is about five orders of magnitude larger than the signal cross section. The double radiative capture $dd \rightarrow {}^4\text{He}\gamma\gamma$ is an irreducible physics background.

In a first step, a preselection with basic cuts is performed to reduce the size of the data files (see Sec. 5.1). Then, a kinematic fit is performed. A general description of this method is presented in Sec. 5.2. In a next step, the final selection cuts are defined and optimized in Sec. 5.3.

The final signal extraction is done using the missing mass method. The mass M of a missing particle X in the reaction $dd \rightarrow {}^4\text{He}X$ can be written as:

$$M = \sqrt{(E_{in} - E_{{}^4\text{He}})^2 - (\vec{p}_{in} - \vec{p}_{{}^4\text{He}})^2}\,, \qquad (5.1)$$

where E_{in} and $\vec{p}_{in}$ are the sum of the deuteron energies and momenta from beam and target. $E_{{}^4\text{He}}$ and $\vec{p}_{{}^4\text{He}}$ are the energy and momentum of the outgoing ${}^4\text{He}$ particle. For events from the signal reaction, the missing mass should correspond to the π^0 mass. A fit of the missing mass spectra with all known contributions is performed with the aim of extracting the number of signal events. This is described in Sec. 5.4.

5.1 Preselection

In Fig. 5.1 the status of the data before the selection of the $dd \rightarrow {}^4\text{He}\pi^0$ events is presented. The calibrated energy loss versus time-of-flight is shown for the angular range of $6° - 9°$ for the first 15 runs of the beamtime. The reactions containing ${}^3\text{He}$ are marked. The ${}^4\text{He}$ from the $dd \rightarrow {}^4\text{He}\pi^0$ reaction events should be located above the ${}^3\text{He}$ from the $dd \rightarrow {}^3\text{He}n\pi^0$ reaction.
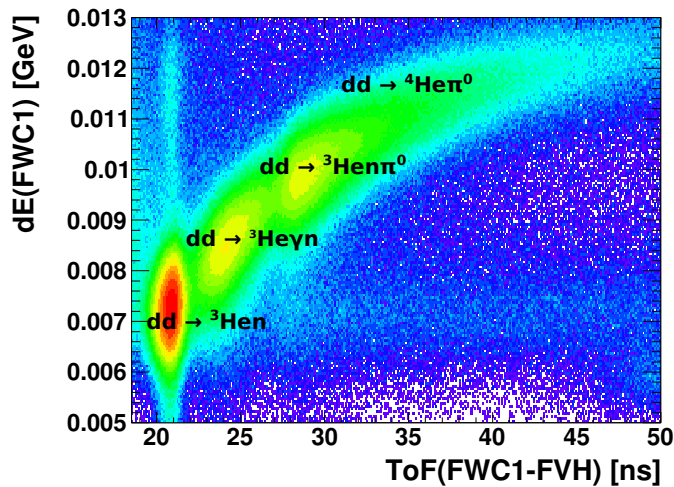
FIGURE 5.1: Calibrated energy losses versus time-of-flight. The islands of the three reactions containing ${}^3\text{He}$ in the final state are visible, namely $dd \rightarrow {}^3\text{He}n$, $dd \rightarrow {}^3\text{He}n\gamma$, and $dd \rightarrow {}^3\text{He}n\pi^0$. The ${}^4\text{He}$ from the $dd \rightarrow {}^4\text{He}\pi^0$ reaction events should be located above the ${}^3\text{He}$ from the $dd \rightarrow {}^3\text{He}n\pi^0$ reaction. The plot is made for θ between $6° - 9°$ for the first 15 runs of the beamtime.

To enhance the fraction of signal valid events and to decrease the time of the analysis, an event preselection is performed. At least two neutral clusters in the Central Detector are required, together with the condition of at least one track in the Forward Detector. The track reconstruction conditions are weaker than described in Sec. 4.2, and are based only on a geometrical overlap between the FWC and the FVH.

In addition, for every pair of neutral clusters in the CD a minimal opening angle of $30°$ between the clusters is required to suppress satellite clusters, where one particle generates more than one cluster. Furthermore, more refined off-line cuts on the energy losses in the FWC are applied: for every element of FWC1 and FWC2 the energy losses of ^{3}He from the $dd \rightarrow {^3}\mathrm{He}n$ reaction are fitted with a Gaussian function. The cut value is taken as the peak position minus five standard deviations, for every angular bin, $3°$ wide. The final cut for the element is taken as the lowest value from all the six angular bins. The cuts are defined using the last 50 runs from every part of the beamtime, when the effect from the dropping gain of the photomultipliers was the largest. In Fig. 5.2 the energy losses in every FWC1 element are presented together with the applied cuts for the 2nd part of the beamtime.

All conditions of the preselection are presented in Tab. 5.1.

TABLE 5.1: Preselection conditions.

Central Detector	
Type of clusters	neutral
Number of clusters	≥ 2
Total energy in cluster	≥ 20 MeV
Time difference between clusters	$\leq 20s$
Opening angle between clusters	$\geq 30°$
Forward Detector	
Number of tracks	≥ 1
dE in FWC	see Fig. 5.2
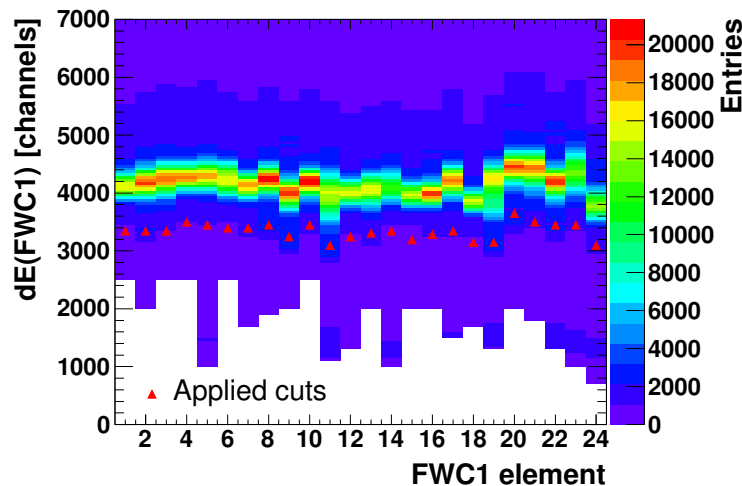
FIGURE 5.2: Energy losses of triggered particles in every FWC1 element. Final cuts applied in the preselection are marked with red triangles. The plot is made for the last 50 runs from the 2nd part of the beamtime.

5.2 Kinematic Fit

The purpose of the kinematic fit is to improve the precision of the measured kinematic variables (i.e., the kinetic energy E_{kin}, polar θ and azimuthal ϕ angles) and to serve as a selection criterion for background reduction. The idea is to vary the measured variables within an uncertainty range until certain kinematic constraints are fulfilled. The main constraint is the overall momentum and energy conservation. In addition, a constraint on the invariant mass of two photons from the π^0 decay can be applied. This constraint is optional. In case of the analysis of the signal reaction, it is not used, in order not to artificially enhance the peak from π^0 events.

The kinematic fit is a least square fit which minimizes a χ^2 function:

$$\chi^2 = \sum_{i=1}^{n} \left(\frac{v_i^{\text{meas}} - v_i^{\text{fit}}}{\sigma_i} \right)^2 , \tag{5.2}$$

where v_i^{meas} are the measured kinematic variables, σ_i are the uncertainties of this variables, and v_i^{fit} are the fit parameters, which are found by minimizing the χ^2 function with constraints such as the energy and momentum conservation. The minimization is based on the Lagrange multiplier technique [70].

In the analysis, three different kinematic fits are performed.

1. The $dd \to {}^4\text{He}\gamma\gamma$ hypothesis is tested to improve the description of the signal reaction and separate it from the main background. This hypothesis describes both the double radiative capture and the signal. No constraint on the invariant mass of the two photons is used, to avoid artificial enhancement of the π^0 peak.

2. The hypothesis of the $dd \to {}^3\text{He}n\gamma\gamma$ reaction is fitted to identify the contribution from the $dd \to {}^3\text{He}n\pi^0$ reaction and to separate it from the signal. No constraint on the two photon invariant mass is used.

3. Finally, also the $dd \to {}^3\text{He}n\gamma\gamma$ hypothesis with the constraint on the π^0 mass is tested. It is used for luminosity determination, which is based on the $dd \to {}^3\text{He}n\pi^0$ reaction.

In all cases shown above, the variables linked to beam and target are fixed in the fit. As an output from the kinematic fit, the minimal value of χ^2_{min} is given. The assumption of a χ^2 fit is that the uncertainties of all kinematic variables have a Gaussian shape. In this case, the distribution of χ^2_{min} for a true hypothesis should match a genuine χ^2 distribution for a particular number of degrees of freedom. Instead of using the χ^2_{min} distribution, also the complementary cumulative distribution can be used. In this thesis, following the nomenclature used in [2], it is called p-value. The p-value is the probability that, under the assumption of the null hypothesis, a χ^2 value equal or larger than the observed one was obtained:

$$p(N, \chi^2_{\text{min}}) = \frac{1}{2^{\frac{N}{2}} \Gamma\left(\frac{N}{2}\right)} \int_{\chi^2_{\text{min}}}^{\infty} e^{-\frac{t}{2}} t^{\frac{N}{2}-1} \, \mathrm{d}t . \tag{5.3}$$

Γ is the Gamma function, N is the number of degrees of freedom. For the true hypothesis, the p-value has a uniform distribution between 0 and 1. The number of degrees of freedom for the fitted hypothesis is equal to:

$$N_{\text{hyp}} = 4 + n_c - u\,. \tag{5.4}$$

The "4" is related to the overall energy and momentum conservation. The n_c stands for the number of additional constraints and u is a number of unmeasured variables. In case of the $dd \rightarrow {}^4\text{He}\gamma\gamma$ hypothesis, one has four degrees of freedom.

$$N_{dd \rightarrow {}^4\text{He}\gamma\gamma} = 4 + 0 - 0 = 4\,. \tag{5.5}$$

For the $dd \rightarrow {}^3\text{He}n\gamma\gamma$ reaction with no $M_{\gamma\gamma}$ constraint, the number of degrees of freedom is equal to one:

$$N_{dd \rightarrow {}^3\text{He}n\gamma\gamma} = 4 + 0 - 3 = 1\,. \tag{5.6}$$

The number of unmeasured variables is equal to 3 because the four-vector of the neutron is not measured and a constraint that the mass of the unmeasured particle is equal to the neutron mass is used ($u = 4 - 1 = 3$). For the hypothesis of $dd \rightarrow {}^3\text{He}n\gamma\gamma$ with the constraint on the mass of neutral pion, we have $n_c = 1$, therefore:

$$N_{dd \rightarrow {}^3\text{He}n\pi^0} = 4 + 1 - 3 = 2\,. \tag{5.7}$$

5.2.1 Error Parametrization

To get a proper result from the fit, the measurement errors of the variables have to be determined. In our case, the uncertainties of ϕ, θ and E_{kin} have to be obtained for all types of particles in the final state of the tested reactions. The error parametrization is based on simulations (after the simulation output has been matched to data, see Sec. 4.5). The reconstructed values of the kinematic variables from the detector simulation are compared with the true values from the generator. For each event the following differences are calculated:

$$\begin{aligned}
\Delta E_{kin} &= E_{kin}^{true} - E_{kin}^{rec}\,, \\
\Delta \theta &= \theta^{true} - \theta^{rec}\,, \\
\Delta \phi &= \phi^{true} - \phi^{rec}\,.
\end{aligned} \tag{5.8}$$

All distributions from Eq. 5.8 are fitted with a Gaussian function. The uncertainty is taken as the standard deviation from the fit. The parametrization is obtained as a function of the kinetic energy E_{kin} and the θ angle, since all calculated errors may depend on these variables. There is no dependence on the azimuthal angle ϕ because of the rotational symmetry of WASA.

For the parametrization, ^{3}He and ^{4}He tracks have been generated in a polar angular range between $2°$ and $18°$, and in a kinetic energy range of $0.15 - 0.22$ GeV for ^{4}He and $0.13 - 0.22$ GeV for ^{3}He. For reach 0.01 GeV wide E_{kin} bin and each $1°$ wide θ bin, $\sigma_{E_{kin}}$, σ_θ and σ_ϕ have been obtained. For the photons the parametrization is obtained in 0.01 GeV bins of E_{kin} in a range of $0.02 - 0.2$ GeV and in a θ range of $20° - 170°$ for $10°$ wide bins.

In Fig. 5.4 the error parametrization for ^{4}He is presented, the parametrization for ^{3}He is shown in Fig. 5.3, and for γ in Fig. 5.5. In the analysis, uncertainties for the fit are taken from these two-dimensional histograms.
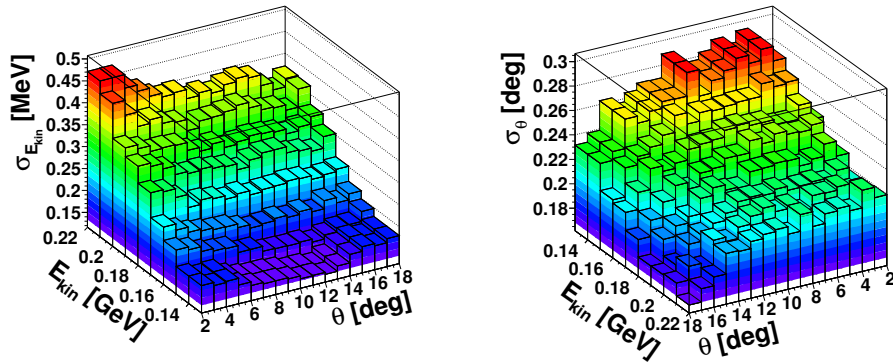
(A) The error parametrization for E_{kin}.

(B) The error parametrization for θ.
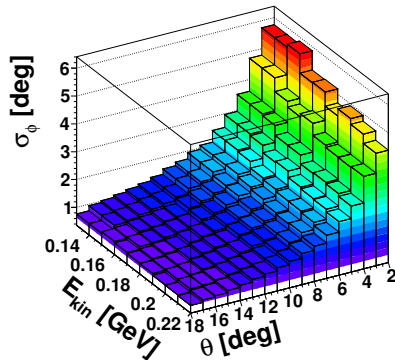
(C) The error parametrization for ϕ.

FIGURE 5.3: The E_{kin}, θ and ϕ error parametrization for ^{3}He.

5.2.2 Results

The fit has been performed on the preselected data set. If more than one track candidate in the FD is registered, or more than two photon candidates in the CD, all possible combinations are separately fitted. Finally, the combination with the smallest χ^2 is taken.

From the kinematic fit new corrected four-vectors are obtained. They fulfill the overall momentum and energy conservation, which has been set as a fit constraint. The minimal χ^2 value provides the information on how much the measured values are

(A) The error parametrization for E_{kin}.

(B) The error parametrization for θ.

(C) The error parametrization for ϕ.
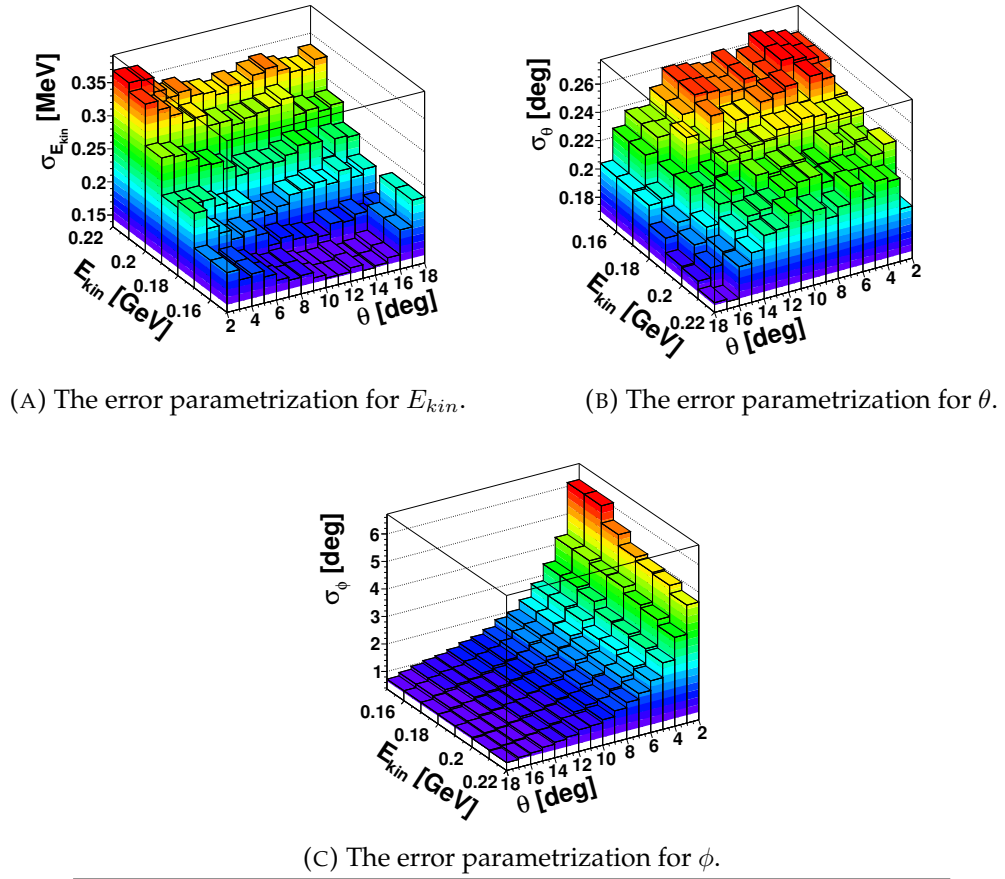
FIGURE 5.4: The E_{kin}, θ and ϕ error parametrization for ^{4}He.

corrected relative to the uncertainties. The performance of the fit can be also described using the p-value defined in Eq. 5.3.

The plots representing the χ^2 and p-value for all tested hypotheses are shown: for $dd \rightarrow {}^3\text{He}n\gamma\gamma$ in Fig. 5.6, for $dd \rightarrow {}^3\text{He}n\pi^0$ in Fig. 5.7, and for $dd \rightarrow {}^4\text{He}\gamma\gamma$ in Fig. 5.8. The χ^2 distributions are normalized to the same height for the data and simulations. The p-value histograms are normalized to the same height at a p-value of 0.3. One can see that the discrepancy between data and simulation is largest in Fig. 5.8. This is because the data sample is still dominated by the $dd \rightarrow {}^3\text{He}n\pi^0$ reaction by four orders of magnitude. For the other two histograms, the agreement gets worse for higher χ^2 values, because the measurement uncertainties do not follow a Gaussian distribution, but have longer tails. Therefore, the region of high χ^2 values and low p-values are more populated. Nevertheless, the p-value of the $dd \rightarrow {}^3\text{He}n\gamma\gamma$ hypothesis with and without mass constraint is flat in the region of $0.1 - 1$ (note the logarithmic scale). In the Fig. 5.7 the cut used for the luminosity determination is marked as a green dashed line.

The fitted kinematic variables are used in the further steps of the analysis. In addition, cuts on the p-value distributions are defined to reduce the amount of background for the $dd \rightarrow {}^4\text{He}\pi^0$ reaction (Sec. 5.3) and for the luminosity determination (Sec. 6).
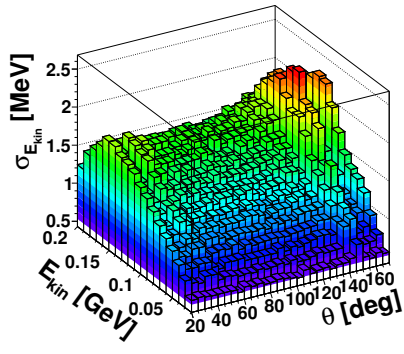
(A) The error parametrization for E_{kin}.
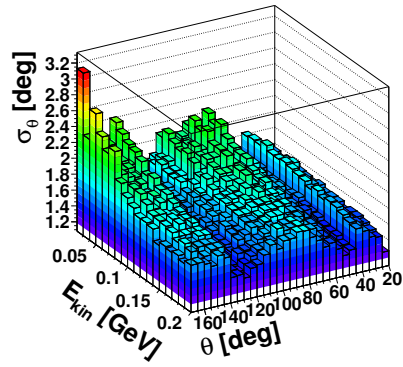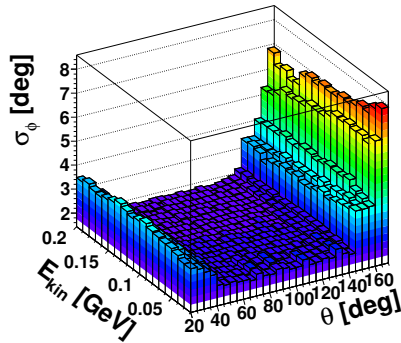
(B) The error parametrization for θ.

(C) The error parametrization for ϕ.

FIGURE 5.5: The E_{kin}, θ and ϕ error parametrization for γ.
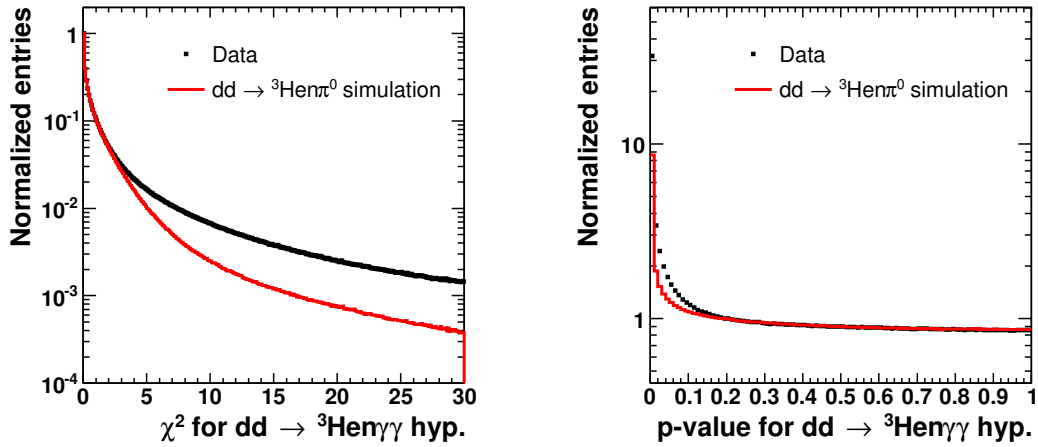
FIGURE 5.6: **Left**: χ^2 distribution for the kinematic fit of the $dd \rightarrow$ ^{3}He$n\gamma\gamma$ hypothesis. **Right**: p-value distribution for the kinematic fit of the $dd \rightarrow$ ^{3}He$n\gamma\gamma$ hypothesis. In both plots the data (black points) are dominated by the $dd \rightarrow$ ^{3}He$n\pi^0$ reaction. The simulation (red line) is performed for the $dd \rightarrow$ ^{3}He$n\pi^0$ reaction.
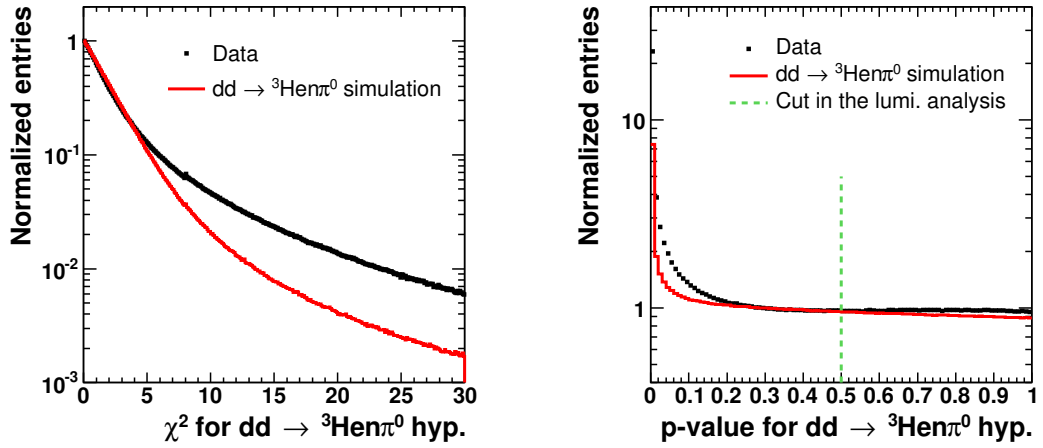
FIGURE 5.7: **Left**: χ^2 distribution for the kinematic fit of the $dd \rightarrow$ $^3\mathrm{He}n\pi^0$ hypothesis. **Right**: p-value distribution for the kinematic fit of the $dd \rightarrow {}^3\mathrm{He}n\pi^0$ hypothesis. The green dashed line at $p = 0.5$ indicates the cut applied for the luminosity determination. The data (black points) are dominated by the $dd \rightarrow {}^3\mathrm{He}n\pi^0$ reaction. The simulation (red line) is performed for the $dd \rightarrow {}^3\mathrm{He}n\pi^0$ reaction.
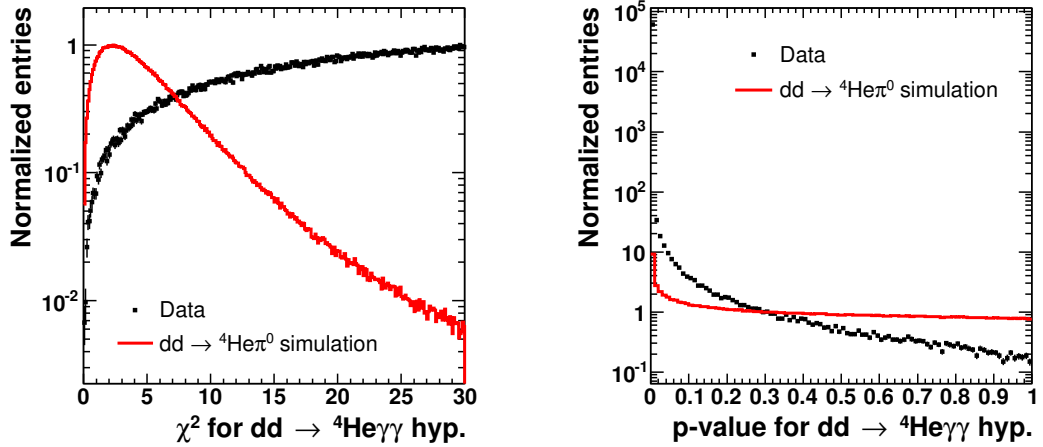
FIGURE 5.8: **Left**: χ^2 distribution for the kinematic fit of the $dd \rightarrow$ $^4\mathrm{He}\gamma\gamma$ hypothesis. **Right**: p-value distribution for the kinematic fit of the $dd \rightarrow {}^4\mathrm{He}\gamma\gamma$ hypothesis. The data (black points) are dominated by the $dd \rightarrow {}^3\mathrm{He}n\pi^0$ reaction. The simulation (red line) is performed for the $dd \rightarrow {}^4\mathrm{He}\pi^0$ reaction.

5.3 Main Cuts of the Signal Selection

In this section the main cuts for the selection of the signal reaction are presented.

For every event the $dd \rightarrow {}^4\mathrm{He}\gamma\gamma$ hypothesis has been fitted. If there is more than one track in the FD or more than two neutral clusters in the CD, the combination with the smallest χ^2 is chosen. For this combination, the $dd \rightarrow {}^3\mathrm{He}n\gamma\gamma$ hypothesis is also fitted. If in case of the $dd \rightarrow {}^3\mathrm{He}n\gamma\gamma$ hypothesis the fit does not converge, the event

is anyhow saved, setting the p-value to zero for this hypothesis. For the sample with a fitted $dd \to {}^4\mathrm{He}\gamma\gamma$ hypothesis, a loose cut on the χ^2 distribution from the kinetic energy reconstruction of $^4\mathrm{He}$ is applied: $\chi^2 < 30$ (see Fig. 4.17). In addition, θ and E_{kin} of $^3\mathrm{He}$ and $^4\mathrm{He}$ from the simulations of the signal and background reactions have also been compared (see Fig. 5.9). In the analysis a cut on $\theta < 9°$ is applied. A cut on E_{kin} has been tested, but was later discarded, as it did not improve the background reduction with respect to the cut on the p-value from the kinematic fit.
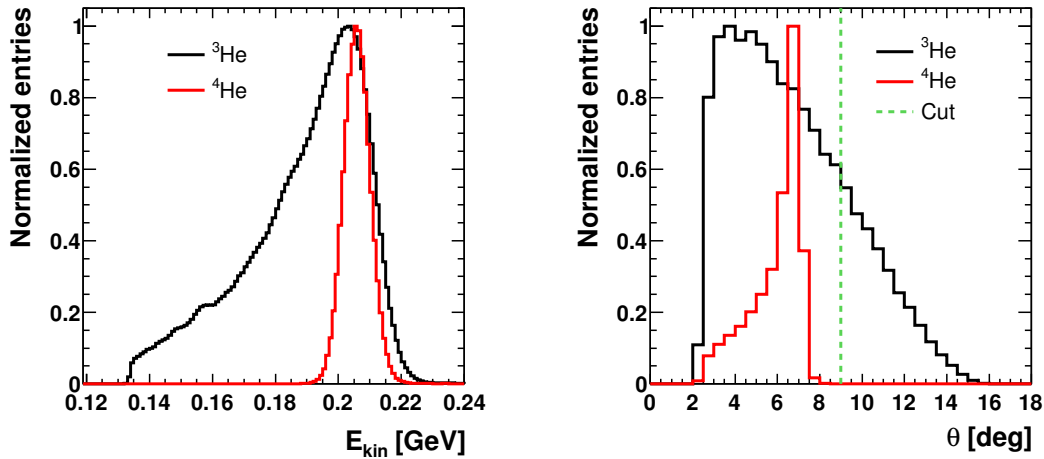
FIGURE 5.9: **Left:** Kinetic energy of $^4\mathrm{He}$ from the simulation of the $dd \to {}^4\mathrm{He}\pi^0$ (red) reaction and $^3\mathrm{He}$ from the simulation of the $dd \to {}^3\mathrm{He}n\pi^0$ reaction (black) for the angular bin $6° - 9°$. **Right:** Polar angle of the same particles. The cut applied in the analysis is marked with a green dashed line. Plots are normalized to the same height.

A significant reduction of the $dd \to {}^3\mathrm{He}n\pi^0$ background is only possible using a cut on the two-dimensional p-value distribution from the kinematic fits. In Fig. 5.10 the p-value for the $dd \to {}^4\mathrm{He}\gamma\gamma$ hypothesis versus the p-value for the $dd \to {}^3\mathrm{He}n\gamma\gamma$ hypothesis is plotted for data and simulations of the $dd \to {}^4\mathrm{He}\pi^0$ and $dd \to {}^3\mathrm{He}n\pi^0$ reactions. The $dd \to {}^4\mathrm{He}\pi^0$ events form a uniform distribution for the $dd \to {}^4\mathrm{He}\gamma\gamma$ hypothesis are located in the low p-value region for the $dd \to {}^3\mathrm{He}n\gamma\gamma$ hypothesis. The events from the $dd \to {}^4\mathrm{He}\gamma\gamma$ reaction have the same signature. The situation is opposite for the $dd \to {}^3\mathrm{He}n\pi^0$ reaction. The final cut is based on Monte Carlo simulations and is indicated with a red line.

For optimization purposes, the cut has been varied in the horizontal and vertical direction, as it is shown in the bottom row of Fig. 5.10. For every combination of a horizontal and vertical cut the missing mass for the $dd \to {}^4\mathrm{He}X$ reaction is fitted with the Monte Carlo templates consisting of the signal and background contributions, i.e., $dd \to {}^4\mathrm{He}\pi^0$, $dd \to {}^3\mathrm{He}n\pi^0$ and $dd \to {}^4\mathrm{He}\gamma\gamma$. This fit is described in detail in the following Sec. 5.4. The missing mass plots have been obtained using the particles four-vectors from the kinematic fit with the $dd \to {}^4\mathrm{He}\gamma\gamma$ hypothesis. For every cut definition, the statistical significance R of the signal is calculated in the region
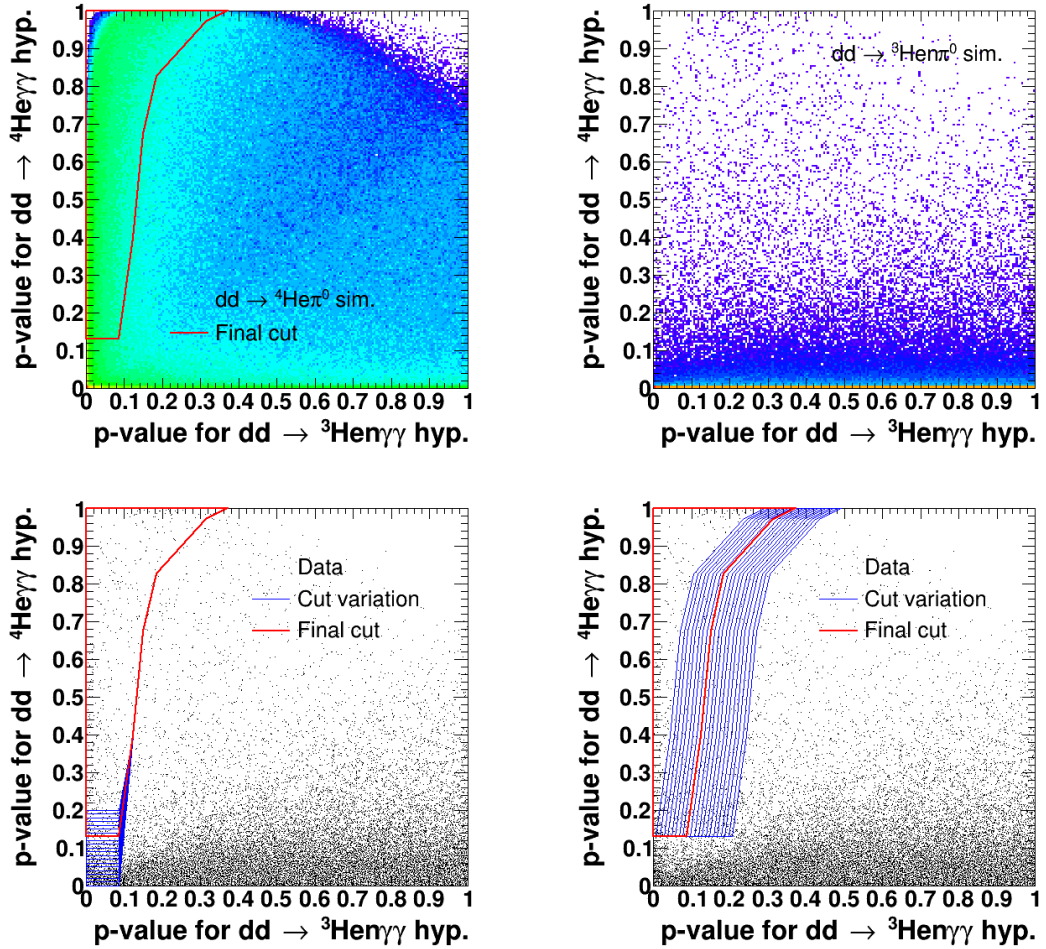
FIGURE 5.10: Two-dimensional distributions of the p-value from the kinematic fits of the $dd \to {}^4\text{He}\gamma\gamma$ hypothesis and the $dd \to {}^3\text{He}n\gamma\gamma$ hypothesis. In the upper row, the distributions for the $dd \to {}^4\text{He}\pi^0$ and $dd \to {}^3\text{He}n\pi^0$ simulations are presented. In the bottom row, the distributions for data are plotted. The final two-dimensional cut applied in the analysis is presented with a red line. The cut variations in the horizontal and vertical directions used in the studies of systematic effects are marked with blue lines.

of the π^0 peak $0.11 - 0.15 \,\text{GeV}/c^2$ using the formula:

$$R = \frac{S}{\sqrt{S + B}}, \tag{5.9}$$

where S is the number of signal events and B is the number of background events. In Fig. 5.11 the significance is shown for a variation of the cut for the 1st and the 2nd part of the beamtime. The final cut maximizes the significance for both parts of the beamtime. The varied vertical cuts are numbered from 0 to 20 from the most restrictive to the loosest one and the varied horizontal cuts are numbered from 0 to 20 from the loosest to the most restrictive one (see Fig. 5.10).
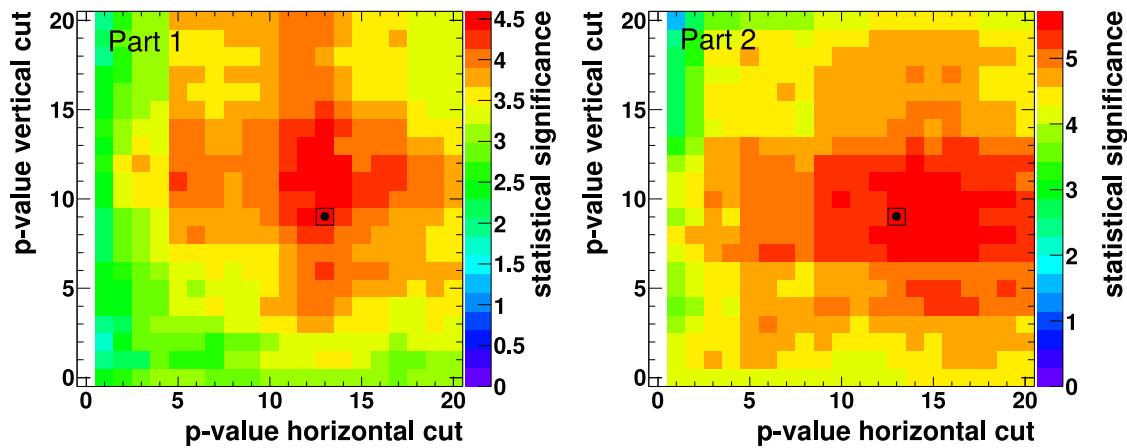
FIGURE 5.11: Statistical significance of the π^0 mass peak in the spectra of missing mass for the $dd \to {}^4\mathrm{He}X$ reaction for different p-value cuts. The variation of the cut is presented in Fig. 5.10. **Left**: Distribution for the 1st part of the beamtime. **Right**: Distribution for the 2nd part of the beamtime. The black dots indicate the significances for the final cut which is shown in Fig. 5.10 with a red line.

5.4 Missing Mass Fit

The four-momenta obtained from the kinematic fit with the $dd \to {}^4\mathrm{He}\gamma\gamma$ hypothesis are used to calculate the missing mass for the reaction $dd \to {}^4\mathrm{He}X$. In this section, the missing mass spectra are fitted with Monte Carlo templates to obtain the number of the registered signal events.

To determine the angular distribution, the spectra are obtained as a function of the scattering angle θ^* of the outgoing particle X in the c.m. coordinate system. The data are divided into four angular bins within the detector acceptance ($-0.9 \le \cos\theta^* \le 0.4$):

- bin 1: $-0.9 \le \cos\theta^* < -0.6$,

- bin 2: $-0.6 \le \cos\theta^* < -0.3$,

- bin 3: $-0.3 \le \cos\theta^* < 0$,

- bin 4: $0 \le \cos\theta^* \le 0.4$.

The widths of bins have been chosen to have a similar number of events and a visible π^0 mass peak in each bin. In Fig. 5.12 $\cos\theta^*$ versus the missing mass is shown; the angular bins are marked with red lines.

Fig. 5.13 shows the missing mass spectra for the whole $\cos\theta^*$ region of $-0.9 \le \cos\theta^* 0.4$. The π^0 mass peak is visible on top of a broad background. The spectra are fitted with a linear combination of the simulated signal reaction and background originating from $dd \to {}^3\mathrm{He}n\pi^0$ and $dd \to {}^4\mathrm{He}\gamma\gamma$. Other sources of background have been already eliminated by the trigger requirements (Sec. 3.2.5), the preselection cuts (Sec. 5.1), and the $dd \to {}^4\mathrm{He}\pi^0$ extraction cuts (Sec. 5.3).
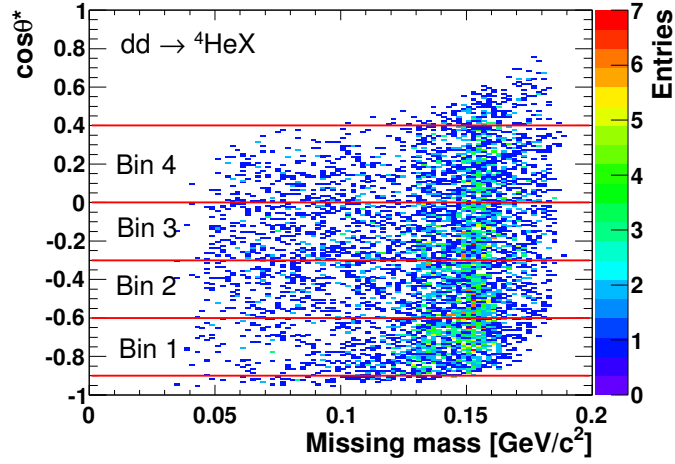
FIGURE 5.12: $\cos\theta^*$ of outgoing particle X in the c.m. coordinate system versus the missing mass for $dd \rightarrow {}^4\text{He}X$. Four angular bins are defined. The plot is made for all data from both parts of the beamtime.

To obtain the individual templates, high-statistics samples have been generated from Monte Carlo simulations, i.e., 10^8 $dd \rightarrow {}^3\text{He}n\pi^0$ events, $2.5 \cdot 10^6$ $dd \rightarrow {}^4\text{He}\gamma\gamma$ events, and $2.5 \cdot 10^6$ $dd \rightarrow {}^4\text{He}\pi^0$ events. For each $\cos\theta^*$ bin, an independent fit of the Monte Carlo templates to the data is performed, with the constraint that the sum of fitted templates have to fit the missing mass spectra for all angular bins together (Fig. 5.13). The fit has been performed separately for the 1st and the 2nd part of the beamtime. The missing mass distribution for every angular bin is presented in Fig. 5.14 and Fig. 5.15. In order to determine the number of signal events, the background contributions have been subtracted in the peak region $0.11 - 0.15\,\text{GeV}/c^2$.
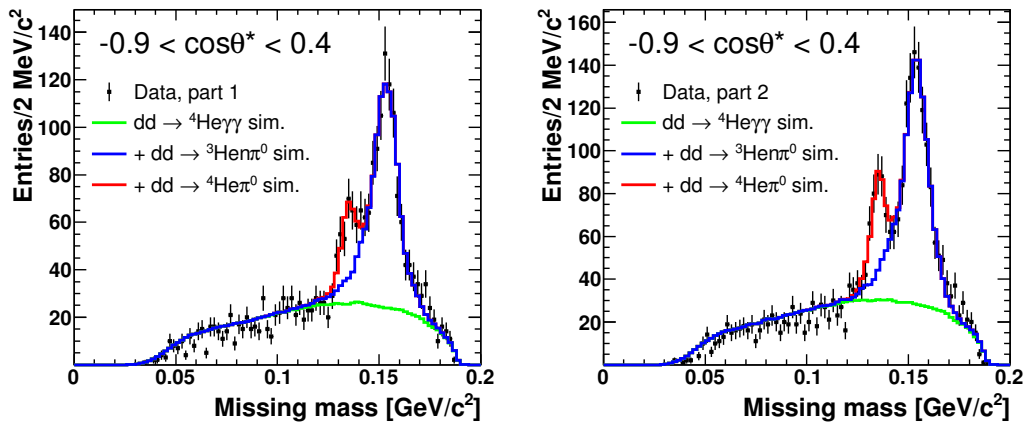
FIGURE 5.13: Missing mass for the $dd \rightarrow {}^4\text{He}X$ reaction for $-0.9 \leq \cos\theta^* \leq 0.4$ for the 1st (left) and the 2nd (right) part of the beamtime. The spectra are fitted with a linear combination of the simulated signal and background reactions: $dd \rightarrow {}^4\text{He}\gamma\gamma$ (green line), plus $dd \rightarrow {}^3\text{He}n\pi^0$ (blue line), plus $dd \rightarrow {}^4\text{He}\pi^0$ generated with 2-body phase space (red line).
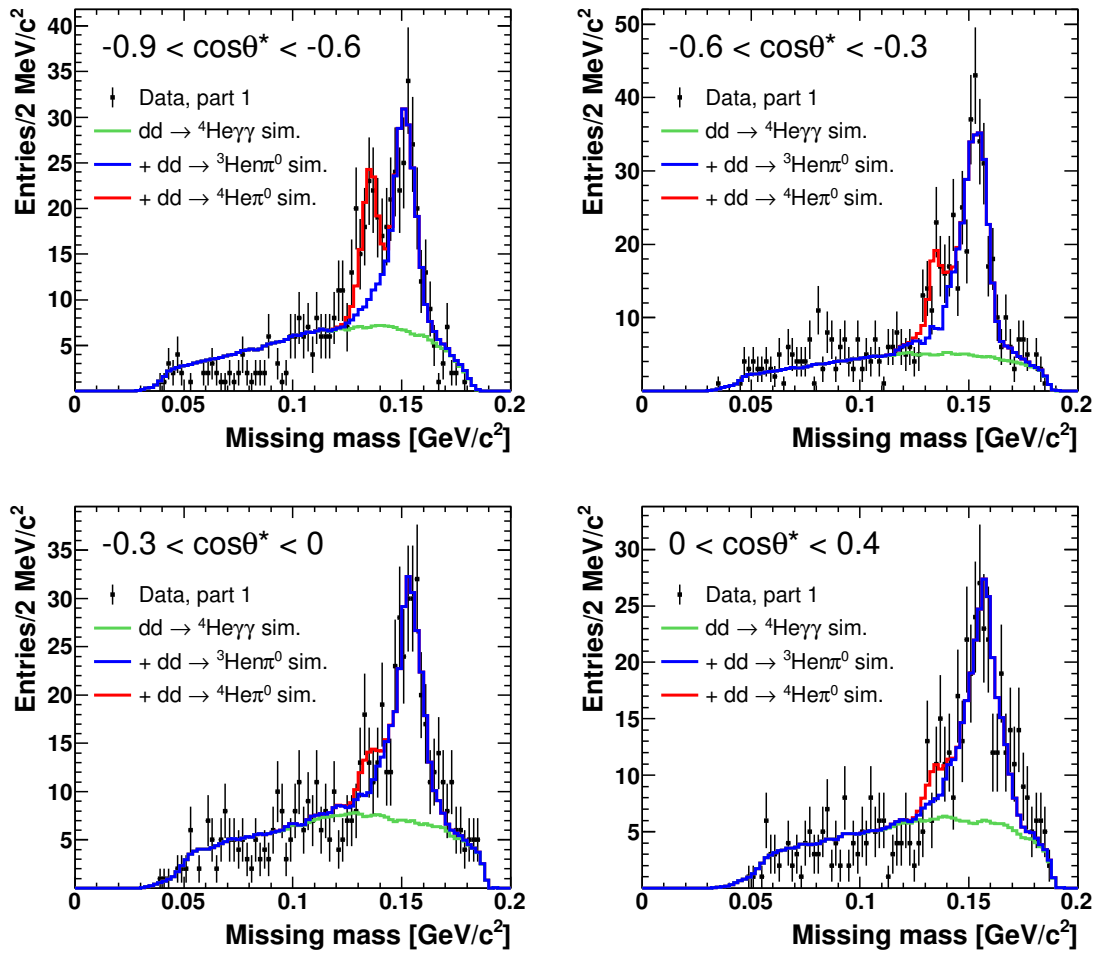
FIGURE 5.14: Missing mass for the $dd \rightarrow {}^{4}\mathrm{He}X$ reaction for every $\cos\theta^*$ bin for the 1st part of the beamtime. The fitted Monte Carlo template is the same as presented in Fig. 5.13.
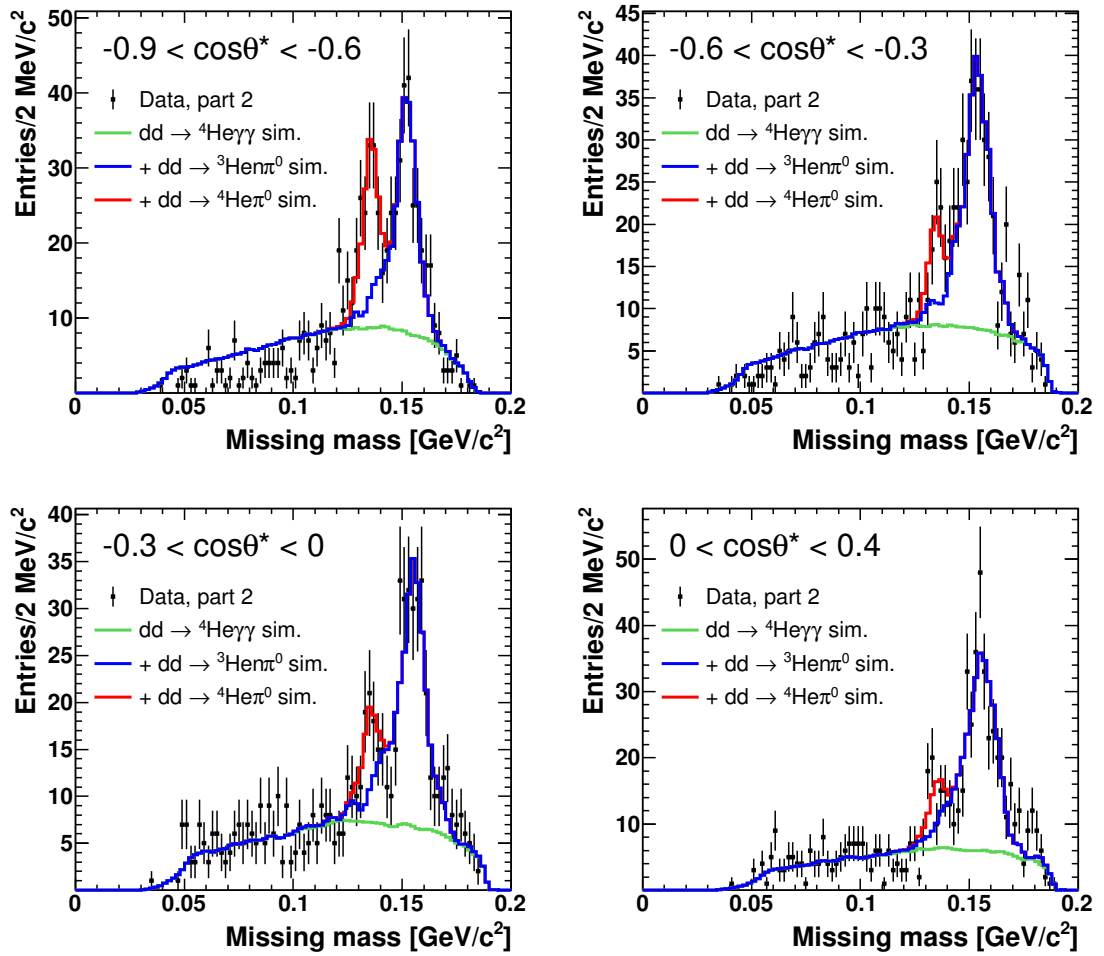
FIGURE 5.15: Missing mass for the $dd \to {}^4\mathrm{He}X$ reaction for every $\cos\theta^*$ bin for the 2nd part of the beamtime. The fitted Monte Carlo template is the same as presented in Fig. 5.13.

Chapter 6

Luminosity Determination

This chapter shows how the integrated luminosity has been determined. From the measurement of a reaction with a known cross section σ, which was registered together with the signal during the same data collection period, one can obtain the integrated luminosity L in the following way:

$$L = \frac{N}{\epsilon \cdot \sigma} \, , \qquad (6.1)$$

where ϵ describes acceptance times cut efficiencies, and N stands for the number of events.

In this thesis, the integrated luminosity has been calculated from the $dd \to {}^3\mathrm{He}n\pi^0$ reaction which was measured previously with WASA at $p_d = 1.2\,\mathrm{GeV}/c$ [64]. The analysis of this reaction is presented in Sec. 6.1. Systematical effects are discussed in Sec. 6.2.

6.1 Analysis of the $dd \to {}^3\mathbf{He}n\pi^0$ Reaction

The $dd \to {}^3\mathrm{He}n\pi^0$ reaction was included in the main trigger described in Sec. 3.2.5. The dropping gain of the photomultipliers did not cause any loss in efficiency for this reaction because the effective trigger thresholds stayed far below the energy losses of the ${}^3\mathrm{He}$ originating from it.

The luminosity has been determined separately for the 1st and the 2nd part of the beamtime. For the preselected data, a kinematic fit has been applied for the $dd \to {}^3\mathrm{He}n\pi^0$ hypothesis. If there was more than one good track in the FD and more than two photon candidates, the combination with the smallest χ^2 was chosen. In addition, two more requirements have been defined:

- The χ^2 of the E_{kin} reconstruction has to be < 30. It is a loose cut to remove events with badly reconstructed E_{kin} (see Fig. 4.17).

- The p-value from the kinematic fit should be > 0.5 (see Fig. 5.7). This value has been determined after checking the influence of the probability cut on the luminosity (see Sec. 6.2). It is possible to use such a very tight cut, due to the large statistics.

The reaction is fully described by four independent variables based on the Jacobi momenta $\vec{q}$ and $\vec{p}$. $\vec{q}$ is the π^0 momentum in the c.m. system, while $\vec{p}$ is the momentum of ^{3}He in the rest frame of the ^{3}He $- n$ subsystem. These variables are:

- $\cos\theta_p$ - the cosine of the polar angle between the beam direction and $\vec{p}$ in the overall c.m. system.

- $\cos\theta_q$ - the cosine of the polar angle between the beam direction and $\vec{q}$ in the overall c.m. system.

- $M_{^3\text{He}n}$ - the invariant mass of the ^{3}He-neutron system.

- φ - the angle between the projections of $\vec{q}$ and $\vec{p}$ onto the x-y plane.

In Fig. 6.1 the kinematic spectra with the integral normalized to 1 are presented for data and simulation for the 1st part of the beamtime. The agreement between data and simulation is similar as in [63, 64]. The small discrepancy for the invariant mass of ^{3}Hen can be linked to effects which are not implemented in the model as, e.g., final-state interaction or the presence of resonances. The agreement for the spectra obtained for the 2nd part of the beamtime is similar.

Since the agreement between data and model was shown to be good, the acceptance and cut efficiency is calculated using the simulation. 10^8 events of the $dd \rightarrow {}^3\text{He}n\pi^0$ reaction were generated. The number of events, in acceptance of the detector, which survived the selection cuts has been divided by the number of generated events. The luminosity is obtained from Eq. 6.1 using the total cross section of $dd \rightarrow {}^3\text{He}n\pi^0$: $\sigma_{\text{tot}} = (2.89 \pm 0.01(\text{stat.}) \pm 0.06(\text{syst.}) \pm 0.29(\text{norm.}))$ μb. In Tab. 6.1 the results for the 1st and the 2nd part of the beamtime are presented. The error shown in the table stems from the error on the $dd \rightarrow {}^3\text{He}n\pi^0$ cross section. The statistical error is negligible (about 0.03%).

TABLE 6.1: Results of the luminosity calculation for the 1st and the 2nd part of the beamtime.

	1st part	2nd part
Number of $dd \rightarrow {}^3\text{He}n\pi^0$ ev.	5545240	6777114
Acceptance $\cdot$ Cut efficiency	12%	12%
Integrated luminosity	$(16.1 \pm 1.6(\text{norm.}))$ pb^{-1}	$(19.6 \pm 2.0(\text{norm.}))$ pb^{-1}

6.2 Systematic Effects

In order to study systematic effects, the cut on the p-value of the kinematic fit and on the χ^2 distribution from the kinetic energy reconstruction are varied in a wide range: $0.05 - 0.8$ for the p-value cut, and $20 - 110$ for the χ^2 cut. Following the method described in [109], the difference between the final value of the integrated luminosity
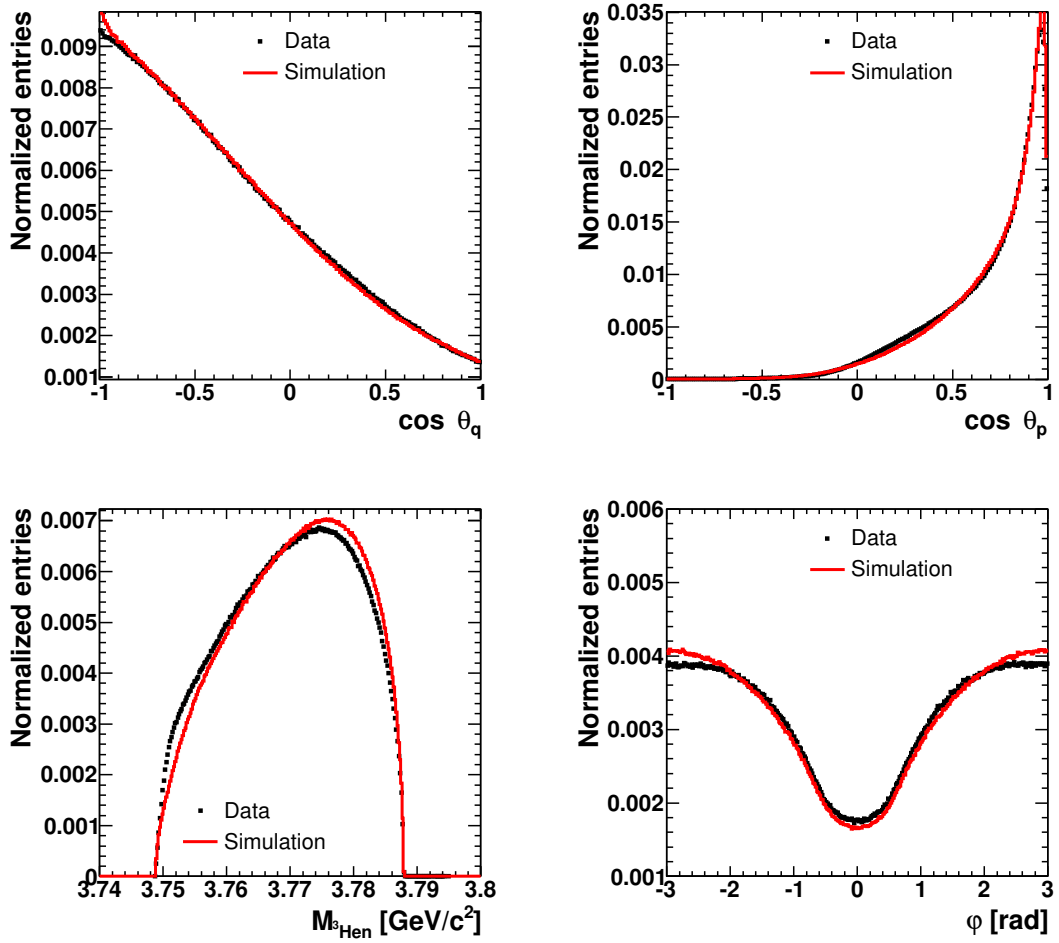
FIGURE 6.1: Kinematic variables $\cos_{\theta_p}$, $\cos_{\theta_q}$, $M_{^3\text{He}n}$, φ describing the $dd \rightarrow {}^3\text{He}n\pi^0$ reaction (for the definition see text). The black point represents data, the red histograms present the simulation. The plots show data for the 1st part of the beamtime.

and the values with varied cuts is checked. It has to be decided if this difference is significant, but what does this mean?

Let us assume that the value a_r is measured with statistical uncertainty σ_r. This is our reference value. The selection cut in the analysis is varied to make it tighter, and the value $a_v \pm \sigma_v$ is obtained for a subset of the reference data. It is also possible that the cut is looser, i.e., that the reference result comes from a subset of the data with the varied cut. Now, the difference $\Delta = |a_r - a_v|$ is considered. It has to be checked whether this difference can be explained by statistics only.

It can be shown (see [109]) that the statistical error on Δ is $\sigma_\Delta^2 = \left| \sigma_v^2 - \sigma_r^2 \right|$. Comparing the difference Δ to σ_Δ, one can judge how significant it is in comparison to its statistical uncertainty. Here, the following criterion has been chosen: if the ratio of Δ/σ_Δ is larger than 3, then the cut is subject to a systematic uncertainty.

The ratio between Δ and σ_Δ has been checked for every variation of the cut. All

differences Δ turned out to be significant. This is linked to the fact that the statistical uncertainty of the calculated luminosity is already very small. Therefore, all cuts should be considered as the origin of a systematic error. In Fig. 6.2 the difference between the reference luminosity L_r and the luminosity L_v for different cuts on the p-value from the kinematic fit and the value of χ^2 of kinetic energy reconstruction is shown. The behaviour of this difference is similar for both parts of the beamtime. Based on this distributions, a p-value cut on 0.5 has been selected to obtain the averaged cross section together with the systematic error. For every type of cut, the maximal positive and negative deviations from the reference value are taken as systematic uncertainties. These uncertainties are added according to the formula:

$$\sigma(\text{syst.})_{+/-} = \sqrt{\left(\Delta_{+/-}^{E_{kin}}\right)^2 + \left(\Delta_{+/-}^{\text{kFit}}\right)^2},\tag{6.2}$$

where $\Delta^{E_{kin}}$ is the maximal deviation from the reference value for the cut on the value of χ^2 of E_{kin} reconstruction, Δ^{kFit} is the maximal deviation from the reference value for the cut on the p-value from the kinematic fit, and $+/-$ refers to the positive or negative deviation. The obtained values of the luminosity including the systematic uncertainties are:

$$L_1 = (16.1 \pm 0.4(\text{syst.}) \pm 1.6(\text{norm.})) \, \text{pb}^{-1}, \tag{6.3a}$$

$$L_2 = (19.6 \pm 0.5(\text{syst.}) \pm 2.0(\text{norm.})) \, \text{pb}^{-1}. \tag{6.3b}$$
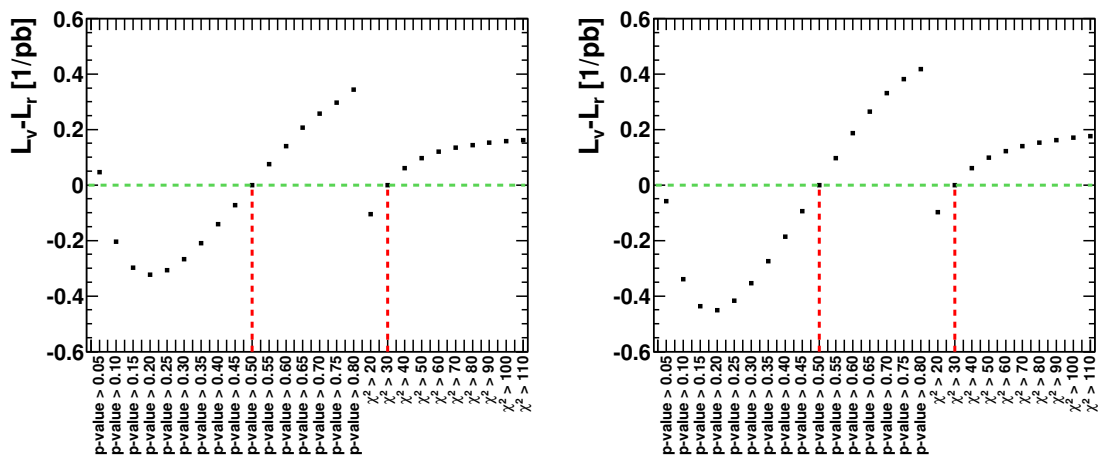
FIGURE 6.2: Difference between the reference luminosity L_r and the luminosity L_v for different cuts on the p-value from the kinematic fit and the value of χ^2 of the kinetic energy reconstruction (black points). The reference values are marked with a red line. Zero is marked with a green dashed line. The **left** plot is made for the 1st part of the beamtime and the **right** plot for the 2nd one.

Chapter 7

Results

In this chapter the results of the analysis are presented. Having the number of registered signal events N and the integrated luminosity L, the missing information to obtain the total and differential cross sections is the combined acceptance and efficiency (ϵ).

Since the angular distribution from the previous measurement of $dd \rightarrow {}^4\mathrm{He}\pi^0$ is not decisive in identifying contributions of higher partial waves [53], the following strategy is used. First, the acceptance correction is done using a 2-body phase space generator. From this analysis, a first result for the differential cross section is determined. This is presented in Sec. 7.1. Based on that, a new signal generator is constructed using the correct angular distribution. With this, the final values for the total and differential cross section are determined. The results from both parts of the beamtime are combined together in a last step. These results are presented in Sec. 7.2.

7.1 Results with the Phase Space Generator

As our goal is to obtain the angular distribution, the cross section within every angular bin has to be determined. This is done using the following formula:

$$\frac{\mathrm{d}\sigma}{\mathrm{d}\Omega} = \frac{1}{L \cdot \epsilon} \cdot \frac{\Delta N}{2\pi \cdot \Delta \cos \theta^*} \, , \tag{7.1}$$

where L is the integrated luminosity, ΔN is the number of signal events in a particular angular bin $\Delta \cos \theta^*$, and ϵ is the acceptance times the cut efficiencies which is determined using a Monte Carlo sample. The number of events in each angular bin after all analysis cuts is divided by the number of generated events in this bin.

The angular distributions for the 1st and the 2nd part of the beamtime are presented in Fig. 7.1. In this plot only the statistical uncertainties are shown. The study of the systematic effects is presented in the following section.

7.1.1 Systematic Effects

In the course of the analysis the following potential systematic effects have been observed.
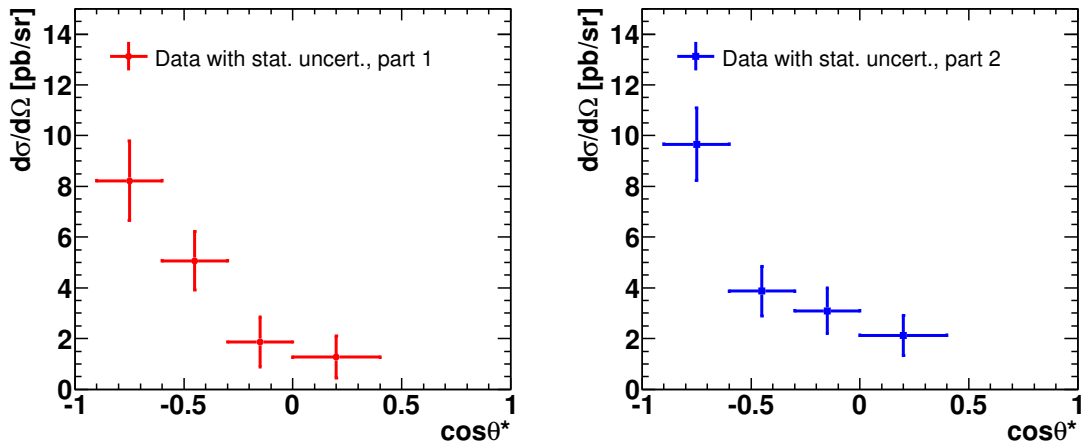
FIGURE 7.1: Angular distribution for the 1st (left) and the 2nd (right) part of the beamtime obtained with the 2-body phase space generator of the signal. In the plot only the statistical uncertainties are presented.

In the missing mass spectra, the background originating from misidentified $dd \rightarrow$ $^{3}\mathrm{He}n\pi^{0}$ events is slightly shifted in comparison to the simulation. The largest effect is visible for forward angles. The reason of this shift can be attributed systematic differences in the simulated detector response for $^{4}\mathrm{He}$ and $^{3}\mathrm{He}$. The limited statistics after all cuts does not allow to study the reason of this effect in detail. To compensate the mismatch, an angular dependent scaling factor is introduced for the missing mass of the $dd \rightarrow$ $^{3}\mathrm{He}n\pi^{0}$ background. It is included in the fit as a free parameter. The obtained factors for the angular bins defined above (from backward to forward) are: 1.005, 0.996, 0.991, 0.972 for the 1st part of the beamtime, and 1.003, 0.988,0.981, 0.980 for the 2nd part of the beamtime. No additional systematic error is assigned to this effect, since the resulting fit describes the shape of the background in the region of the π^{0} mass peak.

Another systematic effect is linked to a mismatch in the missing mass region below $0.11 \, \mathrm{GeV}/c^{2}$ in the most backward angular bin. The fit shows that this region is dominated by the $dd \rightarrow$ $^{4}\mathrm{He}\gamma\gamma$ reaction, which has been simulated using 3-body phase space. This model does not provide a perfect description. However, the dominating background from the $dd \rightarrow$ $^{3}\mathrm{He}n\pi^{0}$ reaction at higher missing masses does not allow to describe all contributions precisely enough to verify more advanced models. There is the possibility of addressing this problem with an improved $dd \rightarrow$ $^{3}\mathrm{He}n\pi^{0}$ subtraction using the energy loss information from the FVH. However, this was not a part of this thesis and is planned as a separate project in the next stage of the data analysis. The final fit excludes the missing mass range below $0.11 \, \mathrm{GeV}/c^{2}$. Nevertheless, in order to estimate the size of a possible systematic effect, the fit in the first angular bin has also been performed in the full range, but with a modified template. The $dd \rightarrow$ $^{4}\mathrm{He}\gamma\gamma$ contribution has been multiplied by the function $f(x) = \frac{1}{2}\tanh(ax+b) + \frac{1}{2}$ to describe the data in the range $0 - 0.11 \, \mathrm{GeV}/c^{2}$ of the missing mass. This function has been

chosen because it describes a smooth step between zero and one at $x = b$. Therefore, it diminishes the $dd \rightarrow {}^4\mathrm{He}\gamma\gamma$ template at missing masses smaller than $\sim 0.11\,\mathrm{GeV}/c^2$ and does not change it above this value. In Fig. 7.2 the missing mass distribution for the most backward angular bin fitted with the modified Monte Carlo template is presented. The differences in cross section of -3% for the 1st part of the beamtime and -1.5% for the 2nd one are included in the systematic uncertainties.
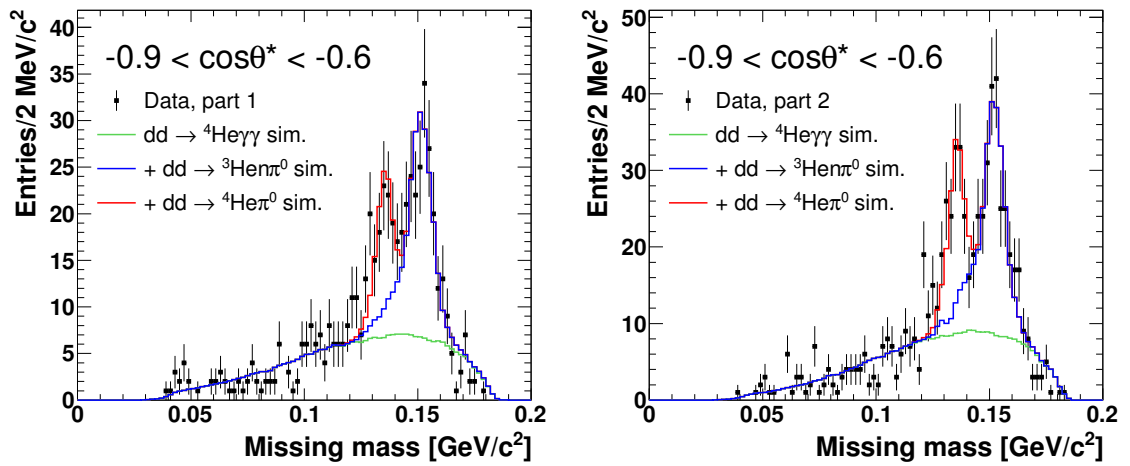
FIGURE 7.2: Missing mass for the $dd \rightarrow {}^4\mathrm{He}X$ reaction for the most backward angular bin $-0.9 \leq \cos\theta^* < -0.6$ fitted with the low mass region included with the modified Monte Carlo template, where the $dd \rightarrow {}^4\mathrm{He}\gamma\gamma$ contribution is multiplied by the function $f(x) = \frac{1}{2}\tanh(ax+b) + \frac{1}{2}$.

Further tests of the systematic effects follow the method described in Sec. 6.2. The selection cuts applied in the analysis have been varied to check the influence on the differential cross section in every angular bin. The p-value cut of the kinematic fit has been varied in the regions presented in Fig. 5.10. Fixing the horizontal cut, the vertical cut has been shifted in steps of 0.01, and vice versa. For each shift, the differential cross section in every $\cos\theta^*$ bin is calculated, and the difference Δ between the reference value and the varied one is obtained. This difference is compared to its statistical uncertainty calculated with the formula $\sigma_\Delta^2 = \left|\sigma_v^2 - \sigma_r^2\right|$, where $\sigma_{v/r}$ is the statistical uncertainty of the varied or reference result. If the ratio is larger than 3, Δ is considered in the estimation of the systematic uncertainty. In Fig. 7.3 an example plot of the differential cross section for different cut variations is presented for the first angular bin. The points marked in red indicate those variations, which are statistically significant. Similarly, the systematic effects associated with the χ^2 cut from the kinetic energy fit as well as the cut on the polar angle of outgoing particles in the FD have been checked. The χ^2 cut has been varied from 20 to 110 in steps of 10, while the θ cut was shifted first to $9 > \theta > 3$, and than to $2 < \theta < 8$. In both cases, no significant statistical shift has been observed.
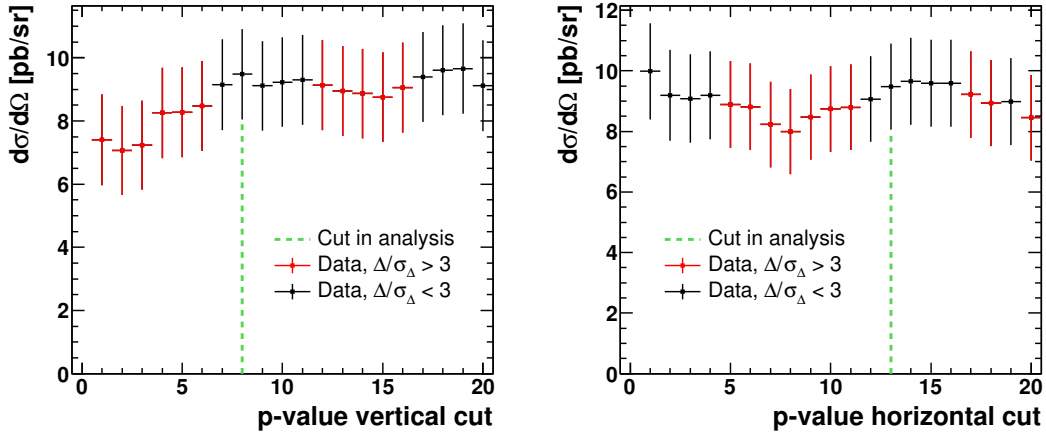
FIGURE 7.3: Example of differential cross section for the 1st angular bin $-0.9 \leq \cos \theta^* < -0.6$ for the variation of the p-value cut. The points marked in red indicate variations, which are statistically significant.

The obtained systematic uncertainties for every bin are included in the angular distribution presented in Fig. 7.4 belonging to the next section.

7.1.2   Fit of Angular Distribution

The aim of the analysis is to identify contributions from higher partial waves. Taking into account only terms that contribute to the unpolarized intensity up to order $p_{\pi^0}^2$ — according to [110] — the unpolarized differential cross section of $dd \rightarrow {}^4\text{He}\pi^0$ has the form:

$$\frac{p}{p_{\pi^0}} \frac{\mathrm{d}\sigma}{\mathrm{d}\Omega} = \frac{2}{3} \left(|A_0|^2 + 2p_{\pi^0}^2 \Re\{A_0^* A_2\} P_2(\cos \theta^*) + |C|^2 p_{\pi^0}^2 \sin^2 \theta^* \right), \qquad (7.2)$$

where A_0 is the s-wave amplitude, A_2 is the d-wave amplitude, and C is the p-wave amplitude. The momentum of the pion in the c.m. system is p_{π^0}, and the incident deuteron momentum in the c.m. system is p. In [110] formula 7.2 is obtained for the $\text{dd} \longrightarrow {}^4\text{He}\eta$ reaction, but it is also valid for the $dd \rightarrow {}^4\text{He}\pi^0$ reaction, since the J^{PC} quantum numbers (J – angular momentum, P – parity, C – charge conjugation) are the same for π^0 and η. Due to the presence of the identical particles in the initial state, odd and even partial waves do not interfere, and the angular distribution is symmetric with respect to $\cos \theta^* = 0$. Ordering the terms with respect to $\cos^2 \theta^*$, the differential cross section can be written as:

$$\frac{\mathrm{d}\sigma}{\mathrm{d}\Omega} = a + b \cos^2 \theta^*, \qquad (7.3)$$

where

$$a = \frac{p_{\pi^0}}{p} \frac{2}{3} \left(|A_0|^2 - p_{\pi^0}^2 \Re\{A_0^* A_2\} + |C|^2 p_{\pi^0}^2 \right), \qquad (7.4\text{a})$$

$$b = \frac{p_{\pi^0}}{p} \left(2p_{\pi^0}^2 \Re\{A_0^* A_2\} - \frac{2}{3} |C|^2 p_{\pi^0}^2 \right). \qquad (7.4\text{b})$$

The p-wave and $s-d$ interference terms contribute to the quadratic term and to the constant term. Even though from an unpolarized measurement one cannot directly disentangle the partial waves, some constraints can still be obtained. Any non-flat angular distribution is an indication of higher partial waves. The parameter b can be positive only if a d-wave contribution is present.

In Fig. 7.4 the angular distribution from the 1st and the 2nd part of the beamtime is fitted simultaneously with the function described in Eq. 7.3. For the fit the systematic and statistical uncertainties are added quadratically and presented in the plot.
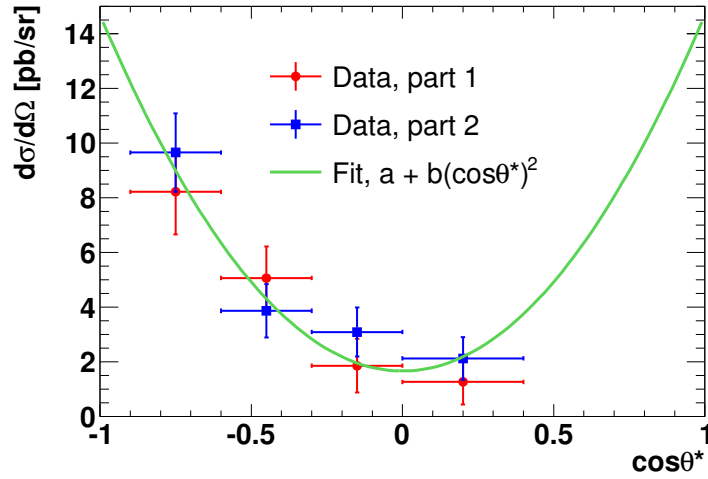
FIGURE 7.4: Differential cross section fitted simultaneously for the 1st and the 2nd part of the beamtime with the function $a + b\cos^2\theta^*$. The acceptance correction has been performed with the $dd \to {}^4\mathrm{He}\pi^0$ phase-space model. The obtained parameters a and b are presented in Eq. 7.5. The χ^2/NDF for the fit is 4.3/6. The parameters are used in the new $dd \to {}^4\mathrm{He}\pi^0$ generator. For the fit the systematic and statistical uncertainties are added quadratically.

The obtained values for a and b are:

$$a = (1.69 \pm 0.47) \text{ pb/sr}, \tag{7.5a}$$

$$b = (12.3 \pm 2.8) \text{ pb/sr}. \tag{7.5b}$$

These values (without the error) are used to set up an improved event generator.

7.2 Results with the New Event Generator

This section describes the final results obtained using the more realistic model including higher partial waves. The data from the 1st and the 2nd part of the beamtime have been fitted separately as described in Sec. 5.4, and the sum of both is presented in Fig. 7.5 and Fig. 7.6. The numbers of signal events extracted for every angular bin and every part of the beamtime are presented in Tab. 7.1.
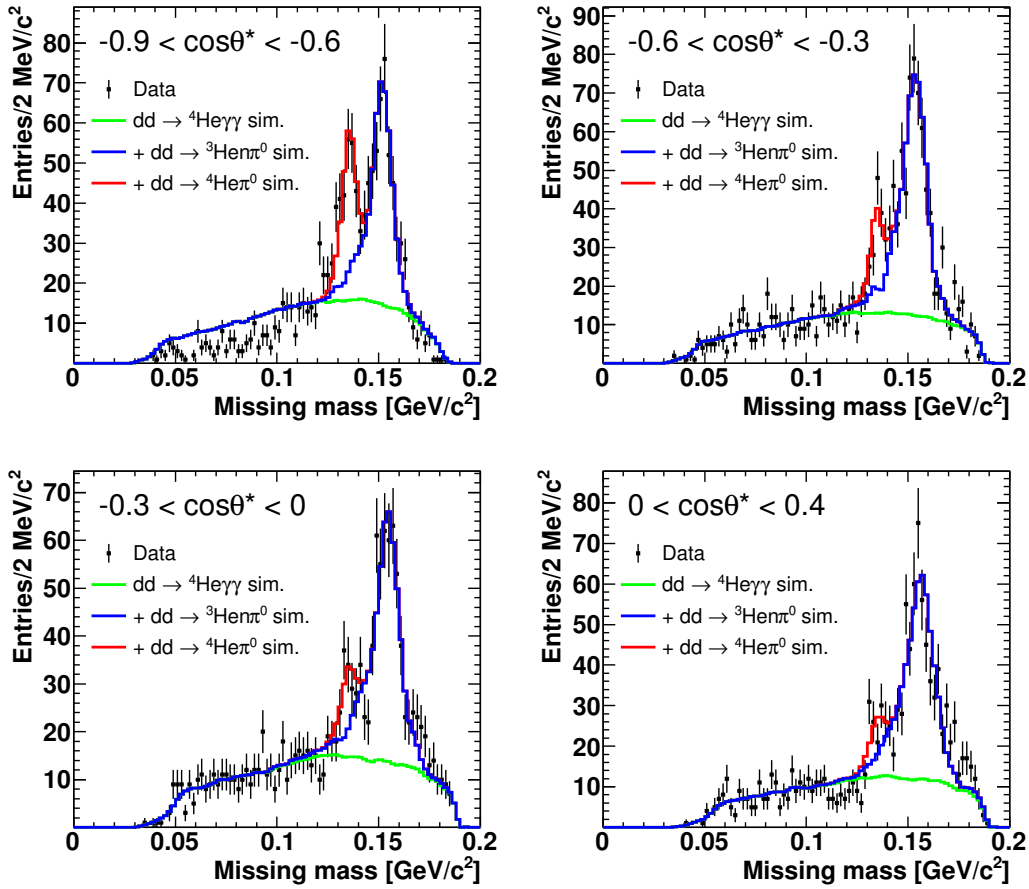
FIGURE 7.5: Missing mass for the $dd \rightarrow {}^4\text{He}X$ reaction for every angular bin for all data. The spectra are fitted with a linear combination of the simulated signal and background reactions: $dd \rightarrow {}^4\text{He}\gamma\gamma$ (green line), plus $dd \rightarrow {}^3\text{He}n\pi^0$ (blue line), plus $dd \rightarrow {}^4\text{He}\pi^0$ (red line).

TABLE 7.1: Number of signal events in every angular bin.

Bin number	Signal events [counts]	
	1st part	2nd part
1	63.2 ± 12	91.6 ± 13.5
2	45.2 ± 10.3	42.5 ± 10.7
3	17.6 ± 9.3	36 ± 10.3
4	12.9 ± 8.5	27.1 ± 9.9

In the ideal case of a perfect resolution, the acceptance times cut efficiencies as a function of $\cos\theta^*$ should be the same both for the phase space and the improved generator. However, in reality there is a migration between the angular bins: an event originating from one bin is measured in another one due to the limited detector resolution. The size of this effect depends on the shape of the angular distribution. In Fig. 7.7 the acceptance times cut efficiency as a function of $\cos\theta^*$ for both generators is presented. The final value of ϵ for every angular bin is shown in Tab. 7.2.
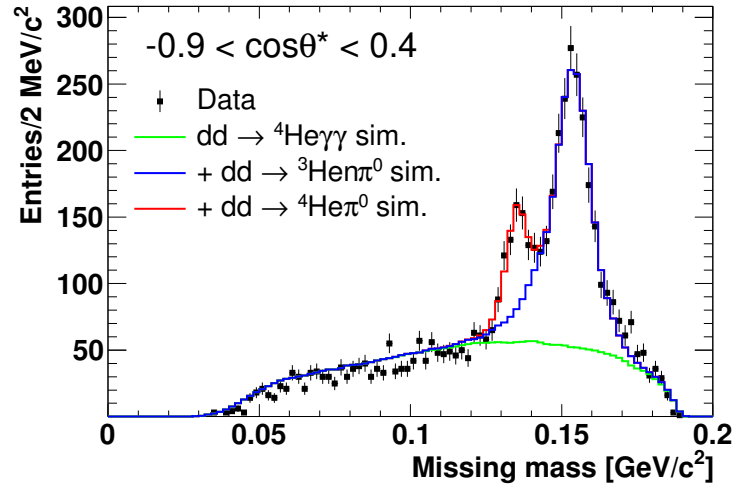
FIGURE 7.6: Missing mass for the $dd \rightarrow {}^4\text{He}X$ reaction for $-0.9 \leq \cos\theta^* \leq 0.4$ for all data. The fitted Monte Carlo template is the same as in Fig. 7.5.
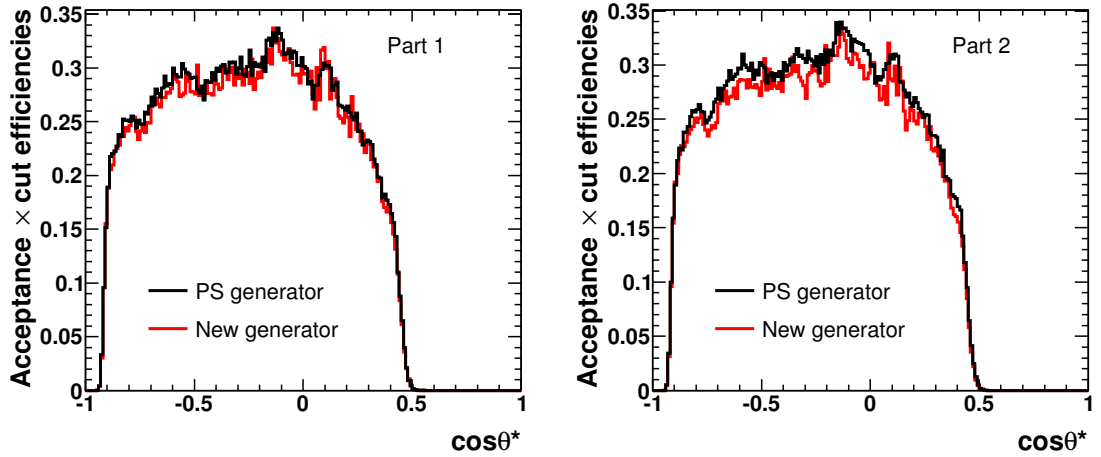
FIGURE 7.7: Comparison of the acceptance times cut efficiencies for the $dd \rightarrow {}^4\text{He}\pi^0$ reaction for the new (red line) and the old (black line) generator as a function of $\cos\theta^*$ for the 1st (left) and the 2nd (right) part of the beamtime.

TABLE 7.2: Signal acceptance times cut efficiencies for every angular bin for the 1st and the 2nd part of the beamtime.

Bin number	Acceptance times cut eff. [%]	
	1st part	2nd part
1	24.3	24.4
2	28.5	28.6
3	30.2	30.1
4	24.3	24.0

The differential cross section has been determined separately for the 1st and the 2nd part of the beamtime. The combined differential cross section $\frac{d\sigma}{d\Omega}_{\text{comb}}$ for every angular bin and for the whole angular range within detector acceptance has been obtained as a weighted average:

$$\frac{d\sigma}{d\Omega}_{\text{comb}} = \frac{\frac{1}{\sigma_1^2} \cdot \frac{d\sigma}{d\Omega}_1 + \frac{1}{\sigma_2^2} \cdot \frac{d\sigma}{d\Omega}_2}{\frac{1}{\sigma_1^2} + \frac{1}{\sigma_1^2}}, \tag{7.6}$$

where the weights are based on the statistical uncertainties of the differential cross sections for the particular $\cos\theta^*$ bin. The variance of the weighted mean is:

$$\sigma_{\text{comb}}^2 = \frac{1}{\sigma_1^{-2} + \sigma_2^{-2}}. \tag{7.7}$$

The final results are:

$$\frac{d\sigma}{d\Omega}\left(-0.9 \le \cos\theta^* < -0.6\right) = \left(9.4 \pm 1.1(\text{stat.})^{+0.5}_{-1.8}(\text{syst.})\right) \text{pb/sr}, \tag{7.8a}$$

$$\frac{d\sigma}{d\Omega}\left(-0.6 \le \cos\theta^* < -0.3\right) = \left(4.5 \pm 0.7(\text{stat.})^{+0.1}_{-1.7}(\text{syst.})\right) \text{pb/sr}, \tag{7.8b}$$

$$\frac{d\sigma}{d\Omega}\left(-0.3 \le \cos\theta^* < 0\right) = \left(2.64 \pm 0.69(\text{stat.})^{+0.25}_{-0.83}(\text{syst.})\right) \text{pb/sr}, \tag{7.8c}$$

$$\frac{d\sigma}{d\Omega}\left(0 \le \cos\theta^* \le 0.4\right) = \left(1.82 \pm 0.6(\text{stat.})^{+0.29}_{-0.62})(\text{syst.})\right) \text{pb/sr}. \tag{7.8d}$$

The systematic effects associated with this combined result have been checked by varying the cuts as in Sec. 7.1.1. Fig. 7.8 shows the differential cross sections for every angular bin together with their statistical and systematical uncertainties as presented in Eq. 7.8. In Fig. 7.9 the systematic uncertainties associated with every type of cut are shown for all four angular bins. For all cross sections there are two additional common systematic uncertainties originating in the luminosity determination: an uncertainty of 10% coming from the error of the $dd \rightarrow {}^3\text{He}n\pi^0$ cross section (marked as "norm.") and an uncertainty of 2.5% determined in Chapter 6 by varying the cuts used in the luminosity analysis (marked as "lumi. syst."). Integrating the differential results, the cross section σ_{acc} within the detector acceptance ($-0.9 \le \cos\theta^* \le 0.4$) equals to:

$$\sigma_{\text{acc}} = \left(36.1 \pm 3.2(\text{stat.})^{+0.1}_{-5.9}(\text{syst.}) \pm 3.7(\text{norm.}) \pm 0.9(\text{lumi. syst.})\right) \text{pb}. \tag{7.9}$$

To obtain the total cross section the angular distributions have been fitted simultaneously for both parts of the beamtime with the function from Eq. 7.3. Then, the function is integrated in the range from -1 to 1 and multiplied by 2π to obtain the total cross section.

Also for this result systematic effects are determined from the variation of the cuts. A separate angular distribution has been determined and fitted for each of these variations. In this way, also the systematical uncertainties for the parameters a and b describing the differential cross section are extracted. In Fig. 7.10 the total cross section
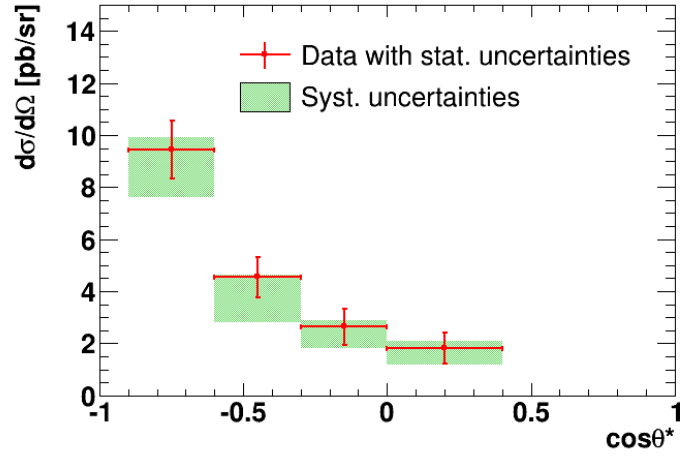
FIGURE 7.8: Differential cross sections for every angular bin. The sta-
tistical uncertainties are presented with a red line. The green area indi-
cates the systematic uncertainties.

and parameters a and b are presented for different cuts. Furthermore, the variation of
the fitted function to the angular distribution is shown. Every green curve shows the
fit for a varied cut. The reference fit for the set of cuts used in the analysis is drawn
with a dashed red curve. The individual contributions to the overall systematic un-
certainty of the total cross section and the parameters a and b have been added as
$\sqrt{\sum_i \sigma_i^2}$, where σ_i is the maximal deviation from the reference value for a single type
of cut.

In Fig. 7.11 the final angular distribution is presented. The obtained results are the
following:

$$a = \left(1.75 \pm 0.46(\text{stat.})^{+0.31}_{-0.8}(\text{syst.})\right) \text{pb/sr}\,, \tag{7.10a}$$

$$b = \left(13.6 \pm 2.2(\text{stat.})^{+0.9}_{-2.7}(\text{syst.})\right) \text{pb/sr}\,. \tag{7.10b}$$

$$\sigma_{\text{tot}} = \left(79.1 \pm 7.3(\text{stat.})^{+1.2}_{-10.5}(\text{syst.}) \pm 8.1(\text{norm.}) \pm 2.0(\text{lumi. syst.})\right) \text{pb}\,. \tag{7.11}$$

The systematic uncertainties connected to the variation of the cuts and the change in
the range of the missing mass fit are marked as "syst.". Both parameters a and b have
common systematic uncertainties of 10% from external normalization and 2% from
luminosity determination.

Fig. 7.11 shows that the angular distribution is not measured in the whole range of
$\cos\theta^*$. This is linked to the drop in acceptance (see Fig. 7.7) caused by two effects: the
^{4}He particles escaping through the hole for the beam pipe (forward and backward go-
ing particles in c.m.) and very slow ^{4}He particles ($E_{kin} \lesssim 0.15\,\text{MeV}$) not reaching the
FVH layer (affecting the acceptance above $\cos\theta^* = 0.5$). However, as the angular dis-
tribution has to be symmetric with respect to $\cos\theta^* = 0$, the reconstructed differential
cross section in the range $-0.5 < \cos\theta^* < 0$ is sufficient to describe the result.
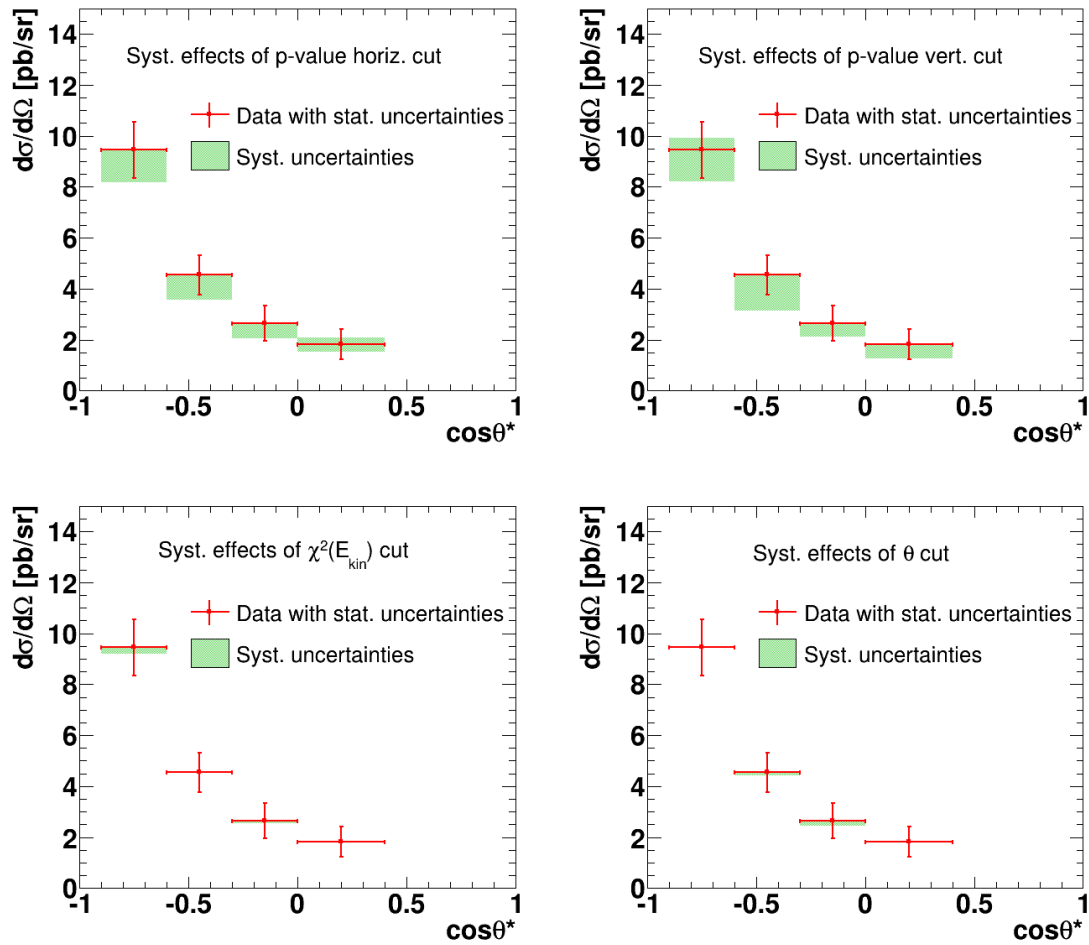
FIGURE 7.9: Systematic uncertainties for the combined differential cross sections for every angular bin. The variation of every cut applied in the analysis has been checked, i.e, the horizontal and vertical p-value cut, the χ^2 cut from the E_{kin} reconstruction procedure and the polar angle cut. The red points represent the combined differential cross section with the statistical uncertainties, and the green area shows the systematic uncertainties.
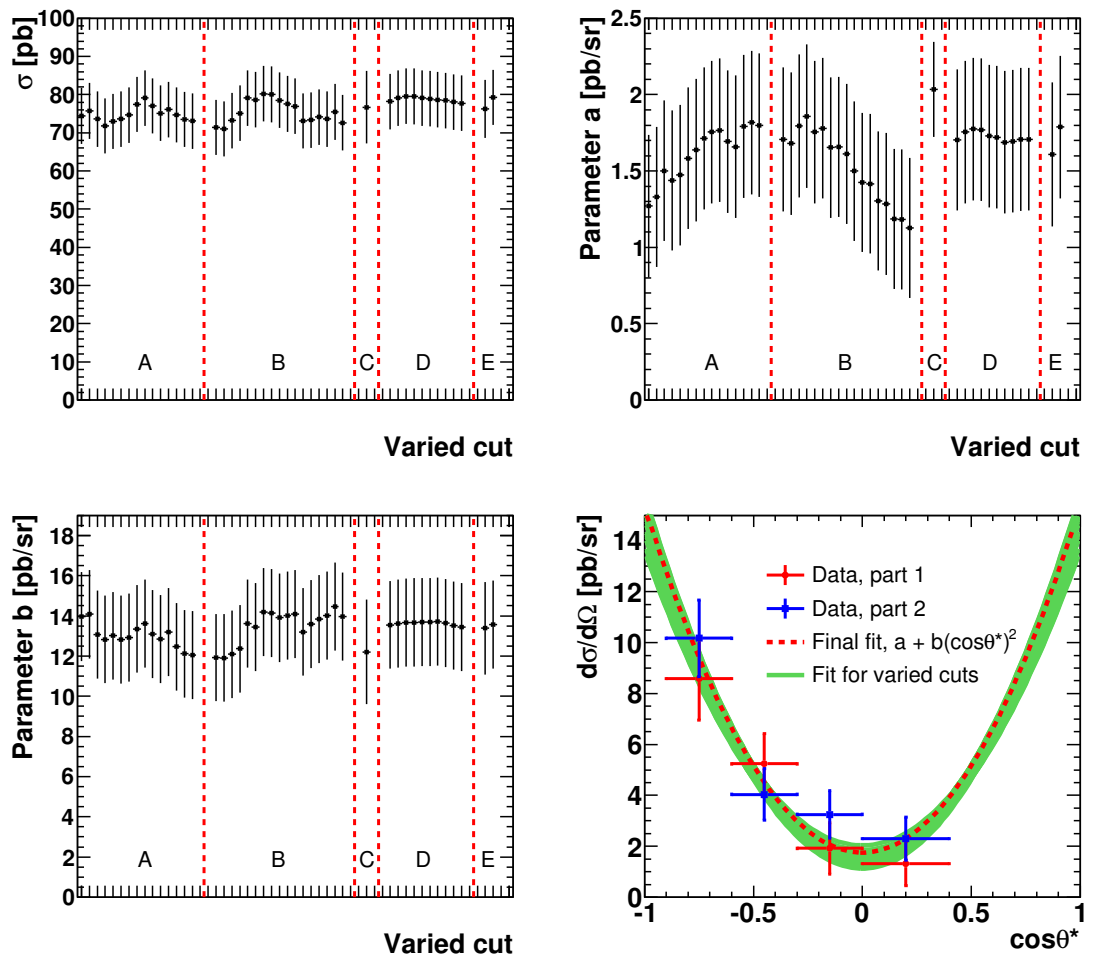
FIGURE 7.10: Check of the systematic effects on the total cross section and the fit parameters of the angular distribution. The total cross section σ, and the parameters a and b of the angular distribution fit, $a + b \cos^2 \theta^*$, are presented as a function of the cut variation, where A is the variation of the horizontal p-value cut (see Fig. 5.10), B is the variation of the vertical p-value cut (see Fig. 5.10), C refers to the change in the range of the missing mass fit (see Fig. 7.2), D is the variation of the χ^2 cut from the E_{kin} reconstruction, E refers to the change in the polar angle cut. The bottom right plot shows the angular distribution from the 1st (red points) and the 2nd (blue points) part of the beamtime, with parabolic functions fitted simultaneously for the cuts used in the analysis (red dashed curve) and for all cut variations (green solid curves).
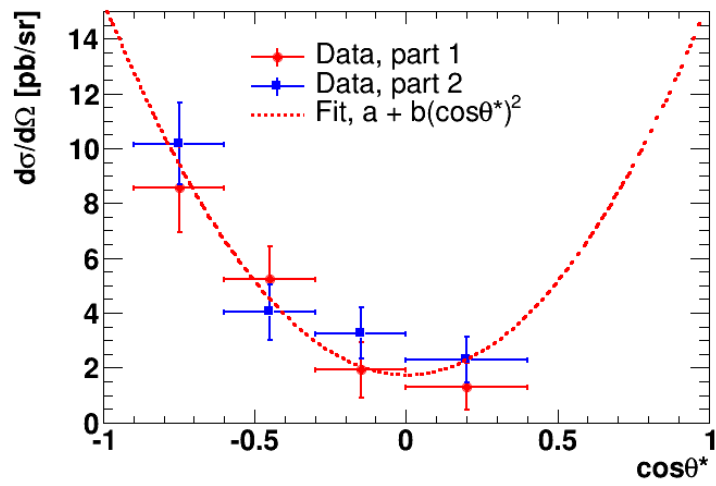
FIGURE 7.11: Final angular distribution. The data points from the 1st part of the beamtime are marked in red and from the 2nd one in blue. The result of the simultaneous fit is shown with a red dashed curve. In the plot only the statistical uncertainties are presented. The obtained parameters a and b are presented in Eq. 7.10. The χ^2/NDF for the fit is 4.2/6.

Chapter 8

Discussion and Outlook

A sample of 336 ± 43 event candidates of the $dd \to {}^4\text{He}\pi^0$ reaction has been extracted using a data set from an eight-week long beamtime with the WASA-at-COSY experiment. The total and differential cross sections have been determined. Following a theoretical description of the shape of the angular distribution as presented in [110], the differential cross section has been fitted with the function $d\sigma/d\Omega = a + b\cos^2\theta^*$. The obtained fit parameters are:

$$a = \left(1.75 \pm 0.46(\text{stat.})^{+0.31}_{-0.8}(\text{syst.})\right) \text{pb}/\text{sr}, \tag{8.1a}$$

$$b = \left(13.6 \pm 2.2(\text{stat.})^{+0.9}_{-2.7}(\text{syst.})\right) \text{pb}/\text{sr}. \tag{8.1b}$$

Both parameters have common systematic uncertainties of 10% from external normalization and 2% from luminosity determination. The total cross section has been obtained as the integral over $\cos\theta^*$ from the presented fit of the angular distribution:

$$\sigma_{\text{tot}} = \left(79.1 \pm 7.3(\text{stat.})^{+1.2}_{-10.5}(\text{syst.}) \pm 8.1(\text{norm.}) \pm 2.0(\text{lumi. syst.})\right) \text{pb}. \tag{8.2}$$

The statistical uncertainties for the parameters a and b as well as for the total cross section are of similar size as the systematical effects estimated by the variation of the selection cuts and the uncertainty of the luminosity determination.

In the previous measurement with WASA-at-COSY these cross sections have also been determined, however with lower statistics [53] (see Sec. 2.2.3). In Fig. 8.1 the results from this thesis (red points) and the previous measurement (black points) are compared. The presented differential cross section from this thesis is the combined result from the two parts of the beamtime using a weighted average with statistical weights, as shown in Eq. 7.6. The error bars indicate the statistical uncertainties, while the systematical uncertainties are marked in green. The red dashed curve represents the final fit of the angular distribution obtained simultaneously for both parts of the beamtime. The error bars of the points from the previous measurement include only the statistical uncertainties - only in the first bin an additional systematic uncertainty is added (see [53]). From this comparison one can see that the tendency of the shape of the differential cross section has been confirmed by this measurement. However, the current measurement is slightly below the previous result: for the first and second

bin the agreement is below one standard deviation of presented uncertainties, for the third and fourth bin it is about 2 standard deviations.
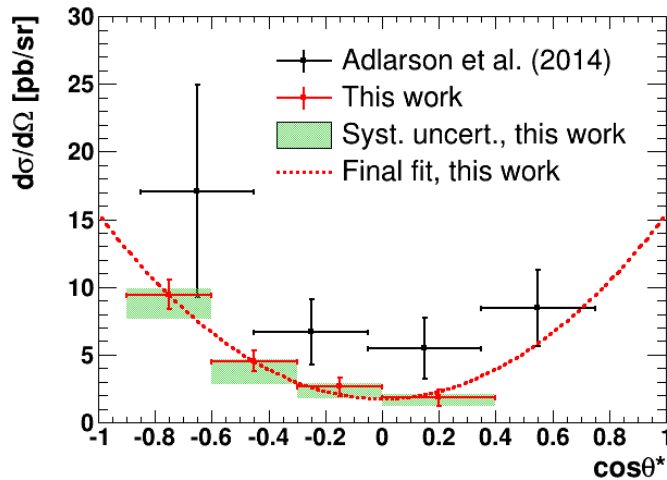
FIGURE 8.1: Comparison between the angular distribution obtained in this thesis (red points) and the previous WASA measurement of $dd \to {}^{4}\mathrm{He}\pi^{0}$ (black points). The error bars of the data points from this thesis show the statistical uncertainties. The systematical uncertainties are marked in green. The red dashed curve represents the final fit of the angular distribution obtained simultaneously for both parts of the beamtime. The error bars of the points from the previous measurement show the statistical uncertainties only, except for the 1st bin where an additional systematic uncertainty is added.

To compare the total cross sections, the fit of the angular distribution from [53] containing higher partial waves ($a + b\cos^2\theta^*$) has been integrated in the range of $-1 < \cos\theta^* < 1$. The obtained result is:

$$\sigma_{\mathrm{tot}}^{\mathrm{prev}} = (123 \pm 30(\mathrm{stat.}) \pm 12(\mathrm{norm.}) \pm 8.6(\mathrm{ext.}))\,\mathrm{pb}\,, \tag{8.3}$$

where "norm." stands for the systematic error of the luminosity determination and "ext." for the error from the normalization to external data. The agreement between this result and the cross section obtained in the thesis is at the level of one standard deviation of the presented uncertainties.

8.1 Common Interpretation with the Other Measurements

From an unpolarized measurement, the different partial waves cannot be directly disentangled, as both p-wave and $s-d$ interference terms contribute to the quadratic term and to the constant term. However, some constraints can be obtained. First of all, any non-flat angular distribution is an indication of higher partial waves. The obtained result shows that the parameter b of the angular distribution significantly differs from

zero. The positive value for the parameter b indicates that a d-wave contribution is essential for interpreting the data (see Eq. 7.4b).

Further conclusions can be drawn when adding the information from the measurement close to threshold [52]. Fig. 8.2 shows the energy dependence of $\frac{p}{p_{\pi^0}}\sigma_{\text{tot}}$ which describes the reaction amplitudes as defined in [110]. The previous experiment with WASA-at-COSY is also included.
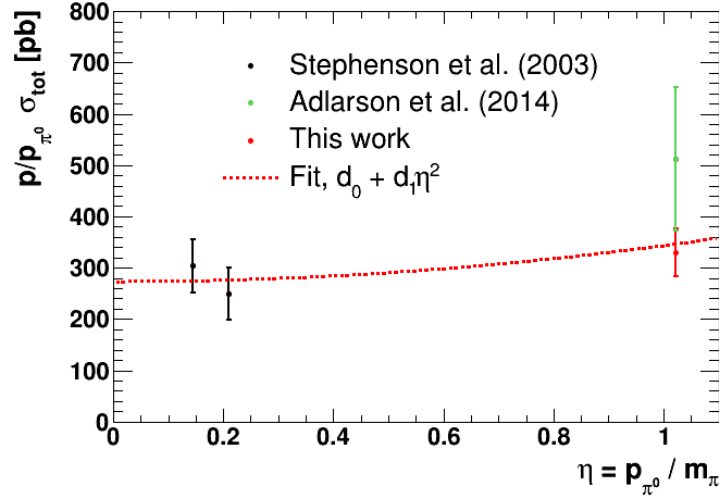
FIGURE 8.2: World data on the unpolarised $dd \rightarrow {}^4\text{He}\pi^0$ total cross section. $\frac{p}{p_{\pi^0}}\sigma_{\text{tot}}$ is shown as a function of $\eta = p_{\pi^0}/m_{\pi^0}$. The red curve indicates the $d_0 + d_1\eta^2$ fit, from which the magnitude of the s-wave and p-wave can be directly obtained like in Eq. 8.5 assuming the absence of initial- and final-state interactions and energy dependence of partial wave amplitudes. The black points show the results from [52], the green point indicates the previous WASA measurement [53] and the red point shows the result from this thesis.

As shown in Sec. 7.1.2, to order $p_{\pi^0}^2$, only three partial wave amplitudes contribute to the unpolarised cross section: s–wave (A_0), p-wave (C) and d-wave (A_2). An anisotropy in the differential cross section can be caused by either p–wave or an $s-d$ interference:

$$\frac{p}{p_{\pi^0}}\frac{\mathrm{d}\sigma}{\mathrm{d}\Omega} = \frac{2}{3}\left(|A_0|^2 + 2p_{\pi^0}^2\Re\{A_0^*A_2\}P_2(\cos\theta^*) + |C|^2 p_{\pi^0}^2\sin^2\theta^*\right) , \qquad (8.4)$$

where p_{π^0} is the momentum of pion in the c.m. system and p is the momentum in the c.m. system of the incident deutron. Integrating this equation over $d\Omega$ we obtain the formula describing the connection between the total cross section and the reaction amplitudes:

$$\frac{p}{p_{\pi^0}}\sigma_{\text{tot}} = \frac{8\pi}{3}|A_0|^2 + \frac{16\pi}{9}m_{\pi^0}^2|C|^2\eta^2 , \qquad (8.5)$$

where $\eta = p_{\pi^0}/m_{\pi^0}$. As the interference term does not contribute to the total cross section, fitting $\frac{p}{p_{\pi^0}}\sigma_{\text{tot}}(\eta)$ with a function of the form $d_0 + d_1\eta^2$ one can directly obtain the square of the magnitude of the s-wave and p-wave amplitudes. However, one has

to keep in mind that the energy dependence of the partial wave amplitudes and the formation of the ^{4}He in the final state are not included here which also might have an influence. The fit is presented in Fig. 8.2 as a red curve. The obtained values are:

$$|A_0|^2 = (32.7 \pm 4.5) \ \text{pb/sr} \,, \tag{8.6a}$$

$$|C|^2 = (690 \pm 560) \ \text{pb/} \left(\text{sr} \cdot (\text{GeV}/c)^2\right) . \tag{8.6b}$$

With the present status of the $dd \rightarrow {}^4\text{He}\pi^0$ measurements, $|C|^2$ obtained from the fit has a large uncertainty. On the other hand, the value of $|A_0|^2$ can be well determined, since it is mostly constrained by the first two points in Fig. 8.2 describing the measurement close to threshold, where s-wave is dominating.

Taking this value of $|A_0|^2$ and fixing it in the fit of the angular distribution determined in this thesis, one can obtain $|C|^2$ and also $\Re\{A_0^*A_2\}$:

$$\frac{p}{p_{\pi^0}}\frac{\mathrm{d}\sigma}{\mathrm{d}\Omega} = \frac{2}{3}\left(|A_0|^2_{\text{fixed}} - p_{\pi^0}^2\Re\{A_0^*A_2\} + |C|^2 p_{\pi^0}^2\right) + \left(2p_{\pi^0}^2\Re\{A_0^*A_2\} - \frac{2}{3}|C|^2 p_{\pi^0}^2\right)\cos^2\theta^*. \tag{8.7}$$

The refitted angular distribution with the fixed $|A_0|^2$ is presented in Fig. 8.3.
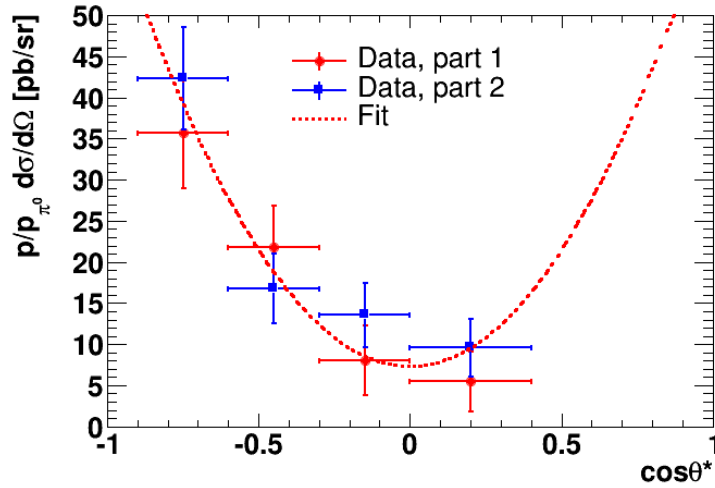
FIGURE 8.3: Fit of the angular distribution with the fixed s-wave contribution from the world data. The data points from the 1st part of the beamtime are marked in red and from the 2nd one in blue. The result of the simultaneous fit is shown with a red dashed curve. The obtained $|C|^2$ and $\Re\{A_0^*A_2\}$ parameters are presented in Eq. 8.8. The χ^2/NDF for the fit is 4.2/6.

The obtained values of $|C|^2$ and $\Re\{A_0^*A_2\}$ are:

$$\Re\{A_0^*A_2\} = \left(1670 \pm 320(\text{stat.})^{+80}_{-430}(\text{syst.})\right) \text{pb/} \left(\text{sr} \cdot (\text{GeV}/c)^2\right), \tag{8.8a}$$

$$|C|^2 = \left(520 \pm 290(\text{stat.})^{+50}_{-430}(\text{syst.})\right) \text{pb/} \left(\text{sr} \cdot (\text{GeV}/c)^2\right). \tag{8.8b}$$

The systematical uncertainties obtained by the variation of the selection cuts and the change in the range of the missing mass fit are marked as "syst.".

The parameters $|C|^2$ and $\Re\{A_0^* A_2\}$ are strongly correlated, with a correlation coefficient of 0.87. Therefore, a proper presentation has to account for this correlation. Fig. 8.4 shows a correlation plot with the confidence regions for both variables. The center point marked with a cross shows the best-fit values. The contours correspond to the 68.3%, 90%, 95% and 99% confidence regions. The plot shows only $|C|^2 > 0$, since the square of the magnitude of the amplitude is not allowed to be negative.

In addition, the central values for $|C|^2$ and $\Re\{A_0^* A_2\}$ are also affected by the overall systematic uncertainties for luminosity (described as "lumi.") and the fixed value for $|A_0|^2$ (marked as "fix."). Both cause a correlated displacement of the center of the ellipses shown in Fig. 8.4. Taking into account the fact that they are correlated, the individual systematic uncertainties are:

$$\Delta\left(\Re\{A_0^* A_2\}\right)_{\text{fix}} = \pm 120 \, \text{pb}/\left(\text{sr} \cdot (\text{GeV}/c)^2\right), \qquad \Delta\left(|C|^2\right)_{\text{fix}} = \pm 350 \, \text{pb}/\left(\text{sr} \cdot (\text{GeV}/c)^2\right),$$
$$\Delta\left(\Re\{A_0^* A_2\}\right)_{\text{lumi}} = \pm 260 \, \text{pb}/\left(\text{sr} \cdot (\text{GeV}/c)^2\right), \qquad \Delta\left(|C|^2\right)_{\text{lumi}} = \pm 320 \, \text{pb}/\left(\text{sr} \cdot (\text{GeV}/c)^2\right).$$

In Fig. 8.4 the possible systematic shifts of the center of the ellipses due to these effects are marked with red (lumi.) and blue (fix.) lines. These lines correspond to a displacement of $\pm\Delta$.
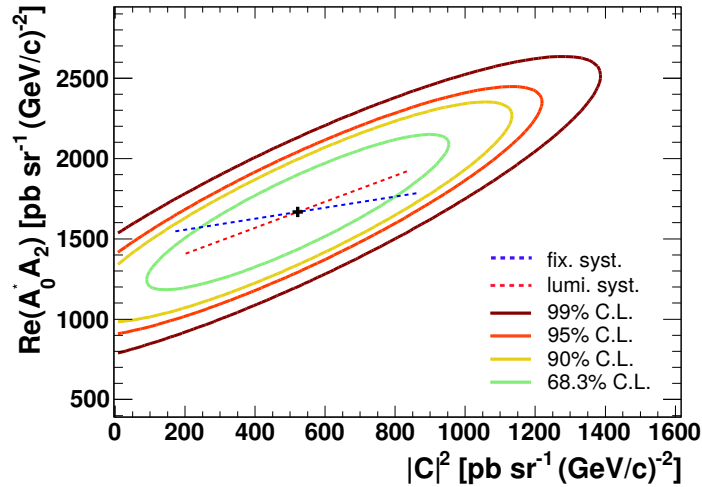
FIGURE 8.4: Correlation plot with the confidence regions for the parameters $|C|^2$ and $\Re\{A_0^* A_2\}$. The center point marked with the cross shows the best-fit values. The contours corresponding to the 68.3%, 90%, 95% and 99% confidence regions for normally distributed data are shown. The red and blue lines show the systematic shift of the ellipses due to the overall systematic uncertainties for luminosity (lumi.) and the fixed value for $|A_0|^2$ (fix.), respectively.

8.2 Future Plans

Besides statistics, the uncertainties of $\Re\{A_0^* A_2\}$ and $|C|^2$ have their main origin in the systematic effects from the selection cuts and the missing mass fit. A possible improvement may be achieved by including the energy loss information from the Forward Veto Hodoscope.

Using the correlation between the energy loss in the FVH and the time-of-flight an additional selection cut can be defined. According to earlier feasibility studies [73], this can further reduce the $dd \to {}^3\mathrm{He}n\pi^0$ background and even remove it completely. It may allow to verify more advanced models of the double radiative capture and reduce the mismatch in the missing mass range below $0.11\,\mathrm{GeV}/c^2$ in the most backward angular bin of $dd \to {}^4\mathrm{He}\pi^0$. Applying only the ToF-dE(FVH) correlation cut and releasing the p-value cut from the kinematic fit, the statistics of the $dd \to {}^4\mathrm{He}\pi^0$ events could possibly be increased by a factor of two, while the background from $dd \to {}^3\mathrm{He}n\pi^0$ could still be effectively reduced.

The improvement, however, strongly depends on the resolution of the energy information from the FVH, which has not been used in any WASA experiment so far. Therefore, a precise and thorough energy calibration of the plastic scintillator bars of FVH with two sided readout is required.

8.3 Final Conclusions

This measurement of the charge symmetry breaking $dd \to {}^4\mathrm{He}\pi^0$ reaction at an excess energy of 60 MeV shows the necessity to include higher partial waves in the theoretical calculations. Already the energy dependence of the total cross section of the world data set for the unpolarised measurement of $dd \to {}^4\mathrm{He}\pi^0$ suggests the presence of higher partial waves. After fixing the square of the magnitude of the s-wave amplitude $|A_0|^2$ from the fit of this dependence, the square of the magnitude of the p-wave amplitude $|C|^2$ and the real part of the $s-d$ interference term $\Re\{A_0^* A_2\}$ have been determined assuming that only terms to order $p_{\pi^0}^2$ contribute to the reaction amplitudes.

The obtained $s-d$ interference term $\Re\{A_0^* A_2\}$ is significantly different from zero (about three standard deviations). In comparison to $\Re\{A_0^* A_2\}$ the square of the magnitude of the p-wave amplitude is small and consistent with zero within uncertainties.

The d-wave contribution manifests itself predominantly in the interference term $\Re\{A_0^* A_2\}$ of the differential cross section. The direct contribution via the $|A_2|^2$ term in the total cross section or the $\cos^4 \theta^*$ term in the differential distribution is of the order of $p_{\pi^0}^4$ and, therefore, is suppressed by the factor $1/p_{\pi^0}^2 \approx 50$ at $\varepsilon = 60$ MeV.

The parameter-free prediction of the p-wave contribution, which can be calculated within chiral perturbation theory in leading and next-to-leading order, should give a value compatible with the measurement. However, since the differential cross section is dominated by the interference term $\Re\{A_0^* A_2\}$, any attempt to fully describe the reaction has to include also d-wave contributions.

Bibliography

[1] *Standard Model of Elementary Particles*, URL: `https://commons.wikimedia.org/wiki/File:Standard_Model_of_Elementary_Particles.svg` (visited on 08/13/2016).

[2] K. A. Olive *et al.* (Particle Data Group), *Review of Particle Physics*, Chin. Phys. C38, 090001 (2014), DOI: `10.1088/1674-1137/38/9/090001`.

[3] A. Bettini, *Introduction to Elementary Particle Physics*, Cambridge University Press, 2014, ISBN: 9781107783140.

[4] D. Perkins, *Introduction to High Energy Physics*, Cambridge University Press, 2000, ISBN: 9781139643375.

[5] C. Quigg, *Gauge Theories of the Strong, Weak, and Electromagnetic Interactions: Second Edition*, Princeton University Press, 2013, ISBN: 9781400848225.

[6] E. Zeidler, *Quantum Field Theory*, Quantum Field Theory, Springer Berlin Heidelberg, 2008, ISBN: 9783540853770.

[7] K. Abe *et al.* (VENUS), *Determination of the QCD scale parameter Lambda (ms) with QCD cascade on the basis of the next-to-leading logarithmic approximation*, Phys. Lett. B240, 232–236 (1990), DOI: `10.1016/0370-2693(90)90440-H`.

[8] R. C. Group, *Measurement of the inclusive jet cross section using the midpoint algorithm in run II at the collider detector at Fermilab (CDF)*, PhD thesis, University of Florida, 2006.

[9] S. Chatrchyan *et al.* (CMS), *Observation of a new boson at a mass of 125 GeV with the CMS experiment at the LHC*, Phys. Lett. B716, 30–61 (2012), DOI: `10.1016/j.physletb.2012.08.021`.

[10] G. Aad *et al.* (ATLAS), *Observation of a new particle in the search for the Standard Model Higgs boson with the ATLAS detector at the LHC*, Phys. Lett. B716, 1–29 (2012), DOI: `10.1016/j.physletb.2012.08.020`.

[11] F. Englert and R. Brout, *Broken Symmetry and the Mass of Gauge Vector Mesons*, Phys. Rev. Lett. 13, 321–323 (1964), DOI: `10.1103/PhysRevLett.13.321`.

[12] P. W. Higgs, *Broken symmetries, massless particles and gauge fields*, Phys. Lett. 12, 132–133 (1964), DOI: `10.1016/0031-9163(64)91136-9`.

[13] P. W. Higgs, *Broken Symmetries and the Masses of Gauge Bosons*, Phys. Rev. Lett. 13, 508–509 (1964), DOI: `10.1103/PhysRevLett.13.508`.

[14] G. S. Guralnik, C. R. Hagen, and T. W. B. Kibble, *Global Conservation Laws and Massless Particles*, Phys. Rev. Lett. 13, 585–587 (1964), DOI: `10.1103/PhysRevLett.13.585`.

[15] P. W. Higgs, *Spontaneous Symmetry Breakdown without Massless Bosons*, Phys. Rev. 145, 1156–1163 (1966), DOI: `10.1103/PhysRev.145.1156`.

[16] F. Wilczek, *Mass Without Mass I: Most of Matter*, Physics Today 52, 11–13 (1999), DOI: `http://dx.doi.org/10.1063/1.882879`.

[17] F. Wilczek, *Origins of Mass*, Central Eur. J. Phys. 10, 1021–1037 (2012), DOI: `10.2478/s11534-012-0121-0`.

[18] D. Gross, M. Henneaux, and A. Sevrin, eds., *Proceedings, 25th Solvay Conference on Physics: The Theory of the Quantum World*, World Scientific, Hackensack, USA: World Scientific, 2013, ISBN: 9789814440615.

[19] J. F. Donoghue, E. Golowich, and B. R. Holstein, *Dynamics of the Standard Model*, Cambridge Books Online, Cambridge University Press, 1992, ISBN: 9780511524370.

[20] A. Manohar and H. Georgi, *Chiral Quarks and the Nonrelativistic Quark Model*, Nucl. Phys. B234, 189–212 (1984), DOI: `10.1016/0550-3213(84)90231-1`.

[21] J. Goldstone, A. Salam, and S. Weinberg, *Broken Symmetries*, Phys. Rev. 127, 965–970 (1962), DOI: `10.1103/PhysRev.127.965`.

[22] M. Gell-Mann, R. J. Oakes, and B. Renner, *Behavior of current divergences under SU(3) x SU(3)*, Phys. Rev. 175, 2195–2199 (1968), DOI: `10.1103/PhysRev.175.2195`.

[23] J. Pivarski, *The Origin of Mass*, https://cornellmath.wordpress.com/2007/07/25/the-origin-of-mass, Blog, 2007.

[24] J. Gasser and H. Leutwyler, *Chiral Perturbation Theory to One Loop*, Annals Phys. 158, 142 (1984), DOI: `10.1016/0003-4916(84)90242-2`.

[25] S. Weinberg, *Phenomenological Lagrangians*, Physica A96, 327–340 (1979), DOI: `10.1016/0378-4371(79)90223-1`.

[26] H. Leutwyler, *On the foundations of chiral perturbation theory*, Annals Phys. 235, 165–203 (1994), DOI: `10.1006/aphy.1994.1094`.

[27] A. Pich, *Chiral perturbation theory*, Rept. Prog. Phys. 58, 563–610 (1995), DOI: `10.1088/0034-4885/58/6/001`.

[28] B. Borasoy, *Introduction to Chiral Perturbation Theory*, Springer Proc. Phys. 118, 1–26 (2008), DOI: `10.1007/978-3-540-73621-9_1`.

[29] M. A. Shifman, A. I. Vainshtein, and V. I. Zakharov, *QCD and Resonance Physics. Theoretical Foundations*, Nucl. Phys. B147, 385–447 (1979), DOI: `10.1016/0550-3213(79)90022-1`.

[30] C. G. Callan Jr. *et al.*, *Structure of phenomenological Lagrangians. 2.*, Phys. Rev. 177, 2247–2250 (1969), DOI: `10.1103/PhysRev.177.2247`.

[31] S. R. Coleman, J. Wess, and B. Zumino, *Structure of phenomenological Lagrangians. 1.*, Phys. Rev. 177, 2239–2247 (1969), DOI: `10.1103/PhysRev.177.2239`.

[32] C. Hanhart, *Meson production in nucleon–nucleon collisions close to the threshold*, Physics Reports 397, 155 –256 (2004), DOI: `http://dx.doi.org/10.1016/j.physrep.2004.03.007`.

[33] S. Weinberg, *Pion scattering lengths*, Phys. Rev. Lett. 17, 616–621 (1966), DOI: `10.1103/PhysRevLett.17.616`.

[34] Y. Tomozawa, *Axial vector coupling renormalization and the meson baryon scattering lengths*, Nuovo Cim. A46, 707–717 (1966), DOI: `10.1007/BF02857517`.

[35] J. Chadwick, *Possible Existence of a Neutron*, Nature 129, 312 (1932), DOI: `10.1038/129312a0`.

[36] S. Weinberg, *The Problem of Mass*, Trans. New York Acad. Sci. 38, 185–201 (1977), DOI: `10.1111/j.2164-0947.1977.tb02958.x`.

[37] J. Gasser and H. Leutwyler, *Quark Masses*, Phys. Rept. 87, 77–169 (1982), DOI: `10.1016/0370-1573(82)90035-7`.

[38] W. N. Cottingham, *The neutron proton mass difference and electron scattering experiments*, Annals Phys. 25, 424–432 (1963), DOI: `10.1016/0003-4916(63)90023-X`.

[39] A. Walker-Loud, C. E. Carlson, and G. A. Miller, *The Electromagnetic Self-Energy Contribution to $M_p - M_n$ and the Isovector Nucleon Magnetic Polarizability*, Phys. Rev. Lett. 108, 232301 (2012), DOI: `10.1103/PhysRevLett.108.232301`.

[40] S. Borsanyi *et al.*, *Ab initio calculation of the neutron-proton mass difference*, Science 347, 1452–1455 (2015), DOI: `10.1126/science.1257050`.

[41] V. Bernard, B. Kubis, and U.-G. Meissner, *The Fubini-Furlan-Rosetti sum rule and related aspects in light of covariant baryon chiral perturbation theory*, Eur. Phys. J. A25, 419–425 (2005), DOI: `10.1140/epja/i2005-10144-9`.

[42] G. A. Miller, B. M. K. Nefkens, and I. Slaus, *Charge symmetry, quarks and mesons*, Phys. Rept. 194, 1–116 (1990), DOI: `10.1016/0370-1573(90)90102-8`.

[43] G. A. Miller, A. K. Opper, and E. J. Stephenson, *Charge symmetry breaking and QCD*, Ann. Rev. Nucl. Part. Sci. 56, 253–292 (2006), DOI: `10.1146/annurev.nucl.56.080805.140446`.

[44] S. E. Vigdor *et al.*, *Charge symmetry breaking in n (polarized) p (polarized) scattering at 183-MeV*, Phys. Rev. C46, 410–448 (1992), DOI: `10.1103/PhysRevC.46.410`.

[45] L. M. Barkov *et al.*, *Electromagnetic Pion Form-Factor in the Timelike Region*, Nucl. Phys. B256, 365–384 (1985), DOI: `10.1016/0550-3213(85)90399-2`.

[46] S. A. Coon and M. D. Scadron, *Universality of $\Delta(I) = 1$ meson mixing and charge symmetry breaking*, Phys. Rev. C51, 2923–2931 (1995), DOI: `10.1103/PhysRevC.51.2923`.

[47] J. A. Nolen Jr. and J. P. Schiffer, *Coulomb energies*, Ann. Rev. Nucl. Part. Sci. 19, 471–526 (1969), DOI: `10.1146/annurev.ns.19.120169.002351`.

[48] O. Dumbrajs *et al.*, *Compilation of Coupling Constants and Low-Energy Parameters. 1982 Edition*, Nucl. Phys. B216, 277–335 (1983), DOI: `10.1016/0550-3213(83)90288-2`.

[49] U. van Kolck, J. A. Niskanen, and G. A. Miller, *Charge symmetry violation in $pn \to d\pi^0$ as a test of chiral effective field theory*, Phys. Lett. B493, 65–72 (2000), DOI: `10.1016/S0370-2693(00)01133-3`.

[50] D. R. Bolton and G. A. Miller, *Charge Symmetry Breaking in the $pn \to d\pi^0$ reaction*, Phys. Rev. C81, 014001 (2010), DOI: `10.1103/PhysRevC.81.014001`.

[51] A. K. Opper *et al.*, *Charge symmetry breaking in $pn \to d\pi^0$*, Phys. Rev. Lett. 91, 212302 (2003), DOI: `10.1103/PhysRevLett.91.212302`.

[52] E. J. Stephenson *et al.*, *Observation of the charge symmetry breaking $d + d \to {}^4He + \pi^0$ reaction near threshold*, Phys. Rev. Lett. 91, 142302 (2003), DOI: `10.1103/PhysRevLett.91.142302`.

[53] P. Adlarson *et al.* (WASA-at-COSY), *Charge symmetry breaking in $dd \to {}^4He\pi^0$ with WASA-at-COSY*, Phys. Lett. B739, 44–49 (2014), DOI: `10.1016/j.physletb.2014.10.029`.

[54] J. A. Niskanen, *Isospin breaking in the reaction $pn \to d\pi^0$ at threshold*, Few Body Syst. 26, 241–249 (1999), DOI: `10.1007/s006010050117`.

[55] V. Lensky *et al.*, *Towards a field theoretic understanding of $NN \to NN\pi$*, Eur. Phys. J. A27, 37–45 (2006), DOI: `10.1140/epja/i2006-10002-4`.

[56] V. Baru *et al.*, *p-wave pion production from nucleon-nucleon collisions*, Phys. Rev. C 80, 044003 (2009), DOI: `10.1103/PhysRevC.80.044003`.

[57] A. Filin *et al.*, *Extraction of the strong neutron-proton mass difference from the charge symmetry breaking in $pn \to d\pi^0$*, Phys. Lett. B681, 423–427 (2009), DOI: `10.1016/j.physletb.2009.10.069`.

[58] A. Gardestig *et al.*, *Survey of charge symmetry breaking operators for $dd \to \alpha\pi^0$*, Phys. Rev. C69, 044606 (2004), DOI: `10.1103/PhysRevC.69.044606`.

[59] A. Nogga *et al.*, *Realistic few-body physics in the $dd \to \alpha\pi^0$ reaction*, Phys. Lett. B639, 465–470 (2006), DOI: `10.1016/j.physletb.2006.04.058`.

[60] T. A. Lahde and G. A. Miller, *Initial-state Coulomb interaction in the $dd \to \alpha\pi^0$ reaction*, Phys. Rev. C75, 055204 (2007), DOI: `10.1103/PhysRevC.75.055204`.

[61] A. C. Fonseca, R. Machleidt, and G. A. Miller, *Nucleon-nucleon charge symmetry breaking and the $dd \to \alpha\pi^0$ reaction*, Phys. Rev. C80, 027001 (2009), DOI: `10.1103/PhysRevC.80.027001`.

[62] *WASA-at-COSY Collaboration, Charge Symmetry Breaking in $dd \rightarrow {}^4He\pi^0$*, COSY Proposal No. 173, 2007.

[63] P. Podkopal, *Investigations of the reaction $dd \rightarrow {}^3Hen\pi^0$ at 350 MeV beam energy with WASA-at-COSY*, PhD thesis, Jagiellonian University, 2011.

[64] P. Adlarson *et al.* (WASA-at-COSY), *Investigation of the $dd \rightarrow {}^3Hen\pi^0$ reaction with the FZ Jülich WASA-at-COSY facility*, Phys. Rev. C88, 014004 (2013), DOI: `10.1103/PhysRevC.88.014004`.

[65] R. Maier *et al.*, *Cooler synchrotron COSY*, Nucl. Phys. A626, 395C–403C (1997), DOI: `10.1016/S0375-9474(97)00562-9`.

[66] R. Maier, *Cooler synchrotron COSY: Performance and perspectives*, Nucl. Instrum. Meth. A390, 1–8 (1997), DOI: `10.1016/S0168-9002(97)00324-0`.

[67] H. Stein *et al.*, *Current Status of the COSY Electron Cooler (Jülich, Germany)*, Atomic Energy 94, 24–26 (2003), DOI: `10.1023/A:1023486402224`.

[68] D. Prasuhn *et al.*, *Electron and stochastic cooling at COSY*, Nucl. Instrum. Meth. A441, 167–174 (2000), DOI: `10.1016/S0168-9002(99)01128-6`.

[69] R. Gebel *et al.*, *Barrier-bucket RF tests*, IKP Ann. Rep. Jül-4282, FZ Jülich, 2008.

[70] C. F. Redmer, *In search of the Box-Anomaly with the WASA facility at COSY*, PhD thesis, Bergische Universität Wuppertal, 2010.

[71] H.-H. Adam *et al.* (WASA-at-COSY), *Proposal for the wide angle shower apparatus (WASA) at COSY-Julich: WASA at COSY*, arXiv: `nucl-ex/0411038`, 2004.

[72] C. Bargholtz *et al.* (CELSIUS/WASA), *The WASA Detector Facility at CELSIUS*, Nucl. Instrum. Meth. A594, 339–350 (2008), DOI: `10.1016/j.nima.2008.06.011`.

[73] M. Żurek, *Design of the new detector setup for the $dd \rightarrow \alpha\pi^0$ reaction measurement*, MSc thesis, Jagiellonian University, 2013.

[74] C. Ekstrom *et al.* (CELSIUS/WASA), *Hydrogen pellet targets for circulating particle beams*, Nucl. Instrum. Meth. A371, 572–574 (1996), DOI: `10.1016/0168-9002(96)00009-5`.

[75] B. Trostell, *Vacuum injection of hydrogen microsphere beams*, Nucl. Instrum. Meth. A362, 41–52 (1995), DOI: `10.1016/0168-9002(95)00302-9`.

[76] F. Winnemöeller *et al.*, *The WASA-at-COSY pellet targets*, IKP Ann. Rep. Jül-4262, FZ Jülich, 2007.

[77] F. Bergmann *et al.*, *The WASA-at-COSY pellet targets*, IKP Ann. Rep. Jül-4282, FZ Jülich, 2008.

[78] F. Winnemöeller, *Analyse des verbotenen η-Meson Zerfalls $\eta \rightarrow \pi^0 e^+e^-$ am Experimentaufbau WASA-at-COSY*, PhD thesis, Westfälische Wilhelms-Universität Münster, 2011.

[79] *WASA Collaboration, Common materials*, URL: `http://wasasrv.ikp.kfa-juelich.de/WasaWiki` (visited on 08/17/2016).

[80] F. Bergmann, Private communication, 2016.

[81] A. Pricking, *Double Pionic Fusion to ^{4}He - Kinematically Complete Measurements over the Energy Region of the ABC Effect*, PhD thesis, Universität Tübingen, 2011.

[82] C. Grupen and B. Shwartz, *Particle Detectors*, Second, Cambridge University Press, 2008, 122–127, ISBN: 9780511534966, DOI: `10.1017/CBO9780511534966`.

[83] H. Calén *et al.*, *Detector setup for a storage ring with an internal target*, Nucl. Instrum. Meth. A379, 57–75 (1996), DOI: `10.1016/0168-9002(96)00468-8`.

[84] M. Janusz *et al.*, IKP Ann. Rep. Jül-4234, FZ Jülich, 2006.

[85] M. Janusz, *Study of the η meson decay into $\pi^+\pi^-e^+e^-$ using WASA-at-COSY detector system*, PhD thesis, Jagiellonian University, 2010.

[86] P. Vlasov, *Analysis of the $\eta \to 3\pi^0$ decay in the pp interaction*, PhD thesis, Ruhr-Universität Bochum, 2008.

[87] E. Perez del Rio, *ABC Effect and d* Resonance in Double-Pionic Fusion to ^{3}He*, PhD thesis, Universität Tübingen, 2014.

[88] M. Jacewicz, *Measurement of the reaction $pp \to pp\pi^+\pi^-\pi^0$ with CELSIUS/WASA at 1.36 GeV*, PhD thesis, Uppsala Universitet, 2004.

[89] P. Podkopał, IKP Ann. Rep. Jül-4282, FZ Jülich, 2009.

[90] R. J. M. Y. Ruber, *Ultra-thin-walled Superconducting Solenoid for Meson-decay Physics*, PhD thesis, Uppsala Universitet, 1999.

[91] B. R. Jany, *Assembly and measurements of the Electromagnetic Calorimeter components for WASA-at-COSY setup*, MSc thesis, Jagiellonian University, 2006.

[92] J. Hambe, *Measurements of the Response Characteristics of CsI(Na) Crystals*, MSc thesis, RWTH Aachen University, 2010.

[93] V. Hejny *et al.*, *Performance issues of the new DAQ system for WASA at COSY*, IEEE Trans. Nucl. Sci. 55, 261–264 (2008), DOI: `10.1109/TNS.2007.914033,10.1109/RTC.2007.4382807`.

[94] H. Kleines *et al.*, *The new DAQ system for WASA at COSY*, IEEE Trans. Nucl. Sci. 53, 893–897 (2006), DOI: `10.1109/TNS.2006.873305`.

[95] C. Zheng, *Matching Trigger Efficiency of Forward Detector of WASA-at-COSY*, IKP Ann. Rep. Jül-4282, FZ Jülich, 2008.

[96] P. Marciniewski, *Fast digital Trigger Systems for Experiments in High Energy Physics*, PhD thesis, Uppsala Universitet, 2001.

[97] V. Hejny, M. Hartmann, and A. Mussgiller, *RootSorter: A New Analysis Framework for ANKE*, Jül-4052, FZ Jülich, 2002.

[98] *ROOT Data Analysis Framework*, URL: https://root.cern.ch/ (visited on 05/24/2016).

[99] R. Brun *et al.*, *GEANT Detector Description and Simulation Tool*, CERN-W5013, CERN, 1994.

[100] *HADES Experiment*, URL: https://www-hades.gsi.de/ (visited on 05/24/2016).

[101] I. Frohlich *et al.*, *Pluto: A Monte Carlo Simulation Tool for Hadronic Physics*, PoS ACAT2007, 076 (2007), arXiv: 0708.2382 (nucl-ex).

[102] *TGenPhaseSpace Class Reference*, URL: https://root.cern.ch/doc/master/classTGenPhaseSpace.html (visited on 07/12/2016).

[103] G. Bizard *et al.*, *Experimental study and baryonic exchange interpretation of the reaction $^2H(d,n)^3He$ in the intermediate energy region*, Phys. Rev. C22, 1632–1637 (1980), DOI: 10.1103/PhysRevC.22.1632.

[104] L. Bianchi, Private communication, 2016.

[105] V. Hejny, *Calorimeter calibration*, URL: http://wasasrv.ikp.kfa-juelich.de/WasaWiki/index.php/Software:Calorimeter_calibration (visited on 08/26/2016).

[106] *TMinuit Class Reference*, URL: https://root.cern.ch/doc/master/classTMinuit.html (visited on 06/02/2016).

[107] M. Schever, Project work, Private communication, 2014.

[108] M. Nanova *et al.* (CBELSA/TAPS), *In-medium omega mass from the $\gamma + Nb \to \pi^0\gamma + X$ reaction*, Phys. Rev. C82, 035209 (2010), DOI: 10.1103/PhysRevC.82.035209.

[109] R. Barlow, *Systematic errors: Facts and fictions*, in: *Conference on Advanced Statistical Techniques in Particle Physics, Proceedings*, 2002, 134–144, arXiv: hep-ex/0207026 (hep-ex).

[110] A. Wronska *et al.*, *Near threshold eta meson production in the $dd \to {}^4He\eta$ reaction*, Eur. Phys. J. A26, 421–428 (2005), DOI: 10.1140/epja/i2005-10185-0.

Erklärung

Ich versichere, dass ich die von mir vorgelegte Dissertation selbständig angefertigt, die benutzten Quellen und Hilfsmittel vollständig angegeben und die Stellen der Arbeit — einschließlich Tabellen, Karten und Abbildungen —, die anderen Werken im Wortlaut oder dem Sinn nach entnommen sind, in jedem Einzelfall als Entlehnung kenntlich gemacht habe; dass diese Dissertation noch keiner anderen Fakultät oder Universität zur Prüfung vorgelegen hat; dass sie — abgesehen von unten angegebenen Teilpublikationen — noch nicht veröffentlicht worden ist sowie, dass ich eine solche Veröffentlichung vor Abschluss des Promotionsverfahrens nicht vornehmen werde. Die Bestimmungen der Promotionsordnung sind mir bekannt. Die von mir vorgelegte Dissertation ist von Prof. Dr. Hans Ströher betreut worden.

Teilpublikationen

- M. Żurek, *Charge Symmetry Breaking in the dd $\rightarrow$ $^4He\pi^0$ reaction with the WASA-at-COSY experiment*, IKP Ann. Rep. Jül-4393, (2016).

- M. Żurek, *Charge Symmetry Breaking in the dd $\rightarrow$ $^4He\pi^0$ reaction with the WASA-at-COSY experiment*, IKP Ann. Rep. Jül-4381, (2015).

- M. Żurek, *Investigations of the charge symmetry breaking reaction dd $\rightarrow$ $\alpha\pi^0$ with the WASA-at-COSY experiment, MesonNet 2014 International Workshop Proceedings*, arXiv:1412.5451 [nucl-ex], (2014).

- M. Żurek, *Investigations of the charge symmetry breaking reaction dd $\rightarrow$ $\alpha\pi^0$ with the WASA-at-COSY experiment*, EPJ Web of Conferences **66**, 05024 (2014).

Lebenslauf

Persönliche Angaben

Name:	Maria Katarzyna Żurek
Gebursdatum:	28.02.1990
Geburtort:	Chrzanów, Polen
Staatsangehörigkeit:	Polnish
Familienstand:	Ledig

Akademische Ausbildung

seit Oktober 2013	Promotionsstudium Universität zu Köln, Köln, Deutschland
Oktober 2011 - Juni 2013	Master der Experimentalphysik Jagiellonen-Universität, Krakau, Polen Gesamtnote: mit Auszeichnung
Oktober 2008 - Juni 2011	Bachelor der Experimentalphysik Jagiellonen-Universität, Krakau, Polen Gesamtnote: mit Auszeichnung

Schulbildung

2005 - 2008	Oberstufenschule, I Liceum Ogólnokształcące, Chrzanów, Polen
2002 - 2005	Mittelstufenschule, Gimnazjum Nr. 1, Trzebinia, Polen
1996 - 2002	Grundschule, Płoki, Polen